STUDY OF DISPLACEMENT CASCADES IN Y-Ti-O SYSTEMS USING CLASSICAL MOLECULAR DYNAMICS

By

Manan Dholakia

(Enrolment No. **PHYS 02 2010 04 014**)

Indira Gandhi Centre for Atomic Research, Kalpakkam, India.

A thesis submitted to the

Board of Studies in Physical Sciences

In partial fulfillment of requirements

For the Degree of

DOCTOR OF PHILOSOPHY

of

HOMI BHABHA NATIONAL INSTITUTE

November, 2017

Homi Bhabha National Institute

Recommendations of the Viva Voce Board

As members of the Viva Voce Committee, we certify that we have read the dissertation prepared by Shri. **Manan Dholakia** entitled **Study of displacement cascades in Y-Ti-O systems using classical molecular dynamics** and recommend that it may be accepted as fulfilling the thesis requirement for the award of Degree of Doctor of Philosophy.

for N.V. Chandra Shekar (Dean-(A)) _____ Date: 16/8/18

(Chairman)

_____ (S. Mathi Jaya) Date: 16/8/18

(Guide/Convener)

G. Vaitheeswaran _____ Date: 16/8/18

(External Examiner) (G.S. VAITHEESWARAN)

_____ Date: 14/8/18

(Member 1)

_____ (SHARAT CHANDRA) _____ Date: 16/8/18

(Member 2)

Final approval and acceptance of this thesis is contingent upon the candidate's submission of the final copies of the thesis to HBNI.

I hereby certify that, I have read this thesis prepared under my direction and recommend that it may be accepted as fulfilling the thesis requirement

Date: 16/8/18

Place: Kalpakkam

(Guide)

Acknowledgements

I gratefully acknowledge my guide Dr. S. Mathi Jaya, for his constant support, motivation, and concern. His guidance helped me in all the time of research. I thank him for carefully going through the thesis.

I thank Dr. Sharat Chandra for always being there for any kind of help, for teaching me so many things, for helping me in helping others, and for unintentionally honing my debating skills by constantly disagreeing even when I am agreeing with him.

Any problem, whether it is about the installation of Linux in a PC or solving some hard-core mathematical problem, should be taken up as a challenge. This was taught to us by our teacher and the former Division Head, Shri. M. C. Valsakumar and I thank him for always setting his own example and going to extremes to teach us the importance of passion, perseverance, and dedication towards work.

I sincerely thank my thesis committee members Dr. C. S. Sundar and Dr. B. K. Panigrahi, for their help, insightful comments and technical inputs. I also thank Prof. N. V. Chandrashekhar, Dean, Physical Sciences, HBNI, for his help and encouragement and for making all the official procedures related to the Ph.D work very smooth and streamlined. I sincerely thank former Director IGCAR, Dr. Baldev Raj and present Director IGCAR, Dr. A. K. Bhaduri for their support and encouragement.

I would like to thank Dr. G. Raghavan for giving me sincere bits of advice, for his constant support and for his helping nature. My sincere thanks go to Shri. V. Sridhar for always giving me food for thought on all the topics and for providing me opportunities to flourish. I thank Dr. S. Sivakumar for useful scientific discussions and for providing me opportunities to take classes along with him on General Relativity and Quantum mechanics, which boosted my confidence and knowledge, and made me realize the importance of learning other subjects too. I sincerely thank Dr. S. Kalavathi for being a well-wisher and for always motivating me. I heartfully thank Dr. Nithya Ravindran for her constant encouragement and
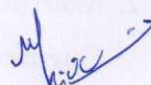
I dedicate this thesis to the Nature – for its inspiration, magnificence, and beauty.

2. *Displacement cascades in Fe-Y_2TiO_5 system : A Molecular Dynamics Investigation.* **Manan Dholakia**, Sharat Chandra and S. Mathi Jaya, Modelling and Simulation of Safety and Materials for Nuclear Application -2015, December 16-17, 2015, Anupuram, Kalpakkam, India.

3. *Development of empirical interatomic potentials for Y_2TiO_5 and $Y_2Ti_2O_7$ and study of displacement cascades using Molecular Dynamics.* **Manan Dholakia**, Sharat Chandra and S. Mathi Jaya, Conference on Computer Simulation of Radiation Effects in Solids -2016, Loughborough University, UK, June-2016.

(d) Publications not included in the thesis

1. *Simulating radiation damage in a bcc Fe system with embedded yttria nanoparticle.* T Lazauskas, S. D. Kenny, R. Smith, Gurpreet Kaur, **Manan Dholakia**, M. C. Valsakumar, Journal of Nuclear Materials, **437**, 317-325 (2013).

2. *Nonlinear effects in defect production by atomic and molecular ion implantation.* C. David, C. Varghese Anto, **Manan Dholakia**, Sharat Chandra, K. G. M. Nair, B. K. Panigrahi, P. Santhana Raman, S. Amirthapandian, G. Amarendra, and John Kennedy, Journal of Applied Physics **117**, 014312 (2015).

Manan Dholakia

List of Publications

(a) Journals

1. *Atomistic simulations of displacement cascades in Y_2O_3 single crystal.* **Manan Dholakia**, Sharat Chandra, M. C. Valsakumar, S. Mathi Jaya, Journal of Nuclear Materials, **454**, 96-104 (2014).

2. *Properties of Y_2TiO_5 and $Y_2Ti_2O_7$ crystals: Development of novel interatomic potentials.* **Manan Dholakia**, Sharat Chandra, S. Mathi Jaya, Journal of Alloys and Compounds, **739**, 1037- 1047 (2018).

3. *A comparative study of topology and local disorder in Y_2O_3, Y_2TiO_5 and $Y_2Ti_2O_7$ crystals.* **Manan Dholakia**, Sharat Chandra, S. Mathi Jaya, Materialia (Under review).

(b) Conference proceedings

1. *Role of $\sum 5$ (210)[001] CSL Boundaries on Displacement CSL Boundaries on Displacement Cascades in bcc-Fe.* Prithwish K. Nandi, **Manan Dholakia** and M. C. Valsakumar, AIP Conf. Proc. **1447**, 743 (2012).

2. *Molecular Dynamics Studies of Radiation Damage in Yttria.* **Manan Dholakia**, Gurpreet Kaur and M. C. Valsakumar, AIP Conf. Proc. **1512**, 1288 (2013).

3. *Displacement cascades in twist and tilt grain boundaries in Fe-bicrystal: Molecular dynamics studies.* **Manan Dholakia**, Prithwish K. Nandi, and M. C. Valsakumar, AIP Conf. Proc. **1665**, 080049 (2015).

4. *Molecular dynamics studies of displacement cascades in Fe-Y_2TiO_5 system.* **Manan Dholakia**, Sharat Chandra and S. Mathi Jaya, AIP Conf. Proc. **1731**, 140046 (2016).
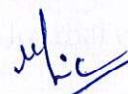
(c) Papers presented in national/international conferences

1. *Displacement Cascades in Y_2O_3: A Molecular Dynamics Investigation.* **Manan Dholakia**, Sharat Chandra and S. Mathi Jaya, Swift Heavy Ions in Materials Engineering and Characterization -2014, Delhi, October-2014.

DECLARATION

I, hereby declare that the investigation presented in the thesis has been carried out by me. The work is original and has not been submitted earlier as a whole or in part for a degree / diploma at this or any other Institution / University

Manan Dholakia

STATEMENT BY AUTHOR

This dissertation has been submitted in partial fulfillment of requirements for an advanced degree at Homi Bhabha National Institute (HBNI) and is deposited in the Library to be made available to borrowers under rules of the HBNI.

Brief quotations from this dissertation are allowable without special permission, provided that accurate acknowledgment of source is made. Requests for permission for extended quotation from or reproduction of this manuscript in whole or in part may be granted by the Competent Authority of HBNI when in his or her judgment the proposed use of the material is in the interests of scholarship. In all other instances, however, permission must be obtained from the author.

Date: 16/8/18
Place: Kalpakkam

Manan Dholakia

their radiation damage properties and the ways we can get insights in these systems using topological methods.

dividual cation polyhedra and calculating the change in energy of the systems by performing molecular statics runs using LAMMPS [13]. The idea is, higher the energy change, more will be the resistance to amorphization. To obtain statistically robust results, 1000 different random configurations for a given distortion are generated and then molecular statics runs are performed on all the configurations.

In both of these studies, the cation polyhedra are assumed to remain intact. But, in processes like displacement cascades, the polyhedra might completely get destroyed and a detailed insight into the dynamics of the processes becomes necessary. Thus, displacement cascade studies using MD simulations are carried out for Y-Ti-O systems for different PKA energies and initial temperatures of the lattice. To obtain good insight from different approaches, we employ point defect analysis using equivalent sphere method [30] as well as ring analysis [14] to analyze the damage in the systems. Ring statistics, as mentioned earlier, is a manifestation of graph theory and uses the concept of primary rings [15].

It is seen that the defect production in displacement cascades happens predominantly due to ballistic collisions. Melted and a radiation damaged system can show a clearly different topology, and this characteristic can be effectively discerned by ring analysis. The structural freedom analysis and testing it using interatomic potentials shows Y-Ti-O systems are highly constrained and have a comparable amorphization resistance which is much higher than known amorphziable materials like SiO_2 [31]. Study of dynamics of displacement cascades showed that at the end of simulation time, highest number of defects survive in Y_2TiO_5. A substantial number of cation antisite formation indicates the proclivity of pyrochlores towards order-disorder transition to defect fluorite structure.

CHAPTER-6: Conclusions and future outlook: This chapter provides an overview of the results described in this thesis and the insights gained into the behaviour of the Y-Ti-O systems undergoing displacement cascades. We also discuss the future outlook for simulating the systems for longer time scales using accelerated molecular dynamics. The chapter also discusses the outlook for the work which would be carried out on a comparative study of pyrochlores and fluorites with respect to

employing linear least square fitting, available in the GULP [24] package to obtain the parameters of the potential. The potential thus developed, is then validated by calculating various physical properties such as defect formation energies, melting point, thermal expansion coefficient and elastic constants using MD procedures. The potentials reproduce melting points (MP) of both the systems fairly accurately with predicted MP of Y_2TiO_5 and $Y_2Ti_2O_7$ as 1935 K (Exp. $\sim$ 2000 K [25]) and 2385 K (Exp. $>$ 2173 K [26]) respectively. The cation antisite pair formation energy is found to be quite less in both the systems, which indicates towards the tendency of pyrochlores to form cation antisite defects leading to order-disorder transition [27].

CHAPTER-5: A comparative study of displacement cascades in Y-Ti-O systems using structural and connectivity topology analyses: This chapter makes a comparative study of displacement cascades for different PKA energies (up to 8 keV) and different initial temperatures (300 K, 600 K, 900 K) of the lattice for Y-Ti-O crystals using MD simulations. We also study the amorphization characteristics of these systems using connectivity topology analyses such as structural freedom analysis [28] and ring analysis [14].

According to Zachariasen [29], materials that get a substantial energy change when disordered, must be averse for the disordered state and hence, must be resistant to amorphization. To test this hypothesis with reference to the Y-Ti-O systems, we start with the constraints analysis, which analytically quantifies Zachariasen's criteria by calculating the degree of freedom of the cation polyhedra forming the matrix and predicts amorphizability of systems based on their structures [28].

Since the constraints analysis doesn't explicitly take into account the role played by interatomic interactions, it may in some cases, predict similar amorphizability for the systems having similar crystal structure but very different interatomic interactions [11]. Thus to improve upon the insight obtained from this analysis, we go on to actually test Zachariasen's criteria using interatomic potentials for these materials (for Y_2O_3, Belonoshko's potential [17] and in-house generated potentials for Y_2TiO_5 and $Y_2Ti_2O_7$). This is done by applying various distortions to the in-

keV) are also performed. Interatomic potential developed by Belonoshko *et. al* [17], containing a Born-Mayer term [18] combined with Coulomb potential, is used for the cascade simulations. An extensive set of data is generated corresponding to 253 different crystallographic directions for the initiation of PKA, as well as for different PKA species (Y or O atom). The production and annihilation of point defects, the influence of the mass of PKA on structural changes and the influence of the direction of PKA on the cascades is studied.

It is seen that for 0.5 keV PKA energy, Y PKA produces $\sim$ 18% higher number of defects as compared to O PKA. While the peak number of Frenkel pairs generated by any PKA does not significantly depend on the PKA direction, the number of surviving Frenkel pair defects does show a distribution, but a definite correlation between the PKA direction and surviving number of defects is not discernible. Y-O bond is observed to be quite resilient and the short-range order in Y_2O_3 never disappears even at the peak of cascades. This points towards the high stability of Y_2O_3 precipitates under radiation damage processes.

CHAPTER-4: Development of interatomic potentials for Y_2TiO_5 and $Y_2Ti_2O_7$ crystals: This chapter discusses the theory, methodology, and validation for the development of new interatomic potentials for Y_2TiO_5 and $Y_2Ti_2O_7$ crystals. As these systems are predominantly ionic in nature [19], pair-wise interatomic potentials can represent them fairly well [12]. Buckingham potential is a popular choice for modeling pair interactions and its combination with Coulomb potential is used to describe interactions in these systems. Parameters of the potential (A_{ij}, ρ_{ij}, C_{ij}, q_i, q_j) need to be fixed using experimental as well as other theoretical results on physical properties of the systems. Since all the required data for fitting is not available, we use the VASP package [20–23] to generate data corresponding to different properties of the systems taking into account different cell volumes, structures, configurations, and distortions. Data obtained using the equation of state (EOS) runs consisting of angular distortions of the cell as well as various defect configurations with the full relaxation of the lattice are also generated to be used in the fitting. All the data generated for fitting the potential is then used in the fitting module

stands the way radiation damage affects the materials, we discuss the various ways radiation damage and the resulting amorphization in materials is predicted. The limitations and applicability of these criteria in different scenarios is also discussed, and we highlight the ways computer simulations can provide useful insights into the disordering mechanisms. The chapter then gives a motivation for taking Y-Ti-O systems as the system of study for this thesis and gives an overview of the thesis.

CHAPTER-2: Theoretical and computational methods: This chapter discusses the theoretical and computational methods used in this thesis. Since classical molecular dynamics (MD) has been the extensively used technique in this work, we make an elaborate discussion elucidating the basic philosophy of MD, as well as its working methodology, with a special emphasis on simulating displacement cascades in materials. Post-processing of MD data is a crucial step, thus we discuss in detail the methods used for analysing the data obtained from MD simulations, particularly in the context of displacement cascades. The development of interatomic potentials for Y-Ti-O crystals, which is the subject matter of Chapter-4, required generating first principle data using density functional theory (DFT) for the systems for various configurations. Thus we also discuss the basics of DFT.

This chapter also discusses the theory and methodology of ring analysis [14], which has been used in the analysis of cascades described in Chapter-5 of this thesis. The basic principles of ring analysis are based on the topological ideas to describe the arrangements of atoms in terms of their connectivities (bonds) [15]. These concepts are quite powerful when applied to highly defective solids, as the concept of reference lattices and symmetry relations may become less useful in these systems [16]. This description sets a stage for the connectivity topology analysis carried out in Chapter-5 of this thesis.

CHAPTER-3: Displacement cascade studies in yttria crystal: This chapter describes cascades in yttria (Y_2O_3) crystal, for an initial equilibration temperature of 300 K and for different initial directions of the primary knock-on atom (PKA). The chapter mainly focusses on low-energy cascades (0.5 keV) and a large statistics is generated for this energy, while some higher energy simulations (up to 3 and 5

However, various studies have shown that irradiation causes changes to nanoparticle size, their number density, chemistry and crystal structure, and these changes have adverse consequences for the mechanical strength and irradiation resistance of steels, especially at high irradiation levels [6]. The complex chemistry, amorphization due to radiation damage [6] and crystallite size of these oxides are important factors that affect their radiation behavior [10]. Thus, understanding the irradiation evolution of Y-Ti-O systems and a thorough knowledge of displacement cascades in them is important for our ability to predict long-term material degradation.

Classical molecular dynamics stands as a very effective tool to understand displacement cascades owing to its ability to provide a dynamical as well as statistical picture simultaneously [5]. Using MD, one can actually visualize the process of displacement cascades as it provides coordinates and velocities of all atoms in the structure, giving the full phase trajectory of damage propagation. At the end of the simulation, the resulting structure contains structural changes due to radiation damage, which can be analysed in detail. MD simulations have also been used to study resistance to amorphization in several materials [11]. However, MD simulations have their own limitations, and the reliability of the data obtained depends heavily on the reliability of the interatomic potentials used for the simulations [12]. The robustness of the interatomic potentials is, therefore, one of the central requirements of MD studies.

In this thesis, we study displacement cascades in Y_2O_3, Y_2TiO_5 and $Y_2Ti_2O_7$ crystals, which are important materials for ODS steels. We use classical molecular dynamics as implemented in LAMMPS package [13]. Since the appropriate interatomic potentials for Y_2TiO_5 and $Y_2Ti_2O_7$ crystals were not available in the literature, we also develop interatomic potentials for these systems. The thesis comprises of six chapters and a brief description of the content of each chapter is as follows:

CHAPTER-1: Introduction: This chapter provides an overview of the problem of radiation damage in materials. Since better materials can be designed if one under-

SYNOPSIS

Core structural materials of nuclear reactors face intense irradiation, high temperature and large thermal gradients that deteriorate their mechanical, elastic and thermal properties, thereby severely reducing the operational life [1]. Resistance to radiation damage (RD) is one of the most important properties a material must possess for it to be used as structural material for nuclear reactors [2]. Radiation resistant materials are required for waste forms, for fuel, and also for other applications in the nuclear fuel cycle [3]. Making better radiation resistant materials has been a holy grail for the nuclear industry and this goal requires a sound understanding of the basic mechanism of RD in the materials [4]. Long-term radiation effects depend crucially on the initial process of radiation damage event [5], i.e, displacement cascades and a thorough understanding of RD can be achieved if we understand the processes involved in displacement cascades properly. Experiments provide important insights, but the atomic length and time scales of displacement cascades make it difficult to probe them with experiments alone. In this regime, classical molecular dynamics (MD) simulations have been proved to be quite useful in getting some important insights [5].

The advent of oxide dispersion strengthened (ODS) steels is one of the most crucial advancements in the field of radiation resistant materials. They exhibit excellent high-temperature strength and creep resistance [2] and have emerged as the prime candidate materials for fusion and advanced fission reactor concepts [6]. ODS steels are made by alloying Fe-Cr-Ti powder with yttrium oxide (Y_2O_3) precipitates, followed by hot consolidation [7]. The fine dispersion of Y_2O_3, Y_2TiO_5 and $Y_2Ti_2O_7$ precipitates formed by this process enhance the mechanical strength of steels [8] by pinning the dislocations and are quite stable at high temperatures as well as at high neutron irradiation dose [9]. They are believed to provide resistance to irradiation damage, specifically void swelling and bubble growth [2] by playing an important role in trapping helium, produced in the nuclear reactors and hence reduce degradation of strength and thermal creep [7].

Contents

List of Tables

List of Figures

that are appropriate for modeling large-scale MD simulations, as well as for modeling energetic processes.

The thesis comprises of six chapters. An overview of all the chapters is as follows:

- **Chapter**-2: (*Theoretical and computational methods*): In this chapter, we discuss the basic concepts of MD, density functional theory (DFT), and ring analysis. We also discuss the basic types of rings present in the Y-Ti-O systems and show their relationships with the corresponding connectivities of the cation polyhedra in their respective lattices.

- **Chapter**-3: (*Displacement cascades studies in yttria crystal*): In this chapter, we discuss the studies of displacement cascades in Y_2O_3 single crystal. The effect of different PKA species and different initial PKA directions on the cascade characteristics is studied in detail.

- **Chapter**-4: (*Development of interatomic potentials for Y_2TiO_5 and $Y_2Ti_2O_7$ crystals*): In this chapter, we discuss the theory and methodology for the development of interatomic potentials for Y_2TiO_5 and $Y_2Ti_2O_7$ systems. The validation of potentials by comparing the calculated values with the experimental/ first principle calculation values is done and the details are discussed.

- **Chapter**-5: (*A comparative study of displacement cascades in Y-Ti-O systems using structural and connectivity topology analyses*): In this chapter, we make a comparative study of displacement cascades in Y-Ti-O systems. We use different tools to probe the systems and use molecular dynamics to investigate the dynamics of displacement cascades. Different irradiation conditions are taken for generating the displacement cascades and the disorder in the cascade-region is probed using various tools.

- **Chapter**-6: (*Conclusions and future outlook*): In this chapter, we outline the highlights of all the main results obtained in this thesis and discuss the ways the present work can be extended.

around Ti defects occur due to a decrease of the Ti coordination number.

With this view, it is understood, that to make a clear picture of displacement cascade characteristics in Y-Ti-O systems, MD stands as an important tool. As we discussed, interatomic potentials make the most crucial requirement of any MD study and a correct modeling of them enables one to elicit out the basic mechanism of displacement cascades. Thus, it is important to use interatomic potentials that can model the displacement cascade processes effectively in these materials.

1.2 An overview of the thesis

This thesis deals with the study of displacement cascades in Y_2O_3, Y_2TiO_5 and $Y_2Ti_2O_7$ crystals. These are important ingredients of the ODS steels and it is important to study their irradiation behavior under similar conditions. Although there are many studies that have explored their characteristics, there still remains a gap in a complete understanding of their behavior under displacement cascades. This understanding is crucial for predicting their long-term irradiation evolution. Thus, we carry out MD simulations of displacement cascades in these materials and analyze the systems using different tools to explore the damage characteristics in them in detail. Further, in any MD study, the role played by interatomic potentials is crucial, and they become indispensable when one wants to study the radiation stability of materials. With all these issues in our view, we address the following main objectives in this thesis:

- A detailed study of displacement cascades in Y_2O_3, Y_2TiO_5 and $Y_2Ti_2O_7$ crystals. The systems should be compared under similar irradiation conditions (such as the initial temperature of the lattice, PKA energies, etc.). Further, the irradiation conditions must also be varied to study their radiation characteristics in detail.

- A deeper understanding of the in-cascade properties and a detailed analysis of disorder in materials.

- The development of interatomic potentials for Y_2TiO_5 and $Y_2Ti_2O_7$ crystals
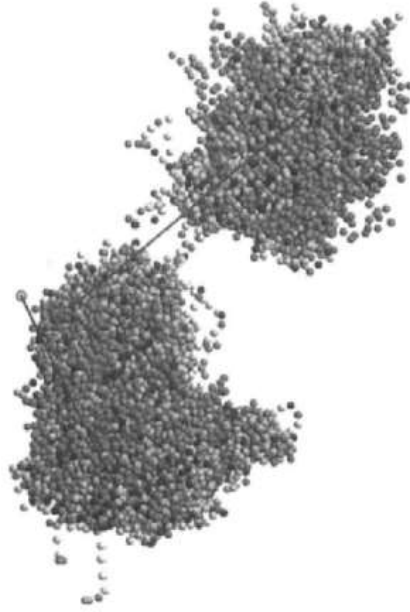
Figure 1.3 – MD studies on displacement cascades shows the development of a sub-cascade in a 20 keV cascade in Ni_3Al. Figure taken from Ref. [32].

scales, thereby reducing the damage in the host matrix. It was shown that when the cascade is initiated near the nanoparticle, the oxide/matrix interface arrests the cascade propagation and the cascade energy instead induces partial amorphization of the Y_2O_3 nanoparticle [70]. MD studies of displacement cascades in Y-Ti-O oxides are sparse, particularly in the case of Y_2TiO_5. Some of the simulation studies of displacement cascades in bixbyite, which is the structure of Y_2O_3, include the work of Kittiratanawasin *et. al* [50, 71]. They performed MD simulations of displacement cascades in Er_2O_3, for different PKA energies, and for different PKA species and found that the cascade formed by heavier Er atom is different from that produced by O atom. In pyrochlores, there have been many simulation studies that have provided useful insights [49, 52, 72–75]. Xiao *et. al* [76] carried out ab initio MD simulations to determine threshold displacement energies and defect formation energies in $Y_2Ti_2O_7$. It was shown that the formation energies of vacancies and Frenkel pairs are relatively higher than those for interstitials and antisite defects. Recently Sattony *et. al* [77] carried out experimental as well as molecular dynamics studies to understand the role played by short-range order on the response of $Y_2Ti_2O_7$ to irradiation. They found that a lot of strong local distortions

MD with its unique capability to simultaneously provide the dynamical as well as the statistical information of the systems, has been the most appropriate computational technique to study energetic cascades. A proper and educated use of statistical ensembles, an adequate simulation cell-size and appropriate boundary conditions can mimic the process of displacement cascades quite realistically. MD has been the most popular technique to study displacement cascades for many decades, and in fact even in very early simulations, it could provide some crucial insights into the detailed processes in displacement cascades. For instance, in the sixties, the MD simulations carried out by Erginsoy *et. al* [59] showed the anisotropy in displacement threshold energy. Gibson *et. al* [60] showed the importance of replacement collision sequences. In 1987, Diaz de la Rubia *et. al* [61] carried out MD simulations which showed the basics of the primary stages of damage evolution, and proved that Brinkman's picture, as shown in Fig. 1.2, is indeed correct. The MD simulations carried out by Webb and Harrison [62] showed the importance of the primary stage of damage evolution by showing that heat spike effects can influence the atomic mixing substantially. It was also shown that pits and adatoms can be formed in cascades at surfaces [63]. Many studies on MD showed that as the energy is dissipated from the cascade-region, substantial atomic mixing takes place and by analysing the radial distribution function (RDF), it was shown that the cascade-region behaves like a melt [61, 64, 65]. Melting has a profound influence on the number of atoms that are displaced in the cascade and on the primary state of damage [32]. Ghaley *et. al* [66–68] showed how the liquid formed in the thermal spike can flow on the surface thereby producing dramatic consequences on surface morphology. The work by Diaz de la Rubia *et. al* [65, 69] showed that in the case of Si, a phase transformation to a stable amorphous state directly occurs in the collision cascade regime. An important aspect of highly energetic cascades is sub-cascade branching, as shown in Fig. 1.3, was also shown by MD studies.

A recent study of displacement cascades in Y_2O_3 embedded in Fe matrix showed that the nanoparticle absorbs the energy of the PKA and releases it at longer time

als, one needs to consider various parameters. In the next section, we discuss the way computational techniques, such as MD can provide some useful insights into the various processes in the displacement cascades and hence provide a clue about the relative radiation stability of materials.

1.1.4   Investigating irradiation behaviour using MD

The criteria considered in the previous discussion do not explicitly consider the role of interatomic interactions. It seems that to really understand the mechanism of amorphization, one should investigate the role played by the interatomic forces, i.e, the type of bonding in materials [56]. It is suggested, that the root cause of the resistance to amorphization is governed by a competition between the short-range and the long-range interatomic forces [57]. In this regard, MD simulations with realistic interatomic potentials can naturally play an important role. The long-range contribution arises as the potentials often have electrostatic charges which emulate ionicity. Further, even for the materials having very high ionicity, the potentials also have short range 'bonding' interactions in order to stabilize the structure [11]. These characteristics of the interatomic potentials become indispensable in the thermal spike regime of displacement cascades and are responsible for the fate of the disordered cascade-region. A considerable fraction of defects initially produced in displacement cascades gets recombined and generally, the number of defects that eventually survive are lesser than that predicted by Norgett-Robinson-Torrens (NRT) formula [58], which is based on the binary collision approximation. This is because, in the initial stages of displacement cascades, atoms move at very high energies and the interatomic interactions are mainly governed by the strong short-range repulsive forces only. At this stage, binary collision approximation is valid. However, in the later stage when the energies of the atoms get lowered down, the nature of the interatomic forces at equilibrium comes into play and influences in a major way the final arrangement atoms adopt after the cascade subsides and thus, crucially dictate the amorphization characteristics of materials. This emphasizes upon the use of appropriate and realistic interatomic potentials to predict the behaviour of systems undergoing radiation damage.

to amorphization. The explanation for this correlation was attributed to the high rise in the electrostatic energy in ionic materials upon substitutional disorder.

Many criteria suggest that the ratio of cation radius in complex oxides plays a major role in the amorphization resistance of materials. The materials that have a similar cation radius find it easier to get a cation disorder at a low energy cost and hence, are resistant to amorphization. For example, $Er_2Zr_2O_7$ is dramatically more resistant to amorphization than $Er_2Ti_2O_7$ as the ratio of cation radii in the former is smaller than in the latter, which reduces the energy cost for the cation disordering. The ease with which cation defects can be accommodated is correlated to amorphization resistance during irradiation [11, 48, 49]. Kittiratanawasin *et. al* [50] examined the radiation damage that can occur in MgO and magnesium aluminate spinel, $MgAl_2O_4$. In the latter case, the material was found to have the ability to incorporate large numbers of cation antisite defects, which was cited as one of the reasons for its relative tolerance to radiation. Structures which are closer to the fluorite structure are also predicted to be more resistant to amorpization and this criterion was used to explain the high amorphization resistance of binary and ternary oxides [51, 52].

A popular criterion based on the structure of materials is the 'topological' model which relates the radiation resistance to the topological freedom of a crystalline material [31, 53, 54]. According to this criterion, materials that are highly constrained, will be difficult to disorder, and hence will be resistant to amorphization. The nearest bonds are taken as defining the constraints on an atom, and structural freedom of the matrix is calculated by calculating the degree of freedom of the structuring polytopes. However, although topological freedom is a quite successful and used criterion to predict amorphization resistance, in some cases, it fails. For example, the pyrochlores $Gd_2Zr_2O_7$ and $Gd_2Ti_2O_7$ are predicted to be equally resistant to amorphization, but in reality, $Gd_2Zr_2O_7$ has a far superior amorphization resistance as compared to $Gd_2Ti_2O_7$. Similarly, SiC was predicted to be constrained and hence amorphization resistant [31], but it gets easily amorphized upon irradiation [55]. It is understood, that for predicting amorphization characteristics of materi-

1.1.3 Understanding irradiation behaviour and amorphization

Radiation damage and the resulting amorphization pose challenges on many other different avenues too. An important example is the field of nuclear waste storage materials. Waste forms are required to safely encapsulate highly radioactive materials up to a time scale of 1 million years [3]. Amorphization of the waste form matrix will lead to percolation type of defects which will enable chemical transport and thus, leakage of highly radioactive atoms into the environment. We need materials that can resist the amorphization due to irradiation, and if we can predict the amorphization characteristics of materials, it will help us in designing better radiation resistant materials.

However, the prediction of amorphization resistance of materials is a nontrivial problem, drawing interest and curiosity from both the technological and the scientific world. There are strikingly different results from experiments on amorphization due to radiation damage. Some materials are seen to be readily amorphizable, while others maintain their crystallinity even at extremely high radiation doses and cryogenic temperatures. These issues have made predicting amorphization resistance of materials an actively debated subject, with varying points of view and criteria. Many of the existing criteria in literature, are very successful in predicting amorphizabilities in some classes of materials but are found to fail in others. Kostya *et. al* [11], in an elaborate discussion on these different criteria, discuss about 20 different factors which can be relevant in the context of radiation damage induced amorphization in materials. Some of these criteria are such as the criteria based on the structure type [45], homologous crystallization temperature [46], melting point [47], temperature ratio criteria [46], structural degree of freedom criteria [28] etc. Temperature ratio criteria, proposed by Naguib and Kelly [46], makes a use of the analogy between radiation damage and crystallization of liquid. According to this criteria, the resistance of a material against amorphization increases with the increase of melting temperature and decrease of the crystallization temperature. Their second criterion was based upon the ionicity of the materials and it was suggested, that higher the ionicity of a material, higher will be its resistance

Several experimental techniques such as Atom Probe Tomography (APT) [40], Small Angle Neutron Scattering (SANS), Transmission Electron microscopy (TEM), Positron Annihilation Spectroscopy (PAS) [41] etc., have been used to understand the behavior of Y-Ti-O nanoclusters. In particular, SANS and TEM are mostly used to probe the size distribution and volume fraction and APT measurements are done to understand the composition and structure of the Y-Ti-O nanoclusters in the host matrix. The chemistry of these oxide nanoparticles has been studied by TEM using the electron energy loss spectroscopy (EELS) or energy filtered TEM (EFTEM) techniques. However, although there have been numerous experimental studies to study the behavior of nanoparticles under irradiation, the consensus on their general behavior under irradiation has been widely variable and inconclusive [6]. The reason is, one can not make a direct comparison between the results of these studies, as they have been carried out for different ODS alloys that have been fabricated, processed or heat treated differently. Further, different irradiation conditions such as particle type and energy, dose, dose rate, and temperature were used, and the initial nanoparticle compositions and morphologies differed in all the experiments [6].

It is generally known, that irradiation causes changes to the particle size, number density, chemistry and crystal structure, and these changes have adverse consequences for the mechanical strength and irradiation resistance of steels especially at high irradiation levels [6]. Further, the high-temperature conditions of irradiation environment also play a severely detrimental role. Skuratov *et. al* [42] observed that at high irradiation temperatures, the regions at the oxide-matrix interface start dissolving into the matrix, leading to an erosion and reduction in the size of the nanoparticle. Amorphization of the nanoparticles due to radiation damage has also been reported by Aleev *et. al* [43] who observed that upon irradiation, the oxide-matrix interface gets diffused, with amorphization starting from the interfaces leading to dissolution of the large nanoparticles. Under these severe conditions, the interface between the oxide particle and the host matrix becomes irregular [44] and less coherent [39].

7

ritic/martensitic steels rapidly decreases with increasing temperature. However, the drawbacks of ferritic steels can be overcome, and here comes the concept of the oxide dispersion strengthened (ODS) steels.

The advent of ODS steels is one of the most crucial advancements in the field of radiation resistant materials. The basic philosophy behind the concept of ODS steels is to enhance the mechanical properties of ferritic steels by adding precipitates in the matrix. They exhibit excellent high-temperature strength and creep resistance [2] and have emerged as the prime candidate materials for fusion and advanced fission reactor concepts [4, 36]. ODS steels are made by alloying Fe-Cr-Ti powder with yttrium oxide (Y_2O_3) precipitates, followed by a hot consolidation [7]. The fine dispersion of Y_2O_3, Y_2TiO_5 and $Y_2Ti_2O_7$ precipitates formed by this process enhance the mechanical strength of steels [8] by pinning the dislocations and are quite stable at high temperatures as well as at high neutron irradiation dose [9]. They are believed to provide resistance to irradiation damage, specifically void swelling and bubble growth [2] by playing an important role in trapping helium and hence reduce degradation of strength and thermal creep [7]. Understanding the irradiation evolution of Y-Ti-O systems and a thorough knowledge of displacement cascades in them is important for our ability to predict long-term material degradation.

1.1.2 Irradiation behaviour of Y-Ti-O nanoclusters

It is known, that the chemistry, size, and the number density of the Y-Ti-O nanoclusters, as well as their coherence with the host matrix, are some of the key parameters which decide their radiation behavior [6, 10]. The typical size of the Y-Ti-O nanoclusters should be $\sim$ 2-5 nm, for them to be effective in pinning the dislocations. Also, coherence with the host matrix is a very important factor, as it decides the role of the nanoparticles to act as effective sinks for the defects generated in a radiation damage event [37, 38]. Studies using high-resolution transmission microscopy (HRTEM) have shown that the Y-Ti-O nanoparticles are indeed quite coherent with the matrix, characterized by a sharp, flat, and non-diffused interface between the oxide and the host matrix [39].

the preferential bias of interstitials to dislocations arises as a consequence of the differing strain fields and their higher diffusion coefficient as compared to vacancies. The leftover vacancies keep on clustering to form bigger voids, leading to a steady swelling of the material. It should be noticed, that these processes at the primary stages of a radiation damage event play a decisive role in the long-term irradiation evolution of materials.

1.1.1 Development of radiation resistant materials

Developing better radiation resistant materials has been a challenge and it involves various optimizations at different levels, complying with the desired properties. Materials to be used in the core components should have good creep strength, low ductile to brittle transition temperature, resistance to irradiation, high thermal conductivity, low residual activation etc. In general, a compromise between high ductility and high mechanical strength has to be made, because materials with high ductility have low mechanical strength and vice versa. Austenitic steels, owing to their mechanical strength up to 650 °C, have traditionally been preferred. But, they have a fcc structure, which is a compact structure, thus, prone to void swelling. Efforts were put to enhance their resistance against void swelling by processes like cold working and by adding precipitates of N, P and Ti which trap helium. These precipitates also pin the dislocations, thus providing creep resistance. But, these steels have residual radioactivity due to the presence of Ni. Further at high irradiation doses, they show a high rate of void swelling, as the protective microstructure breaks down. Thus, it was understood that austenitic steels cannot be the candidate materials for future fusion and fast breeder reactors.

Ferritic/Martensitic steels containing 9-12% Cr with bcc structure are more swelling resistant than austenitic steels at lower He levels and He/dpa ratios. The resons include their bcc structure, smaller dislocation bias, higher self-diffusion coefficient, lower He concentrations in the absence of Ni and high sink densities. However, for bcc metals, a characteristic ductile to brittle transition (DBTT), at a temperature 300-400 K, separates the low-temperature brittle fracture regime from the high-temperature ductile fracture regime. Further, the strength of the unirradiated fer-
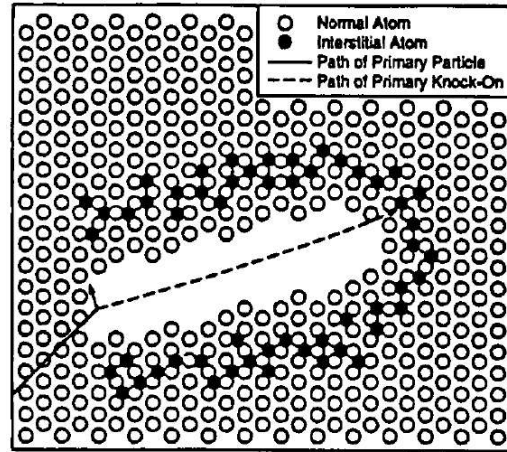
Figure 1.2 – The damage state as a locally depleted zone surrounded by a mantle of interstitial atoms, as pictured by Brinkman. Figure taken from Ref. [34].

Void swelling is basically an isotropic volumetric change of a material under irradiation and it occurs due to the formation and growth of voids in solids. A void distribution after neutron irradiation in type 316 austenitic steel is shown in Fig. 1.1a. In Fig. 1.1b, one can see the dimensional changes in fuel bundles upon exposure to neutron irradiation. Evidently, void swelling drastically reduces the residence time of structural materials.

TEM observation of voids in irradiated metals have shown that the basic mechanism for the formation of voids is due to the condensation and supersaturation of vacancies [35]. The vacancies which survive after the initial displacement cascade event start agglomerating and in association with gas (generally helium produced by transmutation) cluster to make bigger voids. Brinkman in 1954, estimated the mean free path between displacement events as about an order of one atomic distance. This lead him to conclude that in the initial stages of a radiation damage event, a 'production bias' between the number of interstitials and vacancies occurs [34]. He pictured the damage state as a local depleted zone surrounded by a mantle of interstitial atoms, as shown in Fig. 1.2. It is suggested that events immediately after the cascade formation, which lead to a partitioning of interstitials and vacancies, result in an ultimate imbalance of available vacancy versus self-interstitial point defect concentrations [33]. While vacancies and self-interstitials are created in equal numbers by irradiation, and a fraction is lost by mutual recombination,

spike. The thermal spike persists for only a few picoseconds before the heat in the cascade-region gets dissipated to the surrounding lattice. However, the period of thermal spike is very important, as in it many atomic rearrangements take place, since the fast moving atoms in the cascade-region can even relocate themselves to the equilibrium lattice sites, thus reducing the total number of point defects generated during the ballistic phase [32]. At the end of the thermal spike, remnants of the cascade remain, which are termed as the primary state of damage and these include the point defects such as Frenkel pairs, interstitials, vacancies, and also extended defects such as dislocation loops etc. Further, an extensive mixing of atoms on lattice sites also takes place, contributing to a local chemical disorder. Irradiation can also cause the creation of transmutation impurity elements such as helium which precipitates as gas bubbles. These gas bubbles act as the nucleation sites for growing voids and grain boundary creep cavities. Helium also gets segregated to the grain boundaries, thereby degrading the mechanical properties of the materials.

(a)　　　　　　　　　　　　　　(b)
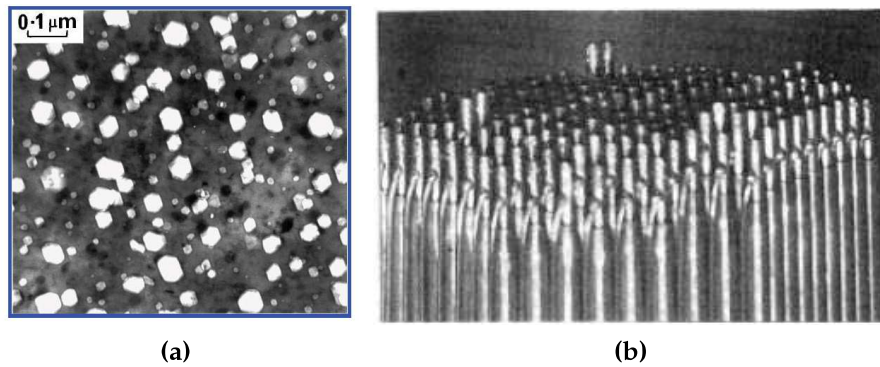
Figure 1.1 − (1.1a) Transmission electron micrograph of a typical void distribution in type 316 austenitic steel after neutron irradiation to 60 dpa at 500°C; (1.1b) The dimensional changes in fuel bundles upon exposure to neutron irradiation. Figures taken from Ref. [33].

The agglomeration of point defects leads to microstructural changes such as changes in the dislocation structures, radiation-induced solute segregation, precipitation, embrittlement, uniform loss of strain ductility, irradiation creep, void swelling, a large reduction in ductility, etc [33]. In the context of fast reactors and fusion reactor concepts, void swelling is the most detrimental effect of irradiation.

microstructure evolution [4]. However, these long-term radiation effects depend crucially on the initial process of radiation damage event [5], i.e, displacement cascades. A thorough understanding of RD can be achieved if we understand the processes involved in displacement cascades properly. Molecular Dynamics (MD) is the most efficient computational technique to probe atomic systems and it can provide the useful insights into the displacement cascade process. If the interatomic potentials used in MD are realistic, they can effectively model the period of thermal spike and the associated atomic arrangements. Further, when analysing the radiation stabilities of materials, the role of interatomic potentials acquires even more importance.

In this chapter, we elucidate the points discussed up to now and give a comprehensive picture of the thesis. In section 1.1, we discuss the problem of RD and its effect on materials and discuss briefly the logical steps towards making better radiation resistant materials. Then we discuss the effects of radiation damage on Y-Ti-O nanoclusters and motivate about the importance of understanding the processes in displacement cascades. Then we make a short discussion on how amorphization in materials is predicted, and the way MD can provide some useful insights into the mechanism of displacement cascades in materials. The importance of interatomic potentials for MD simulations is also discussed. In section 1.2, we highlight the problem addressed in the thesis and briefly discuss the contents of all the chapters.

1.1   Radiation damage in materials

A radiation damage event commences with the bombardment of highly energetic particles on the crystalline solids, producing lattice defects. The collision of an impinging energetic ion produces a primary knock-on atom (PKA) in the target matrix which in turn collides with other lattice atoms, creating a sequence of collisions known as displacement cascade. Typically, after the generation of PKA, in about 0.2-0.5 psec the energy of the recoil atom falls below the threshold energy and this marks the end of the ballistic phase of the cascade. At this point, all the atoms in the cascade-region are set into motion, and this stage is known as thermal

Chapter 1

Introduction

In this chapter, we give an outlook of the larger context of the problem tackled in the thesis. We discuss the general problem of radiation damage, and the various ways the irradiation behavior of materials can be understood.

The core structural materials of nuclear reactors face intense irradiation, high temperature and large thermal gradients that deteriorate their mechanical, elastic and thermal properties, thereby severely reducing their operational life [1]. Resistance to radiation damage (RD) is one of the most crucial properties a material must possess for it to be used as a structural material for nuclear reactors [2]. The radiation resistant materials are required for the waste forms, for the fuel, and for various important applications in the nuclear fuel cycle [3].

In the quest for developing better radiation resistant materials, oxide dispersion strengthened (ODS) steels, owing to their excellent high-temperature strength and creep resistance [2], have emerged as one of the most promising candidate materials for the advanced fast breeder and fusion reactor concepts. Y_2O_3, Y_2TiO_5, and $Y_2Ti_2O_7$ precipitates are the basic ingredients of ODS steels. These oxide nanoparticles enhance the mechanical strength of steels [8], are quite stable at high temperatures as well as at high neutron irradiation dose [9], and are believed to provide radiation resistance [2].

Predicting the in-service performance of these Y-Ti-O oxide nanoparticles requires a detailed understanding of the mechanisms of defect accumulation and

1

Summary

In this chapter, we discussed the basics of MD, DFT and ring analysis and explored the relationships of different polyhedra connectivities with the corresponding rings encompassing them. These concepts will be useful for our subsequent studies.

its polyhedra.
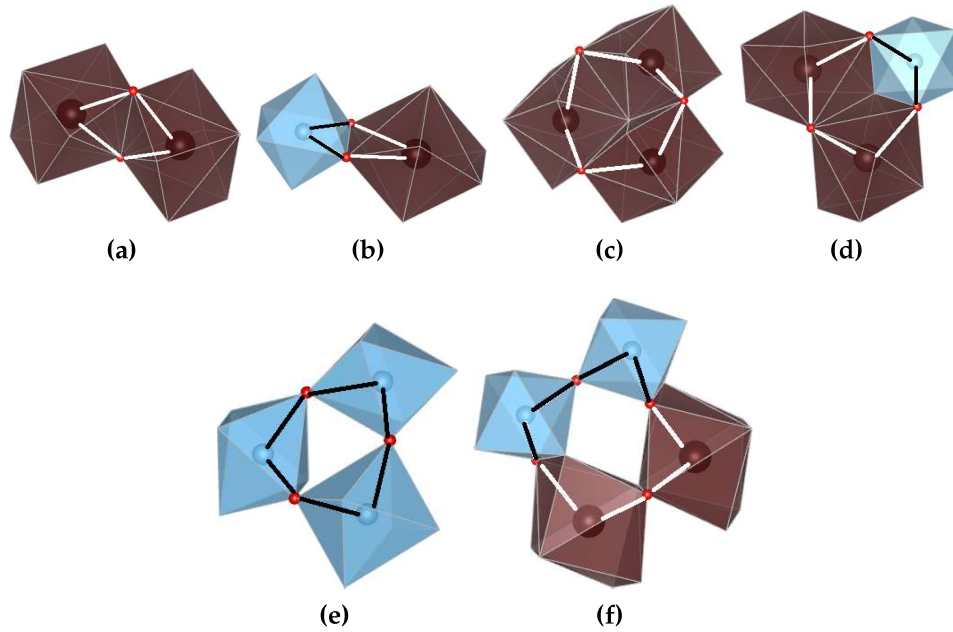
Figure 2.4 – Rings in $Y_2Ti_2O_7$: *4-rings*: (2.4a) Y_2; (2.4b) Y_1Ti_1. *6-rings*: (2.4c) Y_3; (2.4d) Y_2Ti_1; (2.4e) Ti_3. *8-rings*: (2.4f) Y_2Ti_2. Brown: Yatoms; Blue: Ti atoms; Red: O atoms.

The details about the structure of $Y_2Ti_2O_7$ matrix are discussed in section 4.4.2. $Y_2Ti_2O_7$ lattice can be visualized as made up of YO8 and TiO6 polyhedra units. As seen in figures 2.4a and 2.4b, 4-rings in $Y_2Ti_2O_7$ comprise of Y_2 and Y_1Ti_1 rings, while there are no Ti_2 rings present in this system. Thus, edge-sharing is only between Y polyhedra with other Y polyhedra, or Y polyhedra with Ti polyhedra. Ti polyhedra share only corners with each other. The number of Y_1Ti_1 4-rings are twice the number of Y_2 rings which indicates that the two different sublattices, i.e, YO polyhedra sublattice and TiO polyhedra sublattice contribute in constraining each other in a major way.

As shown in figures 2.4c-2.4e, 6-rings in $Y_2Ti_2O_7$ comprise of Y_3, Y_2Ti_1 and Ti_3 rings. In this case, there are Ti_3 rings having all Ti polyhedra sharing their corners. This makes a difference with Y_2TiO_5 matrix where Ti sublattice is completely detached from each other. 8-rings, as shown in Fig. 2.4f, comprise only of Y_2Ti_2 rings where Ti polyhedra share corner with each other, Y polyhedra share edges with each other, and Y and Ti polyhedra share edges with each other.

dra lattice is quite constrained due to the edge-sharing of Y polyhedra with each other as well as with Ti polyhedra. Ti polyhedra matrix, on the other hand, doesn't have many constraints, and it can be said, it provides only more constraints to Y polyhedra matrix.
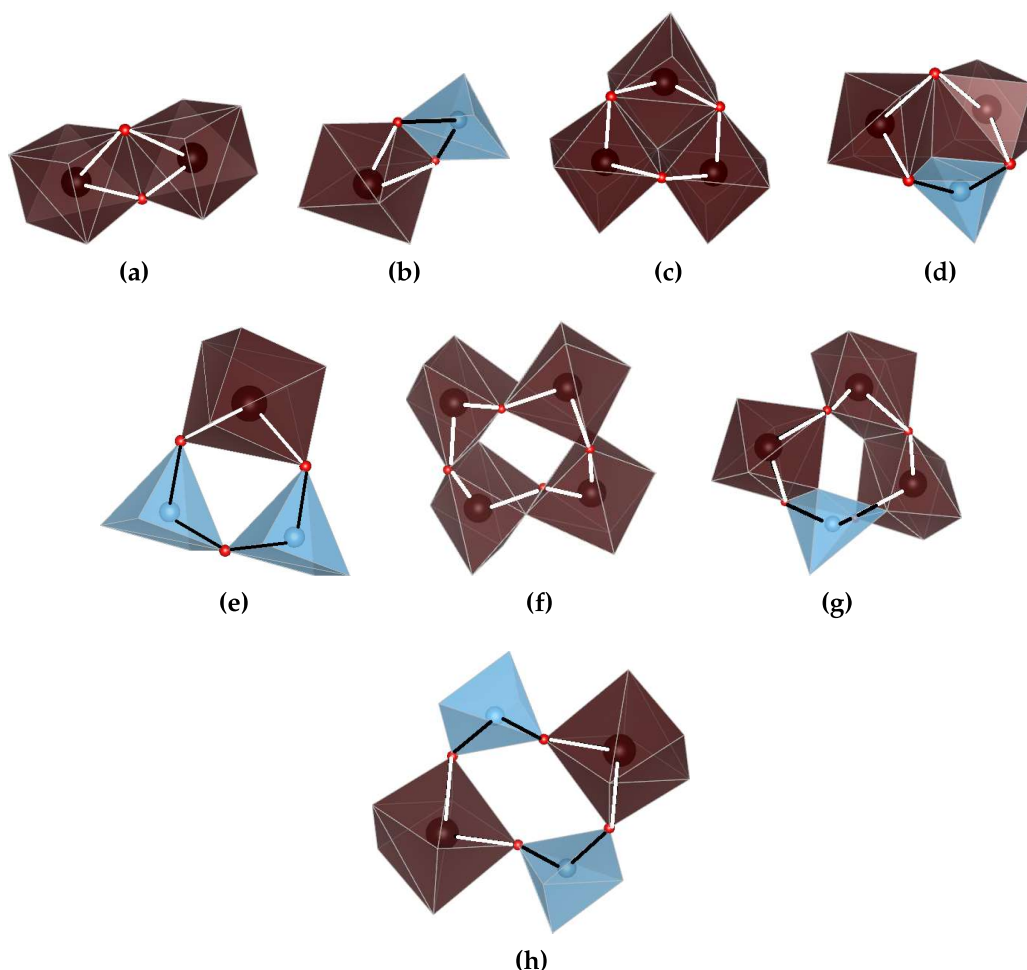
Figure 2.3 – Rings in Y_2TiO_5: *4-rings*: (2.3a) Y_2; (2.3b) Y_1Ti_1. *6-rings*: (2.3c) Y_3; (2.3d) Y_2Ti_1; (2.3e) Y_1Ti_2. *8-rings*: (2.3f) Y_4; (2.3g) Y_3Ti_1; (2.3h) Y_2Ti_2. Brown: Y atoms; Blue: Ti atoms; Red: O atoms.

The type of 6-rings in Y_2TiO_5 are Y_3, Y_2Ti_1 and Y_1Ti_2 in the ratio 5:6:1 respectively. As shown in figures (2.3c) and (2.3d), Y_3 6-rings as well as Y_2Ti 6-rings represent edge-sharing polyhedra, while Y_1Ti_2 rings (Fig. 2.3e) have all corner sharing polyhedra.

Order 8-rings in Y_2TiO_5 comprise of Y_4, Y_3Ti_1 and Y_2Ti_2 rings in the ratio 6:8:1 respectively. Ti_4 and Y_1Ti_3 8-rings are completely absent. Y_4 8-rings comprise of all edge-sharing Y polyhedra. Y_3Ti_1 ring has mixed corner and edge-sharing between
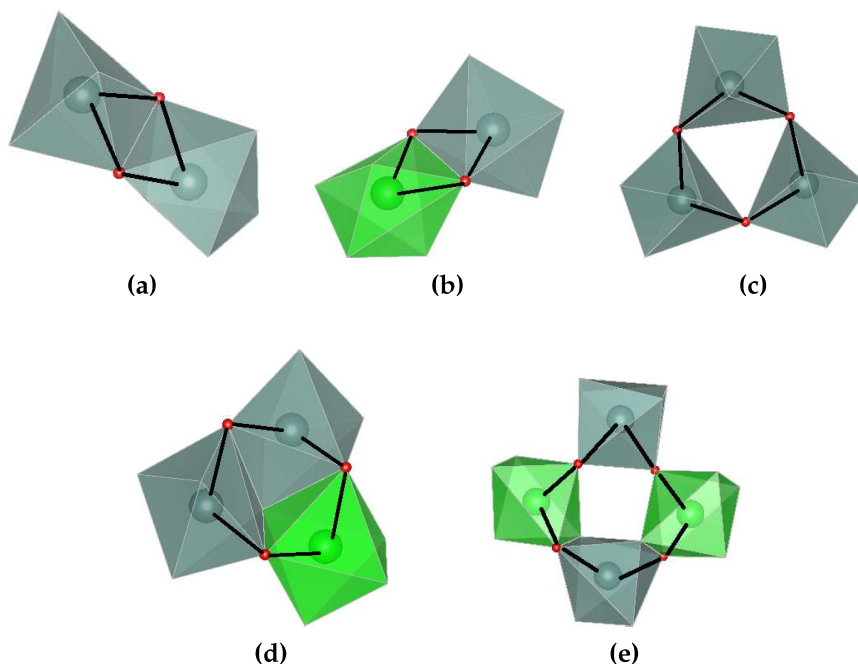
Figure 2.2 – Rings in Y_2O_3 : *4-rings*: (2.2a) Y_a-Y_a polyhedra edge-sharing in a Y_2 ring; (2.2b) Y_a-Y_b polyhedra edge-sharing in a Y_2 ring. *6-rings*: (2.2c) 3 Y_a polyhedra in a Y_3 ring; (2.2d) 2Y_a, 1Y_b polyhedra in a Y_3 ring. *8-rings*: (2.2e) 2Y_a, 2Y_b polyhedra in a Y_4 ring. Silver green: Y_a atoms; Light green: Y_b atoms.

The structure of Y_2O_3 matrix is discussed in section-3.2. Y_2O_3 matrix has two symmetrically inequivalent cation sites, Y_a and Y_b. Both Y_a and Y_b atoms sit in octahedra whose corners are oxygen atoms. Thus, Y_2O_3 lattice can be visualized as made up of Y_aO6 and Y_bO6 cation octahedra. Figures 2.2a and 2.2b show 4-rings in Y_2O_3 crystal involving edge-sharing Y polyhedra. 6-rings, as shown in figures 2.2c and 2.2d comprise of corner sharing polyhedra and edge-sharing polyhedra respectively. 8-rings, as shown in Fig. 2.2e comprise of three edge-sharing polyhedra and one corner sharing polyhedron. One should notice, that 4-rings always represent an edge-sharing between the corresponding polyhedra. However, a similar statement cannot be made in general for higher order rings.

The structure of Y_2TiO_5 matrix is discussed in section 4.4.2. Y_2TiO_5 lattice can be visualized as made up of YO7 and TiO5 polyhedra units. In Y_2TiO_5, there are two types of 4-rings: Y_2 4-rings (Fig. 2.3a) and $Y_1 Ti_1$ 4-rings (Fig. 2.3b), indicating that edges are being shared between Y polyhedra and between Y, Ti polyhedra respectively. The absence of Ti_2 4-rings indicates that none of the Ti polyhedra share edges with other Ti polyhedra, a feature common for $Y_2Ti_2O_7$ too. Y polyhe-

reason for taking an alternate sequence of cations and anions is, we want to track the connectivities between different cation polyhedra, which are connected by anions (oxygen). Second, we take any general cation (not particularly Y or Ti atom) in this definition, as we do not want to discriminate between two rings of the same order having different sequence or species of cations (for example, if a system has only one ring, say Y-O-Y-O ring and that gets replaced by Y-O-Ti-O ring, still the count of rings in this system remains one). This is done so that the case of cation antisite formation in Y-Ti-O systems is not counted as representing a loss of topology, as cation antisite formation is a favorable property of pyrochlores and it provides them amorphization resistance [27]. Further, an n-ring in Y-Ti-O systems has equal number ($n/2$) of anions and cations in it. Since O atoms always make a link between two cations in a ring, they would not be written explicitly, and we simply denote, for example, a 6-ring having the sequence Y-O-Y-O-Ti-O as a Y_2Ti_1 ring. In all the calculations of rings, we have not taken periodic boundary conditions. Rings up to an order 12 are searched. Table 2.1 lists the cut-offs taken for assigning the connectivities between the pair of cations and anions in a ring. These values are obtained by optimizing the bond cut-off for which the coordination number of cations in the corresponding lattice is obtained. These values roughly fall in between the first and the second peaks of the partial RDF of the considered pair of anion and cation.

Cut off	Y-O (Å)	Ti-O (Å)
Y_2O_3	3.2	N.A
Y_2TiO_5	2.9	2.5
$Y_2Ti_2O_7$	3.2	2.8

Table 2.1 – Cut-offs taken for ring analysis.

The common feature of the rings in Y-Ti-O crystal systems is, that in the ideal crystals of all of these materials, only 4, 6 and 8-rings are present. Now we describe in detail about the type of rings present in the crystal structures of these systems, and explore their relationships with the connectivities between the different cation polyhedra.

nar graph contains 5 primitive rings, 1 of order 6, and 4 of order 8. Now, suppose, in this graph, the path EIJH did not exist. Then, even if the path EFGH gets so much distorted, so that it acquires the configuration originally of the path EIJH (or, any other configuration, provided the links in EFGH path do not break), then also, the corresponding ring encompassing that path, for example, the ring ABCDEFGH would not be considered as broken. This feature of the ring analysis enables it to decipher the underlying topology, while obviating the extra details. For instance, in any defect analysis which relys on comparing the disordered system with its initial crystalline counterpart, the aforementioned distorted system would be found to be having point defects (here, the original sites for F and G would be counted as vacancies). Similary, RDF plot also will show the peaks of the original system getting diffused in this distorted system and these analyses will simply mark the system as disordered. However, ring analysis will be able to provide the insight, that although the system has got distorted, yet its uderlying topology has not been disturbed.

Every crystal structure has its own signature primitive rings. For example, a cubic lattice shown in Fig. 2.1b has twelve 4-order primitive rings via an atom. However, in the case of amorphous systems, there will not be any signature rings and any random order of rings can be present in them. This concept is important in differentiating between crystalline and amorphous systems.

2.3.2 Description of rings present in Y-Ti-O systems

Now we analyze the signature rings present in the Y-Ti-O crystal systems. All the three Y-Ti-O crystal systems can be considered as made up of cation polyhedra i.e, a cation surrounded by oxygen atoms. The oxygen atoms make connections between the different cation poyhedra. The study of the various types of rings provides the details of the connectivities between these polyhedra in their respective lattices.

Our aim is to study the compactness of polyhedra and their connectivities. Thus, for these studies, we will consider only those rings which have an alternate sequence of anions (oxygen) and cations. This is done for two reasons. First, the

it will be simply called as an *n*-ring.

Rings can be defined in many ways. For instance, minimal rings [106], rings of interest, strong rings and very strong rings [107] etc. In this thesis, we obtain the topological signature by analyzing *primitive* rings [108] as implemented in RINGS code [14]. A primitive ring is defined as the shortest possible ring for a given order. If between any pair of nodes on a ring, there exists a path that is shorter than that ring, then that path is called a shortcut of that ring. A primitive ring is a ring without any shortcut, or alternatively a ring that cannot be decomposed into smaller rings. In all of our subsequent discussions in this thesis, where ever a mention of rings comes, it should be understood as that for primitive rings, if not otherwise stated.

(a)   (b)
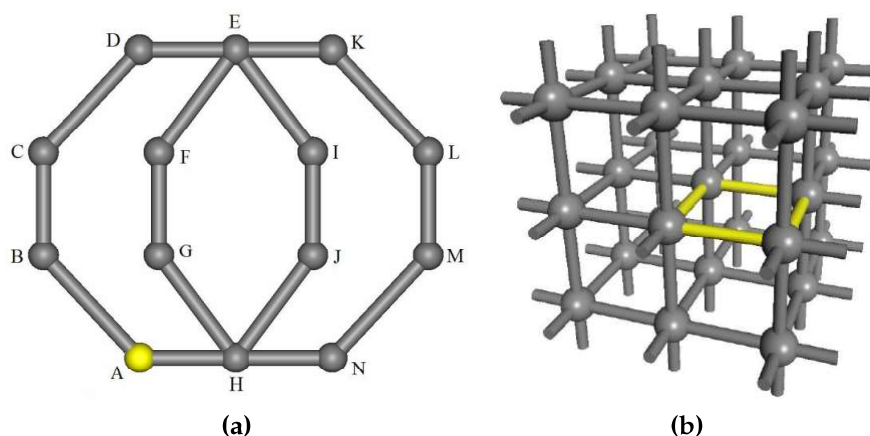
Figure 2.1 – (2.1a) Planar graph for demonstrating the distinction between primitive and non-primitive rings; (2.1b) A cubic structure showing one of the 12 primitive 4-rings starting at the central atom (4 in each orthogonal plane). Figures are taken from Ref. [109].

The concept of primitive rings can be understood from the planar graph shown in Fig. 2.1a. The closed paths ABCDEFGH, ABCDEIJH, EKLMNHJI and EKLMN-HGF are primitive 8-rings, while EIJHGF is a primitive 6-ring. This is because, for these rings, there doesn't exist any ring which has a smaller order and provides a short-cut to come back to the same initial node. However, the 10-ring ABCDEKLMNHA is not a primitive ring, as it encompasses lower-order rings. For example, if we choose the initial node as node H, then ABCDEFGH, ABCDEIJH, EIJHGF, etc., all provide shortcuts with respect to the 10-order ring path. This pla-

Now we discuss some of the aspects of ring analysis and discuss the properties of rings in Y-Ti-O systems.

2.3.1   Graph theory and topological analysis

A graph is defined as an object comprising of two sets, a vertex set V and an edge set E whose elements are two-element subsets of V. The elements of the vertex set are termed as vertices, or *nodes* and elements of the edge set are known as *edges*. Edges connect two elements (nodes) of the vertex set. It is possible that two nodes of the vertex set don't have any edge between them, and hence, are disconnected.

With reference to a given problem and depending upon the particular characteristics one wants to analyze, the nodes and edges in a network can be defined. For example, say three cities A, B and C are linked via roads while A and B are also connected by an aerial route. Then, if one defines road-connectivity as representing the edges, all the cities (*nodes*) are edge-connected to each other, while, if only aerial connectivity is considered as an edge, then only A and B would be considered as edge-connected while C would be disconnected to both of them. The definition of an edge can be even more general, say the common language between the two cities, a similar kind of landscape, etc.

Three-dimensional structures can be described quantitatively by an analysis of the shortest number of connections (edges) joining sets of nodes to form a path. Any atomic system, with its 3-dimensional arrangement of atoms, is an ideal system for a graph theoretical analysis. An obvious choice for the nodes is the atoms of the system, while edges can be defined by the bonds between two atoms. Now we define some of the technical terms which are important for our further analysis. These are *ring* and *order* of a ring.

Ring: A ring is a closed path which starts from a given node, traverses a continuous path via different edges and nodes, and returns back to the same initial node.

Order: Order of a ring is defined as the number of nodes (atoms) present in a given ring. Thus, a ring containing n number of nodes has an order equal to n and

smaller will be the basis set and higher will be the calculation speed. However, if a very small number of basis sets is taken, that may not be able to represent the function properly and thus lead to spurious results. Thus, one must perform the convergence test by calculating a property with respect to the size of the basis set.

2.2.6   k-point sampling

In an infinite crystal, there are infinite number of allowed values for Bloch vector. However, it is impossible to take into account the infinite number of **k** vectors and hence a reasonably large number of **k** vectors are used to get a good description of the properties of a system. As the summation over the **k** vectors is involved in the self-consistent calculations of the electronic structure and other properties, a compormise needs to be made between the required accuracy and the computational time. The symmetry of the Brillouin zone allowed to work in the irreducible part of the Brillouin zone and a suitable **k** grid can be arrived using the **k** grid convergence test. Different **k** grid sampling schemes are available and the Monkhorst-Pack [105] is a popular scheme which is used in the DFT calculations carried out in this work.

2.3   Ring analysis

Ring analysis is a manifestation of graph theory, and finds its basis in topological arguments. A topology based analysis can be very useful in probing disordered systems and it can complement the other tools for analyzing disorder. In highly energetic situations, the usual tools to measure disorder may not remain very appropriate. This is because, most of the defect detection analyses rely on a comparison of the static reference system with the disordered system. However, in a highly energetic situation, the crytalline system is free to move and distort and thus, defect calculations based upon static reference structure may not remain very useful, and one should use topological methods instead.

The topological connectivity analysis used in this thesis is ring analysis. Ring analysis can provide information about the intermediate-range order in systems.

There exist various choices for $f(\rho(\mathbf{r}), \nabla\rho(\mathbf{r}))$, and the schemes developed by Perdew, Burke and Ernzerhof (PBE) [100] and Perdew-Wang [101, 102] are some of the most popular choices. In this work, we have used PBE exchange-correlation functional.

2.2.4 Pseudopotentials

In the KS equations, all the electrons in the system are considered. This makes the calculations computationally highly intensive. However, one can simplify this problem by noticing that the core electrons are strongly bound to nucleus by the coulombic interaction and it is the valence electrons which are important in most of the physical and chemical properties. The core electron orbitals exhibit strong oscillations and to take them into account large number of plane waves (which implies a very high value of E_{cut}) are required which increases the computational efforts enormously. This computational difficulty is overcome by approximating the potential in the core region of the atom by an effective pseudopotential. The process of replacing wave functions and potentials by the respective pseudo functions is called pseudisation. The usage of pseudopotentials screens the singularity, which results in weaker oscillations so that a smaller number of plane waves suffice. The many-body effects of the core states are included in the pseudopotential as the valence states are orthogonal to the core states.

There are various kinds of pseudopotentials which have been implemented in the DFT codes, such as: (a) norm-conserving, (b) ultrasoft, and (c) projector augmented wave (PAW) [103, 104]. In this work, we have used PAW pseudopotentials.

2.2.5 Plane wave cut-off

Ideally, the KS wavefunction can be represented by an infinite number of basis set, but that is practically impossible. Hence a cut-off criterion is required. For a crystalline solid, a Bloch state can be represented using the plane waves. It is known that contribution of the plane wave with higher wave vector is much less than that due to plane waves with smaller wave vector. Thus, it is possible to truncate the infinite series with some cut-off energy (E_{cut}). Smaller the cut-off energy,

state density and the total energy. Up to this point DFT is an exact theory, but unfortunately, the analytic expression for $E_{XC}[\rho]$ is not available and it has to be approximated. In the next sections, we discuss two of the most popular approximate forms of XC functionals.

2.2.2 Local Density Approximation (LDA)

Local density approximation (LDA) is the most popular approximation for the exchange-correlation functional. The basis of LDA lies in the theory of homogeneous electron gas and assumes that the variation of the electronic density is smooth in space. Thus, the XC energy at a point $\mathbf{r}$, with density $\rho(\mathbf{r})$ is taken to be equal to the XC energy of a uniform electron gas of the same density. The XC functional under LDA is written as :

$$E_{XC}^{LDA}[\rho] = \int \rho(\mathbf{r})\epsilon_{XC}(\rho(\mathbf{r}))d\mathbf{r} \qquad (2.36)$$

Here, $\epsilon_{XC}(\rho(\mathbf{r}))$ is the exchange-correlation energy density of a homogeneous electron gas of density ρ.

The exchange term in this functional can be expressed as the exact expression of the homogeneous electron gas, but the representation of the correlation part varies in different versions of the LDA. Some of the popular versions are Perdew-Wang (PW) [98] and Vosko-Wilk-Nusair (VWN) [99].

2.2.3 Generalized Gradient Approximation (GGA)

Although LDA is a very simple and a highly popular functional form for the XC functional, in real systems, the electronic density is not always smooth and can vary rapidly. Thus, not only the electronic density, but also its gradient $|\nabla\rho(\mathbf{r})|$ becomes important for a better description of the XC potential. This is called the generalized gradient approximation (GGA). In this approximation, the exchange energy is written as:

$$E_{XC}^{GGA} = \int f(\rho(\mathbf{r}), \nabla\rho(\mathbf{r}))d\mathbf{r} \qquad (2.37)$$

the universal energy functional.

The total energy functional $E[\rho]$ can be written as:

$$E[\rho] = 2 \left[T[\rho] + \int V_{Ne}(\mathbf{r})\rho(\mathbf{r})d^3r] + \frac{e^2}{2} \int \frac{\rho(\mathbf{r})\rho(\mathbf{r}')}{|\mathbf{r}-\mathbf{r}'|} d^3r d^3r' + E_{XC}[\rho] + V_{NN}(\{\mathbf{R}_i\}) \right] \tag{2.32}$$

Where, $T[\rho]$ is the kinetic energy of the electronic system, V_{Ne} is the interaction potential between the electrons and nuclei, V_{NN} is the Coulomb interaction between the nuclei, $E_{XC}[\rho]$ is the exchange-correlation (XC) functional and $\rho(\mathbf{r})$ is the electronic density at $\mathbf{r}$. This equation is for the non-interacting system and all the quantum mechanical corrections to take into account their correlation as well as the exchange interaction due to their Fermionic nature is included in the exchange-correlation functional $E_{XC}[\rho]$. The minimization of the energy functional $E[\rho]$ yields the Kohn-Sham equations.

The ground state density $\rho_0(\mathbf{r})$ is defined as the sum over the non interacting one particle densities given as:

$$\rho(r) = \sum_{\sigma} \sum_{j=1}^{N_\sigma} \left| \phi_j^\sigma(\mathbf{r}) \right|^2 \tag{2.33}$$

Where σ represents the spin of the electrons and N_σ is the corresponding number of electrons. The single particle wave functions $\phi_j^\sigma(\mathbf{r})$ are determined by Kohn-Sham equations:

$$\left[-\frac{\hbar^2}{2m}\nabla^2 + V_{ion}(\mathbf{r}) + V_H(\mathbf{r}) + V_{XC}(\mathbf{r}) \right] \phi_j^\sigma = \varepsilon_j \phi_j^\sigma \tag{2.34}$$

Where, $V_H(\mathbf{r})$ is Hartree potential which represents the Coulomb interaction between electrons, $V_{XC}(\mathbf{r})$ is the exchange-correlation (XC) functional. It is defined as the functional derivative of E_{XC}, as:

$$V_{XC}(\mathbf{r}) = \frac{\delta E_{XC}[\rho(\mathbf{r})]}{\delta\rho(\mathbf{r})} \tag{2.35}$$

Equations 2.33 and 2.34 should be solved self-consistently to obtain the ground

$$\hat{V}_{int}(\mathbf{r}_i, \mathbf{r}_j) = \frac{e^2}{|\mathbf{r}_i - \mathbf{r}_j|} \qquad (2.31)$$

The first theorem of Hohenberg and Kohn (H-K) [96] is as follows:

For a set of interacting particles, there is a one to one correspondence between the external potential $V_{ext}(\mathbf{r})$ and the ground state density $\rho_0(r)$, upto a constant shift of the potential.

The corollary of this theorem is, once the ground state density is known, the total Hamiltonian is also known. The knowledge of the Hamiltonian leads to determination of all the eigenfuntions and hence, all the properties of the system.

The second H-K theorem is as follows:

For any external potential $V_{ext}(\mathbf{r})$, a universal functional for the energy $E[\rho]$ can be defined. The exact ground state energy of the system is the global minimum value of this functional, and the density that minimizes the functional is the exact ground state density $\rho_0(r)$.

The corollary of this theorem is that the functional $E[\rho]$ is sufficient to determine the exact ground state energy and density.

2.2.1 Kohn-Sham equations

Kohn and Sham, in 1965 proposed an ansatz, which makes the application of DFT [97] to large-scale systems. Since H-K theorem is valid for any kind of particles, not necessarily an electronic system, two completely different systems having the same ground state density should correspond to the same external potential $V_{ext}(\mathbf{r})$. That means the interacting electronic system can be replaced by an auxiliary independent particle system with the same ground state density as that of the interacting system. This replacement of the interacting electronic system with an independent particle system is known as Kohn-Sham ansatz and it provides two main advantages. First, the difficult problem of tackling interacting system gets reduced to calculating the properties of the non-interacting system. Second, the combination of the Hohenberg-Kohn theorems and the Kohn-Sham ansatz leads to the formulation of approximations that are needed to construct the formulation of

that atom is identified as an interstitial. The cut-off radius taken is 50% of the bond lengths of Y-O and Ti-O bonds for Y and Ti atoms respectively, while for O atoms, it was taken to be an average of the cutoffs defined for Y and Ti atoms. The topological order of the radiation damaged system can be probed using ring statistics which is explained in detail in the section 2.3.

Other properties such as MSD, temperature, etc., are calculated as described in the earlier discussion. Calculation of the cascade volume is carried out by approximating the cascade volume by an ellipsoid. The center of mass (C.O.M) of the defects as the center of the ellipsoid, while the x, y and z axes of the ellipsoid are quantified by calculating the standard deviation of defect coordinates from the C.O.M along the three mutually perpendicular axes.

2.2 Density Functional Theory

Density functional theory (DFT) is a powerful, and formally exact formulation for solving the many-body Schrödinger equation. The essence of DFT is the use of electronic density, instead of a many-electron wavefunction, which makes this formulation highly efficient to calculate the physical properties. The advantage of using density instead of a many-particle wavefunction is the reduction of the degree of freedom of the original problem from 3N to 3 (where, N is the total number of particles). The basis of DFT lies in the two theorems proved by Hohenberg and Kohn [96] in 1964. Its formulation is completely general, and is applicable for any interacting system of particles, in an external potential $V_{ext}(\mathbf{r})$.

Let a Hamiltonian operator for a system of interacting particles in an external field $V_{ext}(\mathbf{r})$ is written as:

$$\widehat{H} = \frac{-\hbar^2}{2m} \sum_i \nabla_i^2 + \sum_i V_{ext}(\mathbf{r}_i) + \frac{1}{2} \sum_{i \neq j} \widehat{V}_{int}(\mathbf{r}_i, \mathbf{r}_j) \qquad (2.30)$$

For an electronic system, the interacting potential between particles is the Coulomb potential i.e,

31

generation of the PKA. Simulation box must be adequately large so that the cascade doesn't touch any of the boundaries of the simulation box, as that will lead to the self-interaction of the cascade with its own images and will lead to spurious effects. The simulation cell is divided into two regions, the inner region which is big enough to contain the cascade fully, and the outer region typically of 2-3 atomic layers wide, which corresponds to the surroundings. Before the initiation of an RD event, the whole simulation box is first relaxed to the desired initial equilibrium temperature and pressure using an NPT ensemble. After this, the outer region is linked to an NVT ensemble, while the inner region is linked to an NVE ensemble. The reason for this strategy is, in the inner region where the cascade is generated, a lot of energy is imparted and this leads to an immense rise in the temperature, which should be modeled properly. On the other hand, the outer region, being linked to an NVT ensemble, maintains a constant temperature, just the way in real conditions, the surroundings being quite large, do not get any noticeable change in the overall temperature due to the cascade occurring in a small localized region. After defining all the ensembles, a primary knock-on atom (PKA) with a given energy and direction is initiated. In all the cascade simulations described in this thesis, the initial position of PKA is taken to be at the center of the simulation box. Since atoms move with very high speeds in the ballistic phase of the cascade, while later slow down as the thermal spike and annealing stages arrive, it is appropriate to take a variable timestep approach for describing the process efficiently as well as taking care of the total simulation time.

The radiation damaged system can be analysed using various tools such as RDF, the number of point defects, the topological order in the system etc. Some of the techniques to identify the point defects are such as the Wigner-Seitz cell method [95], the equivalent sphere analysis [30], number of displaced atoms criteria, etc. In this work, we have used the equivalent sphere (ES) analysis to analyze the number of point defects, under which a cut-off radius r_e is defined and if any atom is not found within a sphere of this radius centered around a lattice site, that site is identified as a vacancy. Similarly, if an extra atom comes within this sphere,

Temperature

Temperature of a system is calculated using the equipartition theorem, according to which each degree of freedom of an atom has on average an energy$= \frac{1}{2}K_B T$. Thus, the temperature can be calculated using average of the kinetic energy.

$$K = \frac{3}{2}NK_B T \tag{2.26}$$

where, N is the total number of atoms, K_B is the Boltzmann constant.

Mean square displacement and diffusion coefficient

Mean square displacement is calculated as:

$MSD = < (\mathbf{r}(t) - \mathbf{r}(0))^2 >$

Diffusion coefficient can be easily calculated from MSD, using Einstein's equation:

$$D = \lim_{t \to \infty} \frac{1}{6t} MSD \tag{2.27}$$

Pressure

Pressure is calculated using Virial theorem.

$$W(\mathbf{r_1}, \mathbf{r_2}, ..., \mathbf{r_N}) = \sum \mathbf{r_i}.\mathbf{F_i^{Tot}} \tag{2.28}$$

$$PV = NK_B T + \frac{1}{D} \left\langle \sum_{i=1}^{N} \mathbf{r_i}.\mathbf{F_i} \right\rangle \tag{2.29}$$

where $\mathbf{F_i}$ is the internal force acting on particles. It can be seen, for ideal gases, since $\mathbf{F_i} = 0$, this expression reduces to the ideal gas law, $PV = NK_B T$.

2.1.7 Simulation of displacement cascades using MD

Now we discuss a general methodology for modeling displacement cascades using MD. One practical way which is used for many of the MD simulations of cascades is to start modeling the whole process of displacement cascade from the initiation of a PKA, without concerning about the details about the source for the

will become weaker by the presence of other atoms.

2.1.6 Calculation of physical quantities

Up to now, we discussed the essentials of molecular dynamics simulations. Now we discuss the way physical quantities are calculated from a molecular dynamics trajectory. MD simulations provide the information about the velocities and positions of all the particles in the system and this information is sufficient to calculate most of the physical properties (not those which involve electronic effects) related to atomic systems. The calculation of physical properties in MD simulations amounts to taking time-averages of the physical properties over the system trajectory. Now we discuss some of the physical quantities calculated in MD simulations.

Potential Energy

Potential energy can be calculated at the time of force calculations as follows:

$$P(t) = \sum_{i>j} \sum_j V(|\mathbf{r}_i(t) - \mathbf{r}_j(t)|) \qquad (2.24)$$

Kinetic Energy

The total kinetic energy is calcualted as,

$$K(t) = \frac{1}{2} \sum_1^n m_i v_i(t)^2 \qquad (2.25)$$

Where, m_i and $v_i(t)$ are the mass and velocity of the ith particle.

Total Energy

Total energy can be calculated by adding the kinetic energy and the potential energy. In principle, the total energy, $E = K + P$ must be a conserved quantity. However, in practical simulations, there occurs a small deviation from the constant energy due to errors in integrating the equations of motion. These errors can be minimized by taking small timesteps.

metals, apart from electronic contribution to the many body effect, there can be a directional bias too. This effect can be dealt by using modified embedded atom method (MEAM) [94] potentials.

Stillinger-Weber potential: The popular potentials for covalent compounds are Stillinger-Weber and Tersoff potential. Stillinger-Weber potential models semiconductors with a classical model and is based on a two-body term and a three-body term which explicitly involves angles. The potential form can be written as:

$$V = \frac{1}{2}\sum_{ij} \phi(r_{ij}) + \sum_{ijk} g(r_{ij})g(r_{ik})(cos\theta_{jik} + \frac{1}{3})^2 \tag{2.20}$$

where θ_{jik} is the angle formed by the ij bond and the ik bond, and $g(r)$ is a decaying function with a cutoff between the first and the second neighbor shell. It can be seen, that this potential will prefer configurations for which $cos(\theta_{jik}) = -1/3$, i.e, those configurations where angles are as close as possible to the diamond-like tetrahedral structure.

Tersoff potential: Tersoff potentials are based on the concept of bond-order according to which, the strength of a bond between two atoms is not constant and depends upon the local environment. Tersoff potential can be written as:

$$V = \frac{1}{2}\sum_{ij} \phi_R(r_{ij}) + \frac{1}{2}\sum_{ij} B_{ij}\phi_A(r_{ij}) \tag{2.21}$$

where, ϕ_A is an attractive term, while ϕ_R is a repulsive term. Here, B_{ij} is not a constant and is a decreasing function of a coordination G_{ij} assigned to that bond.

$$B_{ij} = B(G_{ij}) \tag{2.22}$$

G_{ij} in turn, is defined as:

$$G_{ij} = \sum_{k} f_c(r_{ik})g(\theta_{jik})f(r_{ij} - r_{ik}) \tag{2.23}$$

Where $f_c(r)$, $f(r)$ and $g(\theta)$ are suitable functions. The basic idea is, the bond ij

not equal to one, is seen for several cubic materials in which many-body effects are dominent. An analysis of these systems using pair potentials can never show the Cauchy violation.

In this work, we have developed pair potentials for Y_2TiO_5 and $Y_2Ti_2O_7$. The potential form is a combined Coulomb and Buckingham potential. A detailed description of the development and methodology of these potentials is the subject matter of Chapter-4. These potentials have been then used for the displacement cascade studies discussed in chapter-5. We used the fitting procedure that involves the use of an extensive set of data obtained from the DFT calculations.

2.1.5.2 Many body potentials

In many materials, such as metals and semiconductors, it is seen that pair potentials are unable to properly reproduce the physical properties. When coordination increases, the local environment becomes more crowded and the bond strength decreases, due to Pauli's principle. Many-body potentials are important for metals and covalent compunds. Now we discuss some of the important many-body potentials:

Embedded Atom Method (EAM) potential: In EAM potentials, the system is treated as made of positive ions embedded in a sea of electrons. The energy of this system has two parts, one comes from the embedding energy representing the many-body effects, while the other contribution comes from the pair potential part. The basic assumption of EAM potentials is derived from density functional theory, according to which the total energy of an electronic system would be a unique functional of the electron density in which the ions are embedded. The total energy, therefore, can be written as:

$$V = \frac{1}{2} \sum_{i,j=1 (j \neq i)} \phi(r_{ij}) + \sum_{i=1}^{N} F[\rho_i] \tag{2.19}$$

where, $\phi(r)$ is a short ranged decreasing function of distance, F is the embedding function, and ρ_i is the electronic density at the site of the ith ion. Alkali and alkaline metals can be very well represented by EAM potentials, but for transition

2.1.5.1 Pair potentials

Pair potentials depend only upon the distance between two atoms. They are environment independent i.e, the interaction between two atoms remains unperturbed in the vicinity of any other atom. Pair potentials form a good approximation for the materials that have predominantly ionic interactions, or van der Waals interactions. For example, in the case of strongly ionic systems, the forces between two oppositely charged ions are predominantly governed by strong electrostatic force. After losing or gaining electrons, the anions and cations get closed shell configurations and the electronic cloud doesn't get purturbed when another ion apporaches [91]. Thus, the force between the two ions depends only upon the distance between them, and remains almost unperturbed from the influence of any other atom in the vicinity [12].

Some of the common pair potential functional forms are as follows:

Buckingham potential [92]:

$$U_{ij}^{Buckingham} = A_{ij}exp(-\frac{r_{ij}}{\rho_{ij}}) - \frac{C_{ij}}{r_{ij}^6} \tag{2.16}$$

Born-Mayer potential [18]:

$$U_{ij}^{Born-Mayer} = A_{ij}exp(-\frac{r_{ij}}{\rho_{ij}}) \tag{2.17}$$

Lennard-Jones potential [93]:

$$U_{ij}^{LJ} = \frac{A_{ij}}{r_{ij}^{12}} - \frac{C_{ij}}{r_{ij}^6} \tag{2.18}$$

But pair potentials have some limitations owing to the neglect of many-body effects, which are important for covalent or metallic systems. For example, the ratio between vacancy formation energy and cohesive energy is always predicted to be 1 by pair potentials, while in metals, it is about 1/4 or 1/3. Cauchy ratio between two elastic constants, i.e, C_{12}/C_{44} is equal to one for cubic materials governed by pair potentials. However, Cauchy violation, i.e, cubic materials having Cauchy ratio

An interatomic potential can be written as:

$$V(r_1, r_2, r_3 ... r_N) = \sum_i V(r_i) + \sum_i \sum_{j>i} V_2(r_i, r_j) + \sum_i \sum_{j>i} \sum_{k>j} V_3(r_i, r_j, r_k) + ... \quad (2.15)$$

where $V_1 =$ One-body term, representing an external field or some boundary condition.

$V_2 =$ Two-body term, i.e, a pair potential. In this case, the interaction of any pair of atoms depends only on their spacing and is not affected by the presence of other atoms.

V_3 and higher terms: these terms arise when the interaction of a pair of atoms is modified by the presence of other atoms.

The basic assumption in MD simulations of interacting atoms is the Born Oppenheimer approximation, under which the complete Hamiltonian of the nuclei-electronic system can be decoupled into a separate electronic and a nuclear Hamiltonian. This can be done, as for the same kinetic energy, electrons move at ~ 100 times the velocities of nuclei, and the time scales in which nuclei move, electrons can be assumed to follow them instantaneously. As discussed earlier, the way one calculates the interatomic interactions marks the difference between ab-initio MD and classical MD. In ab-initio MD, one solves the Schrödinger equation of the electronic Hamiltonian at every MD timestep, while in classical MD, empirical interatomic potentials are used. Since in this thesis we have used classical MD, now we briefly discuss about empirical potentials.

Constructing an empirical interatomic potential encompasses two main steps : (1) Selecting an analytical form for the potential; (2) Finding an actual parameterization for the functions that constitute the analytical form that has been chosen. Usually, the parameterization of the potential function is done using experimental or first principle calculations data. Now we discuss the various potential models which should be used for different type of materials. The broadest categorization of interatomic potential models is (1) pair potentials and (2) many-body potentials. Their description is as follows:

$$H_N = \sum_{i=1}^{N} \frac{\mathbf{p}_i^2}{2m_i s^2} + V(\mathbf{r}_1, ..., \mathbf{r}_N) + \frac{p_s^2}{2Q} + gkT \ln(s) \tag{2.13}$$

where, $\mathbf{p}_i$ are the momenta of particles, $m_i =$ mass, $V(\mathbf{r}_1, ..., \mathbf{r}_N)$ is the potential energy, Q is a fictional mass related to the extra degree of freedom, which describes the rate at which the temperature is changed, and T is the desired temperature of the canonical distribution. If d is the number of spatial dimensions, then the phase space now has a total $2dN + 2$ dimensions with the addition of s and p_s. The parameter g appearing in eqn. 2.13 is determined by the condition that a microcanonical distribution of $2dN + 2$ dimensional phase space of H_N yields a canonical distribution in the $2dN$-dimensional physical phase space. The variable s in the kinetic energy scales the kinetic energy in order to control its fluctuations. If the system is ergodic the stationary state can then be shown to be a canonical distribution.

The methods used to control pressure are analogous to the one used for temperature control. The system pressure is set by changing the simulation volume with a scaling factor. The scaling is done for both the simulation cell dimensions and the positions of particles. The Nosé-Hoover scheme is also available to control the pressure. A suitable combination of Nosé-Hoover thermostat and Nosé-Hoover barostat reproduces a proper NPT ensemble [89, 90].

2.1.5 Interatomic potentials

Interatomic potentials make the heart of any MD simulation and the accuracy of the data generated from MD simulations crucially depends upon the robustness of the interatomic potentials used. Given a potential function $V(\mathbf{r}_i)$, the force can be calculated as,

$$\mathbf{F}_i = -\nabla_i V(\mathbf{r}_1, ..., \mathbf{r}_N) \tag{2.14}$$

The potential function $V(\mathbf{r}_1, \mathbf{r}_2, \mathbf{r}_3 ... \mathbf{r}_N)$ describes how the potential energy of a system containing N atoms depends on the coordinates of the atoms $\mathbf{r}_1, \mathbf{r}_2, \mathbf{r}_3 .. \mathbf{r}_N$.

free boundary condition, fixed boundary condition etc. For molecules, one should use free boundary conditions. In fixed boundary conditions, atoms at the boundaries are kept fixed. Since this work deals with the simulation of crystals, PBC is the obvious choice, and hence we have used it in all the MD simulations carried out.

2.1.4 Defining ensembles

An ensemble is a collection of all possible systems which have different microstates but have an identical macroscopic or thermodynamic state. There exist different ensembles with different characteristics. The most common are NVE, NVT, NPT ensembles. A microcanonical ensemble (NVE) is characterized by a fixed number of atoms, N, a fixed volume, V, and a fixed energy, E. Thermodynamically a microcanonical ensemble corresponds to an isolated system with constant energy. The total energy of the system does not fluctuate and the system can access only those of its molecular states that correspond to the value of E.

However, a real system is not usually isolated and is typically at some finite temperature or pressure conditions determined by its surroundings. In case of maintaining a fixed temperature, there are several approaches, the simplest one being the velocity rescaling. Under this scheme, whenever the temperature of the system deviates from the desired temperature, the velocities of all the particles in the system are rescaled to maintain that given temperature. However, this technique cannot sample a canonical distribution, and thus, is unphysical. Another approach is to couple the system with an external bath which can control the temperature or pressure, or both. Here comes the concept of NVT and NPT ensembles. Some of the popular thermostats are by Anderson [87], Berendsen [88] and Nosé-Hoover [89, 90]. In this work, we have used Nosé-Hoover thermostat for controlling the temparture. Nosé-Hoover thermostat is an extended Hamiltonian method. Under this scheme, two new degrees of freedom, s and its conjugate momentum p_s are added to the original system and the Hamiltonian of the system gets modified as follows:

serious problem can occur due to atoms reaching to unphysical domains. A very large timestep will lead to atoms jumping long distances before the next update of positions occurs, and thus, two atoms can reach to unphysically close separations. This will lead to a huge rise in potential energy and to a violation of the total energy conservation. Thus, timesteps must be sufficiently small. However, a very small timestep will lead to longer simulation times, which too, is undesirable. Thus, one needs to have a proper compromise between the accuracy and computational times requirements. Usually, for atomic systems, timestep should not be larger than 1 picosecond, which corresponds to the vibrational frequencies of atoms in a crystal lattice.

2.1.3 Boundary conditions

Defining boundary conditions of the simulation cell makes an important part of any MD simulation. For example, when simulating a crystal system, given the limited size of simulation box, a considerable number of atoms will reside on the surface of the box and this will lead to surface effects in the property calculations. The ideal situation would be to take a very big simulation cell to obviate the surface effects. But taking larger cell sizes make computations highly intensive and practically impossible. The way one can simulate an infinite crystal is to make use of the periodic boundary conditions (PBC). In this technique, a simulation box is modeled to be surrounded by periodic images of itself in all the three directions. Thus, even the boundary atoms of the original simulation cell will now find themselves surrounded by atoms from all the sides, and hence, this would mimic as if they are residing in the bulk of the system.

In PBC, if a particle is located at a point (x, y, z) in the simulation box, it is modeled to be present at all the points $(x + n_x L_x, y + n_y L_y, z + n_z L_z)$, where n_x, n_y, n_z are integers and L_x, L_y and L_z are the box lengths along x, y and z axes. If an atom leaves the simulation cell from one side, an identical atom enters back into the box from the opposite surface. Thus, PBC simulates a pseudo infinite medium, and nullifies any surface or edge effects.

Apart from PBC, there are other types of boundary conditions too, such as the

Adding eqns 2.8 and 2.9, we obtain,

$$\mathbf{r}_i(t + \triangle t) = 2\mathbf{r}_i(t) - \mathbf{r}_i(t - \Delta t) + \frac{\triangle t^2}{m_i}\mathbf{F}_i(t) \qquad (2.10)$$

It should be noted, this contains an error of order Δt^4.

Similarly, velocities can be calculated as,

$$\mathbf{v}_i(t) = \frac{\mathbf{r}_i(t + \Delta t) - \mathbf{r}_i(t - \Delta t)}{2\Delta t} \qquad (2.11)$$

Eqn. 2.10 is called the Verlet algorithm [85]. Given a set of initial positions $\mathbf{r}_1(0), ..., \mathbf{r}_N(0)$ and initial velocities $\mathbf{v}_1(0), ..., \mathbf{v}_N(0)$, one can first use eqn. 2.7 to generate $\mathbf{r}_1(1), ..., \mathbf{r}_N(1)$ and then use eqn. 2.10 to generate the full trajectory.

However, there is one drawback with this algorithm, that the velocities are not defined explicitly. This drawback of the Verlet algorithm can be successfully overcome with a slight modification, and the new algorithm is known as the Velocity Verlet algorithm. Under this scheme, the Taylor expansion used in eqn. 2.10 is coupled with the update of velocities as follows:

$$\mathbf{v}_i(t + \triangle t) = \mathbf{v}_i(t) + \frac{1}{2m}\left[\mathbf{F}_i(t) + \mathbf{F_i}(t + \triangle t)\right]\triangle t \qquad (2.12)$$

In the implementation of the Velocity Verlet algorithm, one first obtains the position update using the Verlet algorithm (Eqn. 2.10), then from these positions, new forces can be calculated, which then can be used in eqn. 2.12 to compute the new velocities. It can be easily checked that the Velocity Verlet algorithm generates identical trajectories as generated by the original Verlet algorithm [86]. Since velocities and positions can be simultaneously obtained at every timestep, many physical quantities which depend separately on positions and momentum (for example, kinetic energy and potential energy) can also be calculated together.

The timestep of an integration algorithm, i.e, Δt is an important factor which needs to be chosen carefully. A large timestep will obviously yield higher errors in the integration steps (For example, Verlet algorithm has an error of $O(\Delta t^4)$. But, a

sampling of velocities follows the constraint as:

$$\mathbf{V}_{COM} = \frac{\sum_i m_i \mathbf{v}_i}{\sum_i m_i} = 0 \tag{2.6}$$

2.1.2 The integration algorithms

The eqn. 2.4 needs to be solved numerically and that requires the use of a numerical integrator i.e, an integration algorithm. A numerical integrator generates the phase-space trajectories at discrete times which are the multiples of a parameter called timestep (Δt). The accuracy of MD simulation crucially depends upon the integration algorithm used to integrate the equations of motion. The Verlet algorithm and its variant the Velocity Verlet algorithm are the most widely used integration algorithms. The reason for their popularity is the relative ease of application, efficient implementation, and good numerical precision. Here, we first discuss the Verlet algorithm and then discuss the Velocity Verlet algorithm.

The Verlet algorithm basically uses Taylor series expansion. Suppose, position of the particle at time t is $\mathbf{r}(t)$, then its subsequent position at time $t + \Delta t$ will be $\mathbf{r}(t + \Delta t)$, which can be Taylor expanded as:

$$\mathbf{r_i}(t + \triangle t) \approx \mathbf{r}_i(t) + \triangle t \dot{\mathbf{r}}_i(t) + \frac{\triangle t^2}{2}\ddot{\mathbf{r}}_i(t) + \frac{\triangle t^3}{3!}\dddot{\mathbf{r}}(t) + O(\Delta t^4) \tag{2.7}$$

where, all the terms higher than the fourth order in Δt have been dropped. Now, since $\dot{\mathbf{r}}_i(t) = \mathbf{v}_i(t)$ and from Newton's second law, $\mathbf{F}_i(t) = m_i\ddot{\mathbf{r}}_i(t)$, we can write eqn. 2.7 as,

$$\mathbf{r}_i(t + \triangle t) \approx \mathbf{r}_i(t) + \triangle t \mathbf{v}_i(t) + \frac{\triangle t^2}{2m_i}\mathbf{F}_i(t) + \frac{\triangle t^3}{3!}\dddot{\mathbf{r}}(t) + O(\Delta t^4) \tag{2.8}$$

Again applying Taylor expansion, but this time, we start with the position value at time $t - \Delta t$:

$$\mathbf{r}_i(t - \triangle t) \approx \mathbf{r}_i(t) - \triangle t \mathbf{v}_i(t) + \frac{\triangle t^2}{2m_i}\mathbf{F}_i(t) - \frac{\triangle t^3}{3!}\dddot{\mathbf{r}}(t) + O(\Delta t^4) \tag{2.9}$$

A basic molecular dynamics simulation involves defining initial conditions of the system, employing integration algorithm, defining the boundary conditions and ensembles, defining interatomic potentials, etc., and finally a calculation of the physical quantities and an analysis of the data. Now we discuss these points in detail.

2.1.1 Defining initial conditions

To solve the classical equations of motion (eqn. 2.1), defining the initial conditions makes a basic requisite. It has two main parts: defining the positions and defining the velocities. If a system is equilibrated at a given temperature, velocity distribution of all the atoms in it follows Maxwell-Boltzmann distribution [82]. The difference comes in the way positions are defined. For example, for a liquid, one can start with random initial coordinates, while restricting only the distances between particles so as to avoid strong repulsive forces. For biological materials or for complex molecular systems, the initial parameters can be obtained from experimental values. Similarly, for crystal systems, the lattice positions in the crystal system obtained from X-ray diffraction data can be used as the initial positions for atoms. In this work, we obtained the structure information from the ICDD diffraction database and the spacegroup symmetry information from the Bilbao Crystallographic Server [83]. The structure is then plotted using VESTA [84], which generates all the atom positions in the unit cell using the space group symmetries.

Once the initial coordinates of the system are defined, the next task is to provide the initial velocities to the system. As noticed earlier, in a system equilibrated at a temperature T, the velocities follow the Maxwell-Boltzmann (MB) distribution:

$$f(v) = (\frac{m}{2\pi k_B T})^{1/2} \exp{-mv^2/2k_B T} \tag{2.5}$$

The velocities from the MB distribution are sampled using Box-Muller sampling [82].

One of the most common constraint for initial velocities is that of the external force being zero. In that case, the center of mass has zero velocity. Hence, the

where,

$$H = \sum_{i=1}^{N} \frac{p_i^2}{2m} + V(\{q_i\}) \tag{2.2}$$

Since classical equations of motion are deterministic, one can know precisely the positions and momenta of all the particles at all the times and hence calculate the physical properties. Statistical mechanics provides the link between classical mechanics and thermodynamics which is basically a phenomenological theory. In MD one actually employs the principles of statistical mechanics to calculate thermodynamical properties straight from the classical trajectories generated by the simulation. Thermodynamical quantities are calculated using ensemble averages. For example, the ensemble average of a physical quantity $a(x)$ is calculated as:

$$< a >= \frac{\int dx a(x) F(x)}{\int dx F(x)} \tag{2.3}$$

where, x is the phase space vector of the system and $F(x)$ is the partition function.

However, MD does not provide ensembles, but it evolves the whole system in time, and one can only calculate the time averages of the physical quantities. It is assumed that these time averages are indeed equal to the ensemble averages, and the assumption which provides this link is known as the ergodic hypothesis. According to the ergodic hypothesis, given an infinite time, a system will be able to visit all the phase space points corresponding to its macrostate and hence, an ensemble average can be replaced by a time average. Thus,

$$\bar{a} = \lim_{\tau \to \infty} \frac{1}{\tau} \int d\tau a(x_\tau) =< a > \tag{2.4}$$

where, τ is the time for which the physical quantity has been measured.

However, ergodic hypothesis cannot be proved and will not hold for the systems with large potential hills. This problem is particularly faced in biological systems such as proteins and polypeptides, where important conformations are often separated by barriers in the space of the backbone dihederal angles or other collective variables in the system [82].

17

vides, is its role as a virtual experiment, where one can simulate extreme conditions such as high temperature, pressure etc., just by changing some control parameters in the simulation.

Some of the earliest MD simulations include the work by Fermi, Pasta and Ulam [80], carried out in the fifties, to explore the degree of ergodicity and energy equipartitioning in a one-dimensional chain of harmonic oscillators. Rahman [81] carried out the first simulations using a realistic potential for a system of argon atoms. Since then, there have been many other important works in this field which lead to an advancement of MD techniques as well as provided substantial insights about the statistical systems as well as about the physical processes in real materials.

MD can be classified into two categories: (1) Classical MD and (2) Ab-initio MD. In classical MD, the potential function is given by an empirical formula and in ab-initio MD one uses quantum mechanical methods to obtain the potential function. The earlier MD simulations were limited in the system-size due to limitations in the computational powers. With the advent of modern high-performance computing, nowadays classical MD can scale up to millions of atoms. However, the limitations of system-size still persist in ab-initio MD as the potential function needs to be evaluated at each timestep by solving the Schrödinger equation which makes it computationally highly intensive. Ab-initio MD can successfully model the breaking and forming of bonds and chemical reactions, but its high demand for computational resources makes it inappropriate for simulating large system sizes - one of the prime requirements for displacement cascade studies. Hence, in this work, we have employed classical MD to simulate displacement cascades in Y-Ti-O systems. In our subsequent discussions, we will drop the word "classical" from classical MD and simply refer it as MD.

For a given system with the Hamiltonian $H(\{p_i\}, \{q_i\})$, MD basically solves the classical equations of motion:

$$\dot{q}_i = \frac{\partial H}{\partial p_i}, \quad \dot{p}_i = -\frac{\partial H}{\partial q_i}; \qquad i = \{1....N\} \tag{2.1}$$

Chapter 2

Theoretical and computational methods

Here we discuss the basics of molecular dynamics, density functional theory, and the ring analysis. We also discuss the various types of rings present in the Y-Ti-O crystal systems.

In this chapter, we discuss the theoretical and computational tools used in this thesis. Since molecular dynamics (MD) [78] is the most extensively used technique in the thesis, a major portion of the chapter deals with the theory and methodology of MD, along with the details relevant for our studies. Further, in the development of interatomic potentials, we generated an extensive set of first principle data using density functional theory (DFT) [79]. Thus a brief introduction to DFT is also made, eliciting out its basic principles. Then we discuss the theory and methodology of ring analysis [14] which has been used to analyze cascades, thus setting up a stage for the connectivity topology analysis discussed in Chapter-5 of this thesis.

2.1   Molecular Dynamics

Molecular dynamics solves the classical equations of motion to study the dynamics of a set of particles interacting with a prescribed potential. It is one of the most appropriate computational techniques to explore the atomic systems, and its capability to provide the statistical as well as dynamical details of a system provides it an edge over other computational techniques. The big advantage MD pro-

with respect to direction.

- O atoms play a bigger role than Y atoms in conducting the heat in the Y_2O_3 system.

- A negligible number of antisites survive after the displacement cascade subsides.

- Although the long-range order may be disturbed during the thermal spike, the short-range order is never lost.

SiC, with $f = -3$, should be resistant to amorphization, as predicted by Hobbs [31]. However, it is found to be amorphized easily at 0.2 dpa irradiation dose [55]. It was proposed [135] that the possible antisite disorder generated within the displacement cascade, causes the Si and C sites to become indistinguishable. Due to this the topology and structural freedom of disordered SiC corresponds to that of the Si structure ($f = 0$). Hence, it is easy to amorphize. In our simulations, we have seen that a large number of antisite defects are produced during the ballistic phase. However in the whole thermal spike regime, the RDF does not show any significant shift in the peak positions, but broadens considerably due to the formation of point defects and antisite defects, which result in changes in the local order, but the peaks recover almost fully during the annealing phase. This is due to the high ionicity of the Y–O bond. The difference between Y_2O_3 and SiC comes from their bonding characteristics, as, while SiC is covalent, Y_2O_3 has a highly ionic character, thus the antisite defects cannot be supported in the structure very easily. Y_2O_3 has a very resilient bonding and this property makes it quite stable against amorphization.

3.6   Summary and conclusions

This chapter basically focussed upon 0.5 keV cascades due to Y and O PKA, and a statistics over 253 crystallographic directions is generated for both the cases. Some higher energy (E_{PKA}= 3 and 5 keV) cascades were also carried out, with Y atom as the PKA to study the effect of PKA energy. The initial temperature of the lattice was kept at 300 K. Some of the important points from this study are as follows:

- In the case of E_{PKA}= 0.5 keV, Y PKA produces about 18% higher number of FPs as compared to O PKA.

- The direction dependence, studied for 0.5 keV, showed that the peak number of defects produced do not show any clear dependence upon the initial PKA direction. However, the surviving number of defects do show a variation

hence resistant to amorphization. As we will see in Chapter-5, the structural degree of freedom (f) for Y_2O_3 is -6.0, indicating that Y_2O_3 is a constrained system and hence, must be resistant to amorphization. Naguib and Kelly [46] proposed the temperature ratio criterion according to which, if $T_c/T_m < 0.3$ (where, T_c is the crystallization temperature and T_m is the melting temperature of the system), the system will remain crystalline. For Y_2O_3, T_c is 800–900 K [131, 132] and $T_m \sim 2700$ K [110]. Thus, the temperature ratio comes around 0.3. On the other hand, according to the bond order criterion, if a system has ionicity < 0.47, it would be amorphizable, while materials with ionicity > 0.59 will be always crystalline [46] . Ionicity for this system can be calculated as $I = 1 - \exp{-((X_Y - X_O)/2)^2}$ where, X_Y and X_O are the electronegativities of Y and O atom respectively [46]. Electronegativities can be found from Pauling's electronegativity scale [133]. For Y and O, $X_Y = 1.22$, $X_O = 3.44$. Thus ionicity for Y_2O_3 comes to be 0.7083, and thus, under this criterion too, Y_2O_3 should be resistant to amorphization. Considering the structural behavior of Y_2O_3 matrix under the displacement cascade regime, the pair distribution plots (Fig. 3.10a) provide a lot of insight into the structure of the matrix under displacement cascade. The RDF plot for the total system has a first peak at 2.3 Å, corresponding to the nearest neighbor Y–O distance. As can be seen from the figures, the shift in the first peak is negligible. Similar behavior is seen in Y_2O_3 under high pressures up to 24 GPa [134]. This shows that the Y–O bonding is rigid and hence the basic short-range forces still persist at the peak of the thermal spike and hence the Y–O correlation is preserved. However, the second and third peaks broaden significantly, indicating more disorder in the O–O and Y–Y distances and a loss of long-range order. For the 0.5 keV cascades, even the long-range order seems to be preserved, but this is due to the fact that the cascade is confined to a significantly smaller volume (~ 8.3 Å) than that taken for the RDF analysis (20 Å radius). Experiments [55] performed on Si-based ceramics have shown that for a fluence of $\sim 10^{16}$ Na^+ ions/cm^2, about two-thirds of the SiC_4 tetrahedra are destroyed. In the EXAFS signal, the nearest neighbor Si–C peak vanishes and a new peak emerges corresponding to the formation of the Si–Si bonds.
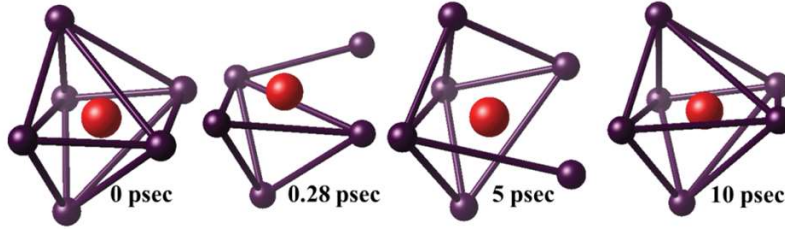
Figure 3.13 – This figure shows the nearest neighborhood of one of the Y ions at different times in the simulation, showing the destruction and the recovery of the YO6 octahedron during the cascade.

$d_i = 0$, but it will be non-zero for different bond lengths. Fig. 3.12 shows the variation in the averaged bond length and the distortion index for all the ions found in the nearest neighborhood of a Y ion, where the averaging has been carried out over all the Y ions in the cascade region of 0.5 keV PKA. Fig. 3.13 shows the nearest neighborhood for one of the Y ions, which shows the destruction and recovery of the YO6 octahedron for the same 0.5 keV cascade. The distortion of octahedra in the displacement cascade increases and becomes a maximum at t_{peak}. By the end of the thermal spike, the octahedra regain the ideal structure. If we consider the total kinetic energy partitioned between the Y and O sublattices, the O sublattice gains energy faster than the Y sublattice and also loses it at a faster rate. This suggests that the octahedra manage to dissipate the extra kinetic energy through the anharmonic vibrational modes, rather than getting destroyed. At about t_{peak}, a decline comes after which MSD attains a constant value. The octahedra in the displacement cascade regime are highly distorted while the ones away from the cascade are virtually undistorted. The constant, non-zero value of MSD at the end of the thermal spike suggests a rearrangement and interchange of the cascade core atoms.

3.5 Discussion

There are different criteria for predicting the resistance to amorphization. The structural freedom criteria predicts amorphizability of systems by calculating the degree of freedom (f) of structuring polytopes of the lattice [28, 130]. A negative value of the structural degree of freedom indicates the system is constrained and

shows the Wendt–Abraham parameter (R_g) for all the three PKA energy cases. A value of R_g greater than 0.14 indicates melting in the system. It can be seen that Wendt–Abraham parameter rises from 0 to its peak value around t_{peak} and then returns to zero at the end of the cascade, indicating recrystallization. R_g reaches the value of 0.14 only for the 5 keV PKA, indicating a highly disordered state at the peak of the thermal spike, while the system virtually remains intact in the case of $E_{PKA} = 0.5$ keV. These plots indicate that Y–O bond is not affected much and hence, the Y–O correlation is not lost, while the next nearest neighbors do get displaced and then come back to their position soon after t_{peak}. This can also be seen from the corresponding mean square displacement (MSD) plots shown in Fig. 3.11 for all the atoms. MSD is calculated in a spherical volume of 30 Å radius. For a 5 keV PKA, the peak value of MSD shows that on an average, all the atoms are displaced by about 1.8 Å, while the atoms lying near the cascade core are displaced on an average by a distance slightly greater than the Y–O interatomic distance (2.3 Å). It is seen that the peak value of MSD reaches just after the t_{peak} and then slightly decreases and settles down to a value of 2.3 Å^2.
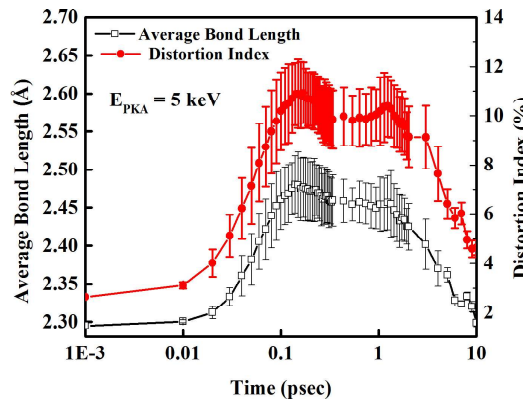
Figure 3.12 – The averaged distortion index and the Y–O bond length of the Y$_2$O$_3$ octahedra as a function of the simulation time.

Now we complement these studies by analysing the geometry of the YO6 polyhedra in the cascade region. For any polytope, one can define the distortion index [129] as, $d_i = \frac{1}{n} \sum_1^n \frac{|l_i - l_{avg}|}{l_{avg}}$, where, n is the number of the atoms in the neighborhood of the central atom, d_i the distortion index, l_i the individual bond length, and l_{avg} the average bond length in the regular polytope. If all the bond lengths are equal,

around the initial position of the PKA. The RDF plots are shown in Fig. 3.10a for the three energies. It shows the nearest neighbor Y–O peak at 2.3 Å, the O–O peak at 2.9 Å and the Y–Y peak at 3.5 Å. As can be seen from the RDF plots, the crystal gets disordered at the thermal spike and then almost recovers its initial state at the end of the cascade. For 0.5 keV, the crystal remains practically unaltered during the whole cascade as the cascade core region is quite small and the crystal is not disturbed much outside the cascade volume.
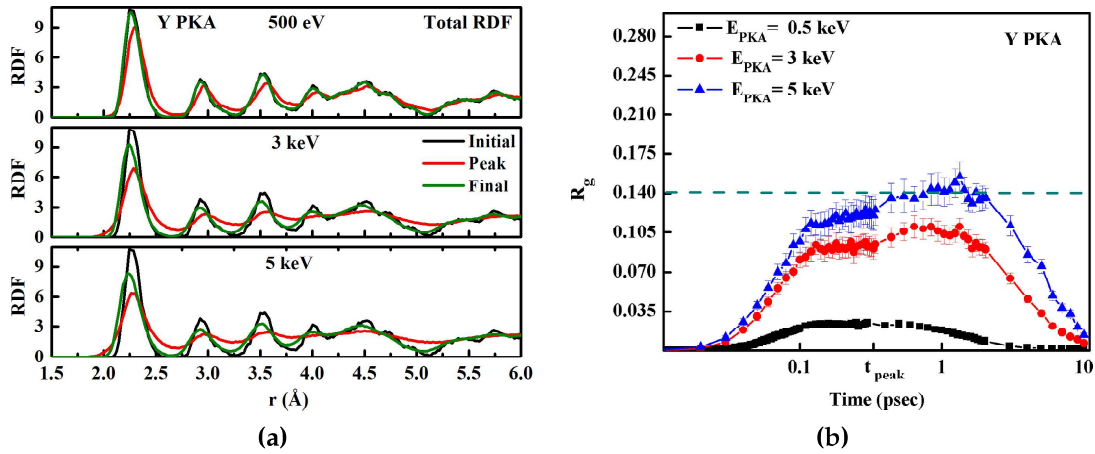
Figure 3.10 – (3.10a) Pair correlation function plot for 0.5, 3 and 5 keV PKA, in a spherical region of radius 20 Å around the PKA; (3.10b) Wendt–Abraham parameter (R_g) calculated from the ratio of the first minimum to the first maximum in the pair correlation function.
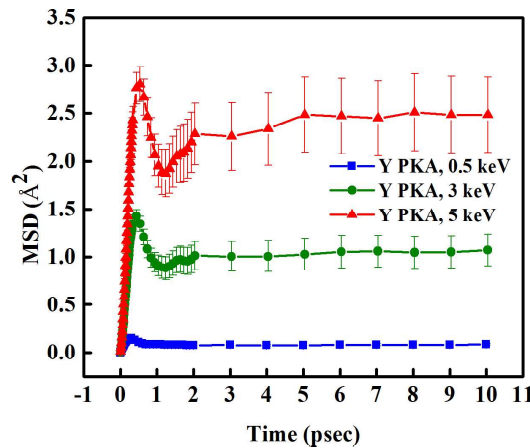
Figure 3.11 – MSD vs time plots for all the PKA energies.

RDF gives a qualitative picture of the disorder. Wendt-Abraham parameter (R_g) defined as the ratio of the first minimum and the first maximum of the RDF of a system [128] can quantify the information obtained from RDF. Fig. 3.10b
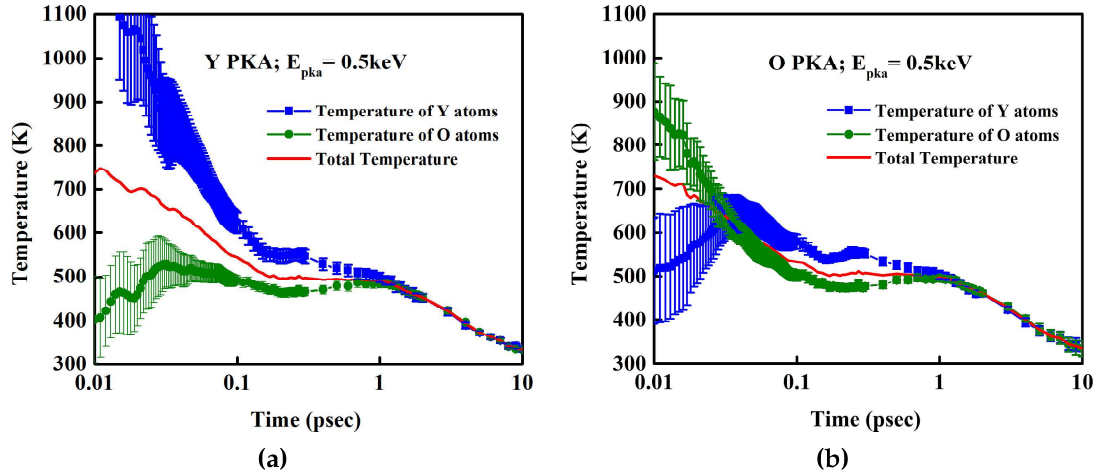
Figure 3.9 – Temperature distribution of Y and O atoms in Y_2O_3: (3.9a) Y PKA (3.9b) O PKA.

the individual Y and O sublattices. Fig. 3.9 shows the temperature distribution of Y and O atoms. If the sublattice is of the same atomic type as that of the PKA (for example, Y sublattice, when Y atom is the PKA), then initially, that sublattice is having a higher temperature than the other sublattice. This is simply because of the way we calculate temperature from the average kinetic energy. Although in the initial period, temperatures of the Y and O sublattices are different, but after about $\sim$ 1 psec, it is equal in both the lattices. It should be noticed that in the period before 1 psec, regardless of the type of PKA species used to generate the cascade, oxygen sublattice loses its heat energy at a higher rate than Y sublattice. This point is emphasized by Fig. 3.9b, which shows the case of O PKA. It can be seen, although the temperature of O sublattice was initially higher than the Y sublattice, it still lost its energy quickly, and became colder than Y sublattice for a short time interval before 1 ps, after which both the lattices equilibrate to the same temperature. Thus, it indicates that in both the ballistic movement phase and post t_{peak} during the cascade, it is the O ions that predominantly help in redistribution of the energy due to the larger probability of their collision with other O ions.

3.4.4   Local structure in the cascade

Now we study the local structure in the cascade region using various analyses. The radial distribution function (RDF) is calculated in a sphere of radius 20 Å

3.4.3 Temperature distribution in the cascade region

During a displacement cascade process, not only a large number of point defects are produced, but the temperature of the cascade region also rises drastically. However, as the time proceeds, this high temperature in the cascade starts decaying, as the heat flows out to the outward regions. Fig. 3.8 shows the variation of temperature with time for Y and O PKAs (E_{PKA} = 0.5 keV) in different concentric spherical shells of increasing radius around the initial position of the PKA. Here, each shell is of 5 Å thickness, and the first shell has a radius of 5 Å, while the last shell has 35 Å radius. The plots show that the regions farthest from the PKA practically remain unaffected and retain their original temperature. As can be seen, for all the PKA energies, the temperature increases to a very high value, but then starts decaying and by the end of the simulation time, decays to the initial equilibration temperature (300 K) of the lattice. After t_{peak}, once the defect generation has stopped, the system does not find enough time to exhibit melting outside a very small region in the cascade core and the other regions become highly disordered. The energy that has been deposited in the crystal subsequently gets dissipated through anharmonic phonon coupling that is quite strong at high temperatures.
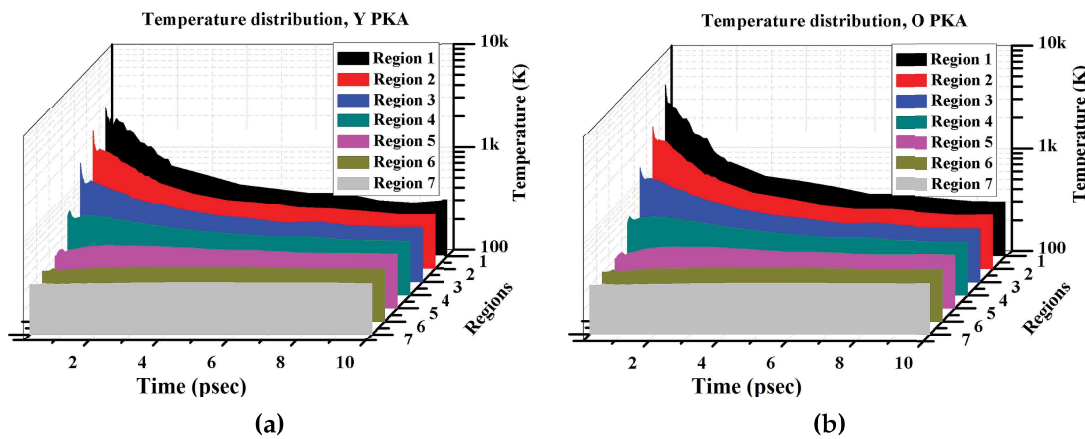
Figure 3.8 – Temperature variation in spherical shells around the PKA of energy = 0.5 keV. (a) Y PKA; (b) O PKA.

Now we study the role played by Y and O atoms in the distribution of heat energy during displacement cascades. For this, we calculate the temperatures of

Fig. 3.6 that for 0.5 keV PKA energy, only a negligible number of antisite defects are produced, while for the higher energy PKAs, the number of antisites also increases. However, by the end of the cascade, only a negligible number of antisites survive. This is because of the high formation energy of the antisite defects in Y_2O_3 matrix, which is 6.03 eV for charge neutral Y antisite and 18.37 eV for charge neutral O antisite [127]. O antisites also show a similar distribution as Y antisites.
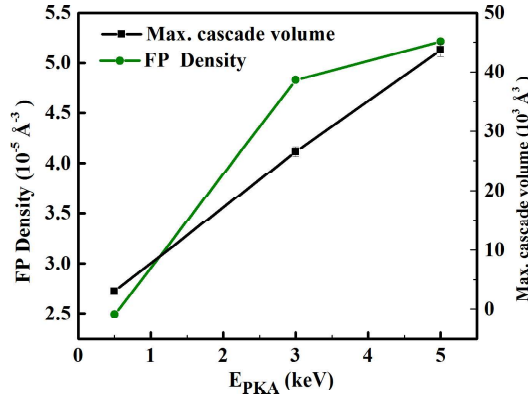
Figure 3.7 – Variation of the cascade volume and the number density of Frenkel pairs with respect to PKA energy.

Now we calculate the cascade volume and the FP number density at t_{peak} for the different PKA energies. The cascade volume is calculated by finding the volume of an equivalent sphere of radius equal to the root mean square (RMS) distance of all the created vacancies from the centroid of the FPs at t_{peak}. The average RMS radius is a better criterion as compared to the Delaunay triangulation technique for finding the cascade volume as it is not affected severely if a small number of atoms are displaced by a large amount during the cascade. The RMS radius is found to be 8.94 ± 0.4 Å and 8.65 ± 0.3 Å for Y and O PKA cascades at 0.5 keV and 18.48 ± 0.2 Å and 21.8 ± 0.2 Å for 3 and 5 keV Y PKA cascades respectively. Fig. 3.7 shows that the cascade volume increases linearly with the PKA energy. However, the FP number density in the cascade volume does not show a linear behavior, with an apparent saturation in the density is seen beyond 3 keV energy. This shows that the cascade is sparse at lower energies while it gets denser as the PKA energy increases. This may be a reason for $\kappa > 0.8$, for 0.5 keV energy cascade.

3.4.2   PKA energy effect

Here we study the effect of PKA energy on the cascade characteristics. These simulations are carried out only for Y PKA. Fig. 3.5 shows the net surviving number of Frenkel pairs for all the energies of the PKAs. It shows that the actual number of surviving defects is equal to that predicted by Norgett–Robinson–Torrens (NRT) formula [126]. The displacement efficiency (κ) is calculated using the formula $N_{FP} = \kappa E_{PKA}/2E_d$. Comparing this result with Calder and Bacon's result for Fe [123], we see, that the displacement efficiency for Y_2O_3 is greater than that for Fe. Thus, in Y_2O_3 a larger number of defects survive at the end of the cascade, as compared to Fe.
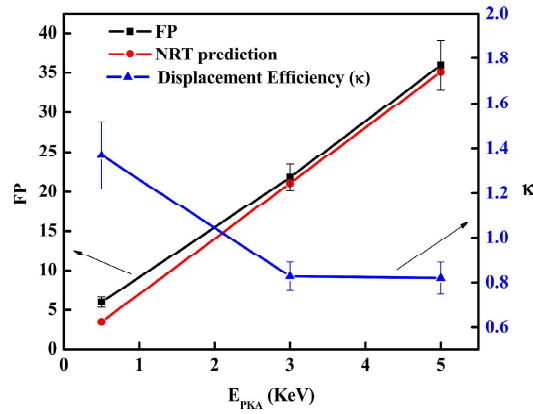
Figure 3.5 – The surviving FPs for Y PKA, compared to the NRT model and the displacement efficiency (κ) calculated using $N_{FP} = \kappa E_{PKA}/2E_d$. For NRT, $\kappa = 0.8$.
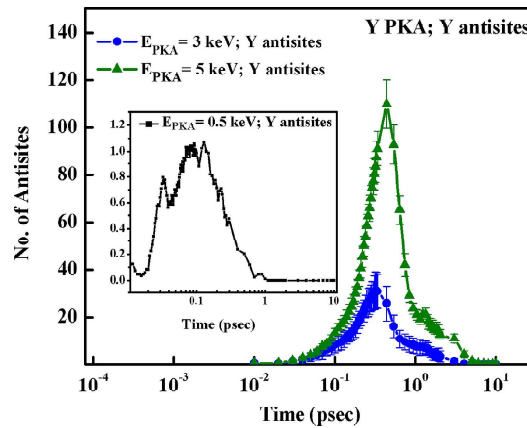
Figure 3.6 – The antisite defects generated for Y PKA at different energies.

In a multicomponent system like yttria, the radiation cascade can also lead to antisite defects that constitute to a local chemical disorder. It can be observed from

This result clearly shows that the Y PKA loses its energy at a rate smaller than that for O PKA and hence, the defect peak also comes little later (Fig. 3.2c). On an average, both the O and Y PKA are displaced by similar amount of 3.5 Å till the time the energy of the PKA falls below the displacement energy E_d, which is 57 eV [124] for both the Y and O atoms in Y_2O_3, as computed from the transmission electron microscopy data. This distance is of the order of the Y–Y and O–O distances in Y_2O_3. There are 6 Y and 6 O ions in the Y ion neighborhood, while there are 4 Y and 9 O ions in the O ion neighborhood within this distance. Both the PKAs keep on moving fast due to secondary collisions thereafter till t_{peak}, and move an average distance of 7.5 Å for Y and 13.5 Å for O PKA. The fast movement of the atoms comes to a stop at $\sim$ 2 ps, after which the system thermalizes to the simulation temperature. By this time the PKAs cover an average distance of 16.5 Å for Y and 23 Å for O PKA. As the Y PKA is surrounded by 6 O ions, it is able to transfer energy at the start of the cascade to a large number of O ions. The immediate neighborhood of an O PKA comprises of 4 heavy Y atoms, to which a fraction of the energy of the PKA would get transferred. Compared to this the O PKA can transfer energy much more efficiently to other O ions in its extended neighborhood. In fact, the entire energy of the O PKA can be transferred to another O atom in a single head-on collision, whereas at most a fraction 0.517 of the O PKA energy can be transferred in a head-on collision with a Y atom. Hence, the O PKA loses its energy faster as compared to the Y PKA on an average. The cumulative effect of this asymmetry gets built up as the cascade progresses. At higher energies of 3 and 5 keV, we see from Fig. 3.4 that the Y PKA energy becomes lesser than E_d at practically the same time. This is due to the fact that the PKA travels almost 6.4 Å for 3 keV and 7 Å for 5 keV during this time and the number of collisions that it undergoes is same for both the energies. The total distance a Y PKA travels increases with the PKA energy to 28 Å for 3 keV and 32 Å for 5 keV. O PKAs travel a lot farther than Y PKAs ($>$ 42 Å for 5 keV PKA).
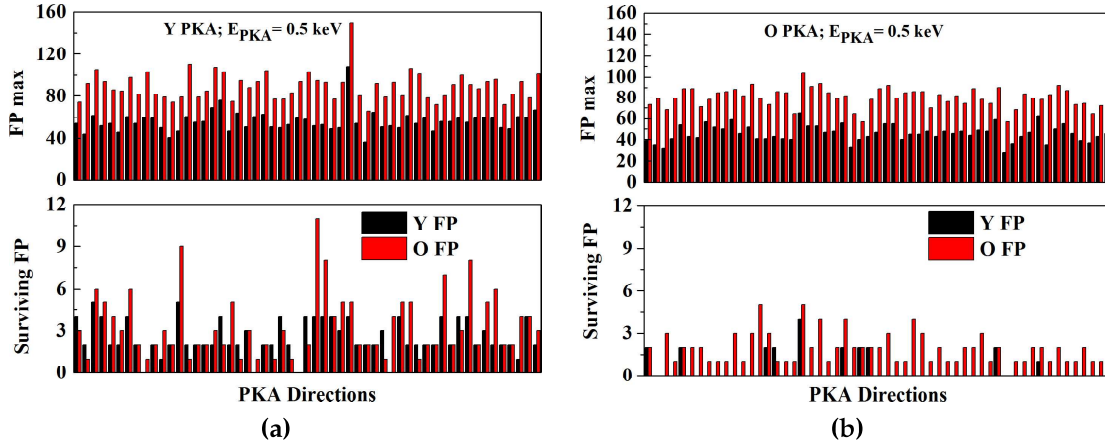
Figure 3.3 – The peak number of FPs (FP$_{max}$) and surviving number of FPs for different PKA directions: (3.3a) Y PKA; (3.3b) O PKA. The points on the *x*-axis in these plots refer to various directions such as <100>, <110>…, etc., taken in the simulations.

the simple binary collision approximation [5]. Assuming the collisions to be perfectly elastic and treating the atoms as equivalent hard spheres, the average kinetic energy transfer is given by $< T_i >= \frac{\gamma E_i}{2}$, where, E_i is the energy of the incident particle, T the transferred energy and $\gamma = 4m_1 m_2/(m_1 + m_2)^2$. Energy transfer is maximum when the two masses m_1 and m_2 are equal. In view of the stoichiometry of Y$_2$O$_3$, the probability of collision of both the Y and O PKAs with another Y atom is lesser than that for collision with O atom, leading to a little inefficient energy transfer for Y PKA as compared to O PKA. This can be seen from Fig. 3.4, where the energy variation of the PKA as a function of time has been plotted for both Y and O PKA.
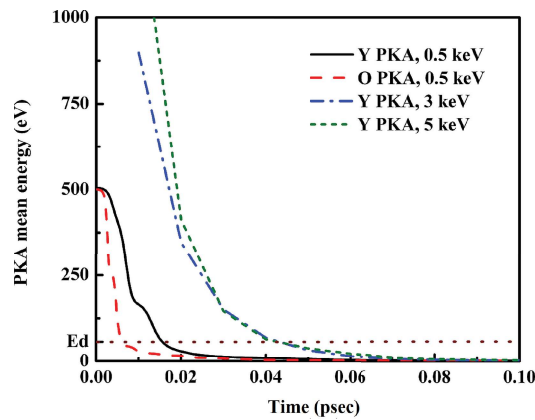
Figure 3.4 – Mean PKA energy plotted as a function of simulation time for 0.5, 3 and 5 keV PKAs.
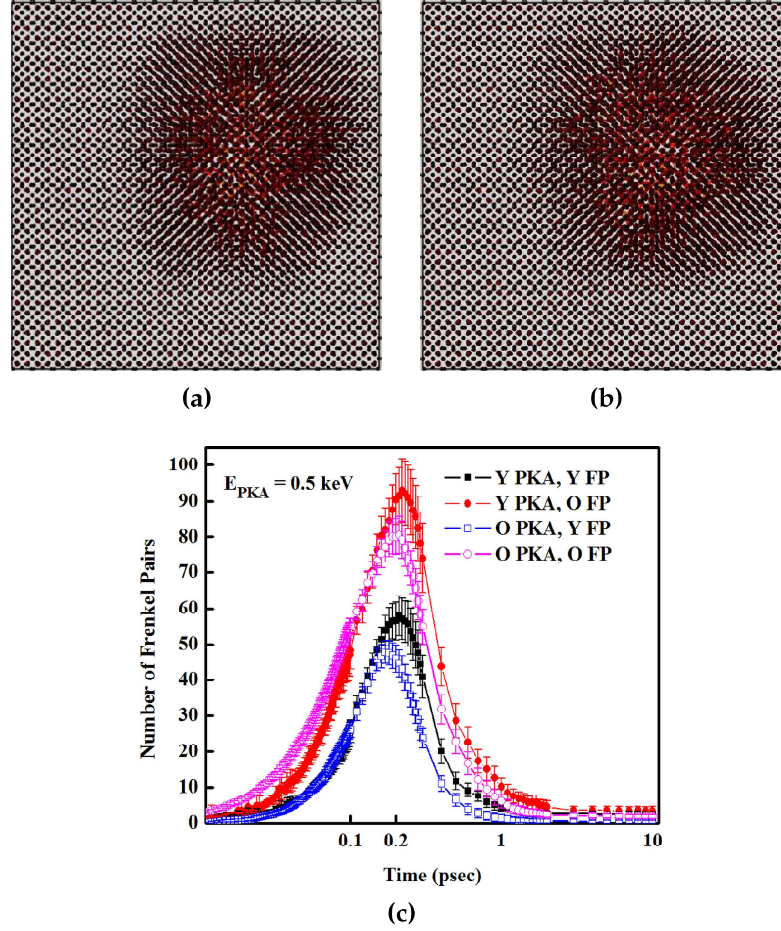
Figure 3.2 – (3.2a and 3.2b) Show two of the cascades generated at t_{peak}, for the 0.5 keV Y PKA started in <410> and <631> directions respectively. The atoms with speed above that corresponding to the average speed at room temperature are colored red and others are colored black; (3.2c) Y and O Frenkel pairs (FP) vs time for E_{PKA} = 0.5 keV. The figures in (3.2a and 3.2b) were generated using OVITO [125].

As seen in Fig. 3.3, the maximum number of Frenkel pairs generated by any PKA does not significantly depend on the PKA direction. The number of surviving Frenkel defects does show a distribution, however, no definite correlation between the direction of PKA and the number of Frenkel pairs generated by it is discernible. The isotropic nature of the displacement cascade can be due to the inherent nature of the Y_2O_3 crystal which contains large interstitial volumes and thus the number density of the atoms in almost all the planes apart from the <111> plane is similar.

We can also see from Fig. 3.2c that the time (t_{peak}) to reach the maximum number of defects is little higher for the Y PKA in comparison to O PKA (0.22 ps for Y PKA and 0.18 ps for O PKA). The reason for this observation can be explained from

51

the atoms move comparatively slowly and the generated defects get annealed out. Variable timesteps of $2 \times 10^{-6}, 10^{-5}, 10^{-4}$ and 10^{-3} ps are chosen at different stages from the start of the cascade, when the atoms are moving very fast, to the annealing phase, where the atoms are relatively slow moving, for a total simulation time of 10.3 ps. Periodic boundary conditions are applied in all the directions. For integrating the equations of motion, Velocity Verlet algorithm [86] is used. The defect analysis is done by using the equivalent sphere analysis [30, 123] by comparing the position of atoms with that in the original lattice just before the start of the cascade. The generation and annihilation of the defects is analyzed for all the time steps and the interstitials and vacancies of Y and O atoms are counted separately.

3.4 Results

3.4.1 Distribution of point defects

A displacement cascade process produces a substantial number of point defects such as Frenkel pairs, antisites and leads to a disorder in a localized region. Here we analyze the number of Frenkel pairs (FP) produced in the system. First, we start with the study of the effect of PKA species (Y or O atom), which has been carried out for $E_{PKA} = 0.5$ keV case. As can be seen from Fig. 3.2c, at the time (t_{peak}) when the number of defects reaches its maximum value in the cascade, the number of FP generated by a Y PKA is $\sim 18\%$ more than the number of FP produced by O PKA of the same energy. This result differs from the study on Er_2O_3 by Kittiratanawasin *et. al* [71], where they report that for Er_2O_3, the low energy cascades of 0.4 keV induce the similar number of defects for both the Er and O PKA. The number of oxygen defects is always seen to be greater than the number of yttrium defects (Fig. 3.2c). The reason for this is the stoichiometry of the yttria matrix. This tendency for more number of oxygen defects was also seen in the studies on Er_2O_3 [50]. But in that case, apart from the stoichiometry, the threshold displacement energy (lesser E_d for O than that for Er) is also one of the reasons. However, as seen from [124], the Y and O atoms have about the same threshold displacement energy of 57 eV in Y_2O_3.

the MP of yttria quite closely. The functional form of the interatomic potential is as follows:

$$\phi(r_{ij}) = A_{ij} \exp(-B_{ij} r_{ij}) + q_i q_j e^2 / r_{ij} \tag{3.1}$$

Here, r_{ij} is the distance between atoms i and j, q_i is the ionic charge of the ith atom, e is the electronic charge, and A_{ij} and B_{ij} are parameters. The potential parameters are as follows: $A_{YY} = 239350.4$ eV, $B_{YY} = 4.3048$ Å^{-1}, $A_{YO} = 143417.5$ eV, $B_{YO} = 5.7928$ Å^{-1}, $A_{OO} = 450833.3$ eV, $B_{OO} = 5.3195$ Å^{-1}, $q_Y = +1.8$ and $q_O = -1.2$.

3.3.1 Simulating radiation damage using MD

MD simulations are performed using LAMMPS [13]. We use a cubic simulation box to model the cascade evolution. The whole cascade is contained fully and remains well inside the simulation box and whenever it touches the simulation boundaries, the run is aborted. The crystal is equilibrated at an initial temperature of 300 K. To simulate the heat bath, Nosè-Hoover thermostat [89, 90] is used. The simulation box is divided into exterior and interior regions. The exterior region is a shell comprising of the atomic layers contained within half a lattice parameter along all the faces of the simulation box, while the interior region consists of all the other atoms. Before the initiation of displacement cascade, the whole system is equilibrated for a total of 50 ps. In the first 30 ps of the equilibration process, constant NPT conditions are applied, after which the exterior region is evolved for the next 20 ps keeping NVT constant with T = 300 K, while the interior region is allowed to equilibrate under constant NVE conditions. After the equilibration, constant NVE conditions are continued in the interior region and a cascade is initiated by imparting the required energy for the PKA, either Y or O atom, at the center of the simulation box. Since in MD simulations, the optimum choice of the timestep decides the accuracy of the simulation and computational time efficiency, we take variable timestep approach considering the different time scales of the processes involved in cascades such as the initial ballistic phase, when the atoms move very fast till the peak defect production, and after that, the annealing period when

to Y_a octahedra, while Y_a octahedra are connected to both Y_b and Y_a octahedra. Each vertex is shared by three edge-connected and one corner shared YO6 unit.

3.3 Simulation details

To simulate the displacement cascades we took a $9 \times 9 \times 9$ cell of Y_2O_3. PKA energies considered in this chapter are 0.5, 3 and 5 keV, however, maximum statistics were generated for 0.5 keV case, and the study of displacement cascades due to O PKA is done only for the 0.5 keV case. Since Y_2O_3 is an ionic solid, it has long-range Coulomb interactions between its atoms, that need to be calculated in every MD step. This involves Ewald summation [86] which makes the computations very intensive. Thus we limited the runs to lower energy simulations as smaller simulation cells are adequate for them, and they could be performed with the available computational facilities at the time of this work. We will discuss the higher energetic simulations in Y_2O_3 crystal in chapter-5, where the cascade properties in Y_2O_3, Y_2TiO_5 and $Y_2Ti_2O_7$ will be compared.

To study the effect of initial direction of PKA on the cascade characteristics, we take 55 different crystallographic directions for the initiation of the PKA. These 55 crystallographic directions correspond to independent directions in a set of 253 directions after accounting for the multiplicities of the underlying bcc lattice. Further, in the case of 0.5 keV PKA, both Y and O atoms are chosen as PKA, to understand the effect of PKA species on cascade. The PKA energies chosen for Y and O atoms are taken for comparison of our data with the older published works, as many of the studies use the PKA energies in this range.

MD simulations require appropriate interatomic potentials. Pair potentials of the Pauling type [121, 122] are available for yttria, however, these potentials do not correctly reproduce the melting point (MP) of yttria [17]. Since the temperature can exceed the melting point of the material during displacement cascades, these potentials are unsuitable for carrying out radiation damage cascade simulations. In these studies, we have used the potential developed by Belonoshko *et. al* [17] which has a Born-Mayer term [18] and a Coulomb term. This potential estimates

atom occupies the body center of a cube, the corners of which are occupied by O atoms [119, 120]. A quarter of the O atoms are missing in this ideal structure. The arrangement of the vacancies is regular and they occupy either the face diagonal, or the body diagonal positions. As shown in Fig. 3.1b, Y_a unit on the lower left has two O vacancies on the face diagonal. Y_b unit on the upper right has two O vacancies on the body diagonal. For both the sites the coordination number is 6, but whilst Y_b atoms form the Y_bO6 octahedron with equal bond lengths, the Y_aO6 octahedron is highly distorted in the real structure with 3 different bond length pairs, as shown in Fig. 3.1c. Thus, the bixbyite crystal structure can be viewed as comprising of 32 Y ions, 48 O ions and 16 O vacancy positions.

(a)   (b)

(c)
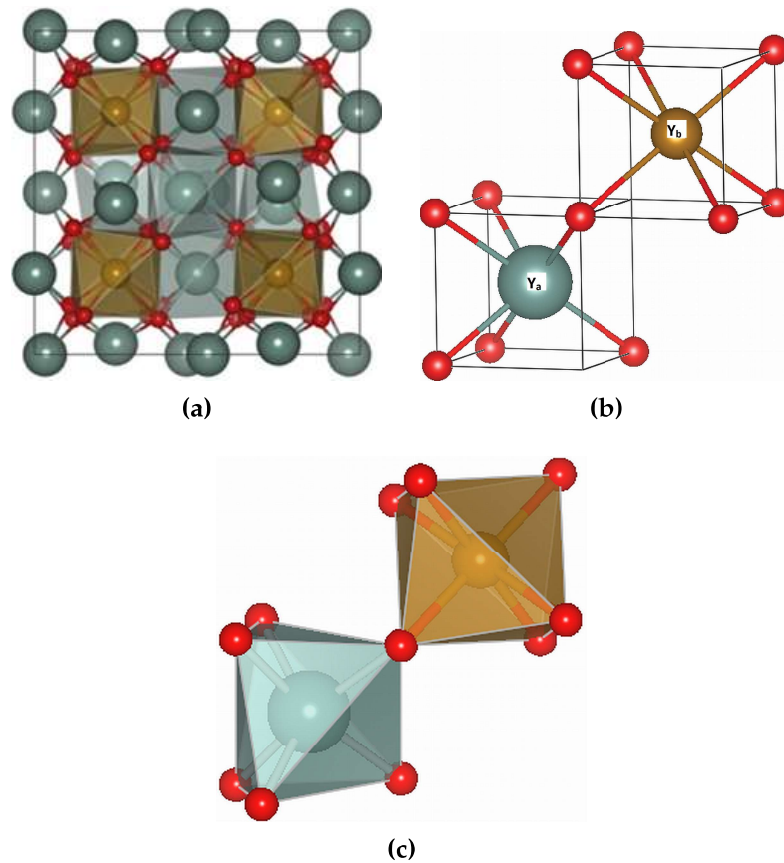
Figure 3.1 – (3.1a) Crystal structure of Y_2O_3, showing the interconnected YO6 units; (3.1b and 3.1c) The local environment of the two inequivalent Y ions in Y_2O_3 structure: (3.1b) ideal representation and (3.1c) after atomic relaxation. Green balls represent Y_a, copper balls Y_b and red balls O atoms.

Alternatively, the unit cell can be viewed as a network of interconnected octahedra (Fig. 3.1a), where each Y atom is surrounded by 6 O atoms. Each octahedron is connected via six edges to other YO6 octahedra. Y_b octahedra are connected only

As discussed earlier, Molecular dynamics (MD) is an appropriate tool to study the mechanism of displacement cascades [32]. Work on MD studies of displacement cascade on other bixbyite structures such as Er_2O_3 has been reported [50, 71]. There have been studies of displacement cascades in Y_2O_3 embedded in α-Fe matrix [70] which show that Y_2O_3 provides radiation stability to the host Fe matrix by releasing the absorbed energy from primary knock-on atom (PKA) at larger time scales through atomic vibrations and hence helps in reducing the number of point defects generated in the host matrix. However, there is not enough information about how the displacement cascade affects the bulk Y_2O_3 properties. The current study thus focuses on the structural and defect production aspects of the displacement cascades in Y_2O_3 single crystal. We study the production and annihilation of point defects, the influence of the mass of PKA on displacement cascades, the effect of initial direction of the PKA on the cascade characteristics, the variation of the temperature and other structural aspects during the course of displacement cascade.

This chapter is organized as follows: We first discuss the structure of Y_2O_3 in section 3.2. Then we discuss the particulars of the simulations in section 3.3, which is followed by a presentation of the results and discussion in sections 3.4 and 3.5. Section 3.6 summarises the main results of this study.

3.2   Structure of Y_2O_3

Y_2O_3 has a bixbyite structure [117] which is a focus of active research due to its high tolerance against radiation damage and its resistance to crystalline to amorphous transformation. Bixbyite Y_2O_3 is basically a bcc crystal structure ($Ia\bar{3}$), containing 80 atoms per unit cell (32 Y and 48 O atoms) [118], with a lattice constant of 10.6 Å, which is shown in Fig. 3.1a. It has two symmetrically inequivalent cation sites, Y_a (green balls) at Wyckoff positions $24d$ $(x, 0, 1/4)$ and Y_b (copper balls) at Wyckoff positions $8a$ $(1/4, 1/4, 1/4)$. Oxygen (red balls) atoms are placed at the Wyckoff positions $48e$ (x, y, z). The local environments of the two Y atoms are different as shown in Fig. 3.1b. One way to look into this structure is, that each Y

Chapter 3

Displacement cascades studies in yttria crystal

In this chapter, we discuss molecular dynamics simulations of displacement cascades in yttria crystal. Cascades are generated by different PKA species as well as for different initial directions of the PKA. Even though the crystal is seen to be in a highly disordered state in the cascade volume, the correlation between the Y and O atoms is not completely lost.

3.1 Introduction

In this chapter, we present the results of our studies of displacement cascades in bulk yttria (Y_2O_3) crystal. Y_2O_3 is one of the important ingredients of oxide dispersion strengthened (ODS) steels and it provides them mechanical strength along with the radiation resistance. It has a high melting point of 2700 K [110], good crystallographic stability up to 2600 K [111, 112], high mechanical strength, high thermal conductivity (33 W m^{-1} K^{-1}), wide band gap (6 eV), relatively high dielectric constant ($\sim$15), and high static dielectric constant (between 2 and 3) [113–115]. These properties make it an appropriate choice for some very different fields too, such as for optoelectronic applications and for protective coatings in severely reactive environments [116]. Further, its radiation resistance properties are highly useful for the semiconductor industry too.

systems of Y_2TiO_5 and $Y_2Ti_2O_7$. An extensive set of first principle calculations data was generated for the fitting of the potential parameters and the required checks were carried out to ensure the reliability of the potentials. Some of the important points of this chapter are as follows:

- The new potentials are of the rigid-ion type and lack shell components, which makes them appropriate for MD simulations of large system sizes, up to 1 million atoms.

- The repulsive part of the Buckingham potential has been modeled with good care, and thus the potentials are expected to be appropriate for simulating processes where atoms come very close to each other as in energetic situations.

- The potentials reproduce the melting temperature of the systems quite nicely, which indicates these potentials are well suited for studying thermal properties.

- Cation antisite pair formation energy is smaller than most of the other defect pair formation energies. In particular, for $Y_2Ti_2O_7$, it is quite small, indicating the ease for cation antisite formation.

- The potentials were further used to probe different properties of both the systems such as the bond distances, lattice parameters, elastic constants, coefficient of thermal expansion etc., and are able to reproduce the experimental/ *ab initio* values of the physical properties fairly well.

(a)

(b)

(c)
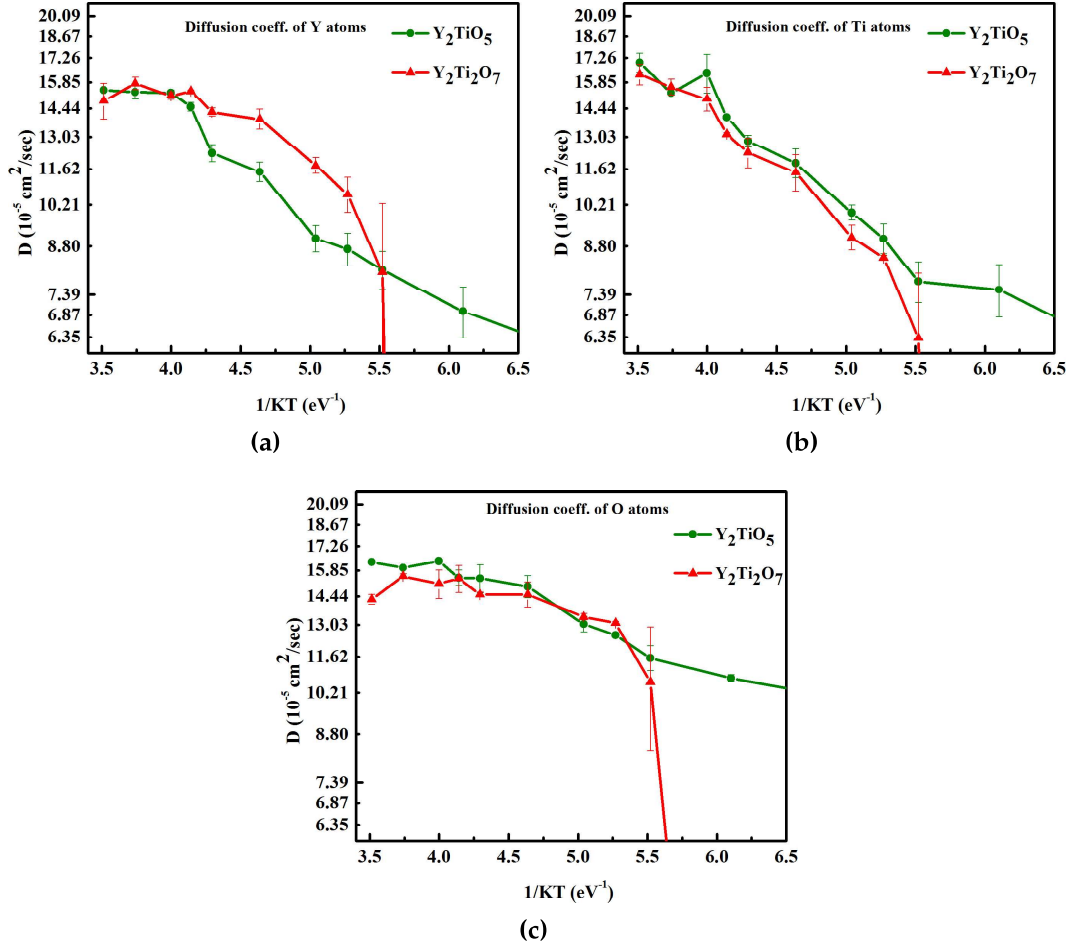
Figure 4.9 – A comparison of diffusion coefficients of individual atomic species in Y_2TiO_5 and $Y_2Ti_2O_7$. (4.9a) Diffusion coefficient of Y atoms, D(Y) vs temperature; (4.9b) D(Ti) vs temperature; (4.9c) D(O) vs temperature.

easier to jump to it, as compared to a reverse situation in which Ti atoms jumps to a vacant lattice site of Y. A comparison of diffusion coefficients for different atomic species is shown in Fig. 4.9. It shows that after the MP for both the systems is reached, Y atoms have a higher diffusion coefficient in $Y_2Ti_2O_7$, as compared to that in Y_2TiO_5. However, after MP, the diffusion coefficient of Ti does not differ in the two systems, as seen from Fig. 4.9b. A similar behavior is seen in the case of O atoms too, as shown in Fig. 4.9c.

4.5 Summary and conclusions

In this chapter, we discussed the development of new pair-wise interatomic potentials based on combined Coulomb and Buckingham potentials for the crystal
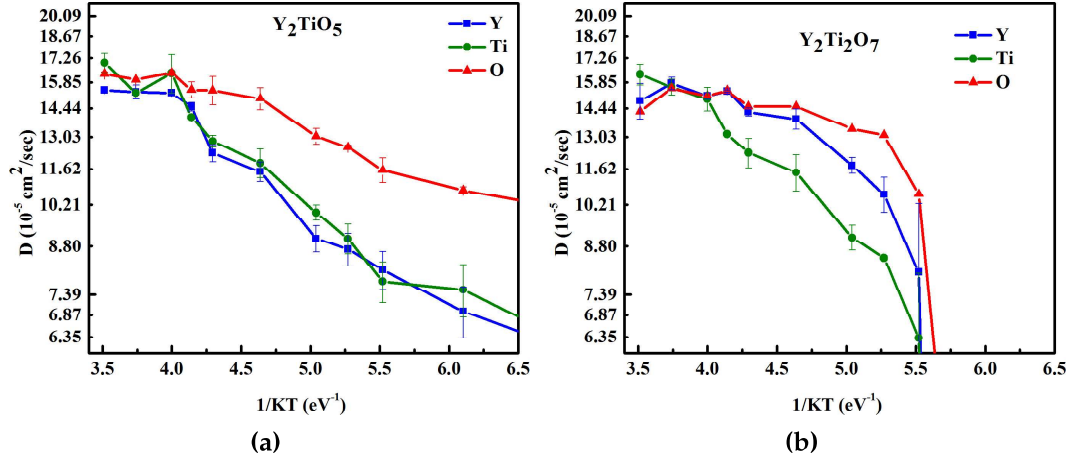
Figure 4.8 – Diffusion coefficient of Y, Ti and O atoms in (4.8a) Y_2TiO_5; (4.8b) $Y_2Ti_2O_7$.

and O atoms in both Y_2TiO_5 and $Y_2Ti_2O_7$ are shown in Fig. 4.8. In both the systems, the diffusion coefficient remains almost zero for temperatures lesser than the respective MP, indicating the systems are solid at these temperatures. It starts increasing abruptly at ~ 1750 K (1/KT= 6.625 eV^{-1}) for Y_2TiO_5 and at about ~ 2300 K (1/KT= 5.04 eV^{-1}) for $Y_2Ti_2O_7$ indicating a high diffusion in the systems near their respective melting points. It is to be noticed, that in Y_2TiO_5, in contrast to $Y_2Ti_2O_7$, oxygen atoms have a significant diffusion coefficient compared to other atomic species well before the melting point is reached.

Y and Ti atoms have almost the same diffusion coefficient in Y_2TiO_5 while Y has a higher diffusion coefficient than Ti in $Y_2Ti_2O_7$. Y atom is heavier than Ti atom, and given the same kinetic energy for both the atoms at a given temperature, Y atoms have a lower velocity than Ti atoms and thus must have a smaller mean square displacement (MSD), if the systems are just assumed to be in a continuum. However, the higher diffusion coefficient of Y atoms than Ti atoms, in $Y_2Ti_2O_7$ indicates that the process involving a Y atom jumping to its neighboring site is more favourable than that for Ti atoms. DFT calculations by Xiao *et. al* [76] show that the antisite formation energy for Y atom occupying Ti lattice site is 1.56 eV, which is smaller than the formation energy of Ti antisite at Y lattice site (4.45 eV). This may be a reason for Y having a higher diffusion coefficient, as compared to Ti atoms in $Y_2Ti_2O_7$, because, for a given vacant lattice site of Ti, a Y atom will find it

Y$_2$TiO$_5$				
	MD *(GPa)*	**GULP** *(GPa)*	**DFT** *(GPa)* [145]	**Expt.** *(GPa)* [150]
C11	184.3	182.2	188.7	–
C12	70.3	72.9	85.6	–
C13	66.4	64.4	90.5	–
C22	252.8	234.6	212.5	–
C23	98.9	101.4	118.6	–
C33	193.3	191.8	232.0	–
C44	97.1	96.7	91.4	–
C55	46.4	30.6	55.5	–
C66	48.9	48.6	67.0	–
B$_{Voigt}$	122.4	120.7	135.8	–
G$_{Voigt}$	64.8	51.6	65.3	–
E$_{Voigt}$	165.3	154.1	168.9	–
Y$_2$Ti$_2$O$_7$				
C11	245.5	239.4	325.2	329.4
C12	85.9	82.8	111.7	91.4
C44	80.7	80.6	73.2	97.2
B$_{Voigt}$	139.1	134.9	182.9	170.7
G$_{Voigt}$	80.3	79.6	86.6	105.9
E$_{Voigt}$	202.1	198.9	224.4	263.3

Table 4.4 – Elastic constants of Y$_2$TiO$_5$ and Y$_2$Ti$_2$O$_7$ calculated from molecular dynamics, lattice dynamics (GULP) and DFT calculations and compared with experimental data ([150]) in the case of Y$_2$Ti$_2$O$_7$. *Cij*: elastic constants, B$_{Voigt}$: Bulk modulus Voigt average, G$_{Voigt}$: Shear modulus Voigt average, E$_{Voigt}$: Young's modulus Voigt average.

MD calculated *C12* and *C44* are near to the experimental values, *C11* differs from both the experimental and DFT calculated values by ∼25%. There is a discrepancy seen in both the *C12* and *C44* between the experimental and DFT calculated values too. This results in the large difference seen in the GULP, MD and the DFT calculated bulk modulus of the Y$_2$Ti$_2$O$_7$ crystal. There is no data on experimental measurements of elastic constants in Y$_2$TiO$_5$, but the match between the DFT and the MD or GULP calculated values is better.

4.4.5 Study of diffusion coefficient for the two systems

Diffusion coefficient can be calculated using Einstein's relation $D = \frac{<r^2>}{6t}$, where $<r^2>$ is the mean square displacement of the atoms. Thus, for both the systems, we first calculate the mean square displacement accounting for the periodic boundary conditions. The Arrhenius plots for diffusion coefficients calculated for Y, Ti

4.4.4 Calculation of elastic constants

Elastic constants measure the resistance a material offers against the applied stress. The elastic constant matrix is a 6 × 6 matrix. However, because of the symmetry, many of the elements of the matrix are equal. In the case of $Y_2Ti_2O_7$, the unique elastic constants are $C11$, $C22$ and $C44$, while for Y_2TiO_5, there are 9 elastic constants, that are $C11$, $C22$, $C33$, $C44$, $C55$, $C66$, $C12$, $C13$ and $C23$. To calculate the elastic constants, we took a unit cell of the given system and carried out molecular statics runs at $T = 0$ K, $P = 0$ bar by giving small distortions to the simulation box in different directions and then calculating the resulting change in the total energy. Table 4.4 shows a comparison of the calculated values for both the systems with the corresponding DFT data, as well as with the available experimental data in the case of $Y_2Ti_2O_7$. The matches are seen to be reasonable. If a crystal structure possesses an inversion center and if the interactions between the atoms can be described by a central potential between the atoms, then the elastic constants should follow Cauchy's relationship between the elastic constants, i.e, $C12 = C66$, $C13 = C55$, $C14 = C56$, $C23 = C44$, $C25 = C46$ and $C36 = C45$ for a triclinic system [149]. For orthorhombic crystals, this reduces to $C12 = C66$, $C13 = C55$, and $C23 = C44$, while for cubic crystals it means that $C12 = C44 = C66$. Non compliance with Cauchy's relations is an indication of the anisotropic nature of the central potential in crystals with a center of inversion. For $Y_2Ti_2O_7$ crystal, apparently, the Cauchy relationship is seen to be violated in DFT calculations, while it is satisfied in experiments as well as in the case of calculations using interatomic potentials. Cauchy violation, in case it is present, can be observed by many-body potential models [143].

The bulk and shear modulus are calculated from the MD calculated elastic constants using the Voigt average, where, bulk modulus, $B_{Voigt} = \frac{1}{3}(A + 2B)$, and shear modulus, $G_{Voigt} = \frac{1}{5}(A - B + 3C)$ and Young's modulus, $E_{Voigt} = \frac{(A-B+3C)(A+2B)}{(2A+3B+C)}$. Here, $A = \frac{1}{3}(C11 + C22 + C33)$, $B = \frac{1}{3}(C12 + C23 + C13)$ and $C = \frac{1}{3}(C44 + C55 + C66)$ [151]. These values are compared with the GULP, DFT and experimental data for bulk and shear modulus for $Y_2Ti_2O_7$. While GULP and

are only 6 independent parameters. Further, higher the symmetry of the crystal, lower will be the number of independent thermal coefficients. Since $Y_2Ti_2O_7$ is a cubic system, all the off-diagonal elements of the thermal coefficient matrix are zero, while the diagonal elements are all equal. Hence, $\alpha_{11} = \alpha_{22} = \alpha_{33}$ and thermal expansion is isotropic. Since Y_2TiO_5 has an orthorhombic structure, thermal expansion will not be isotropic and a difference in the temperature variations of α_{11}, α_{22} and α_{33} is expected.
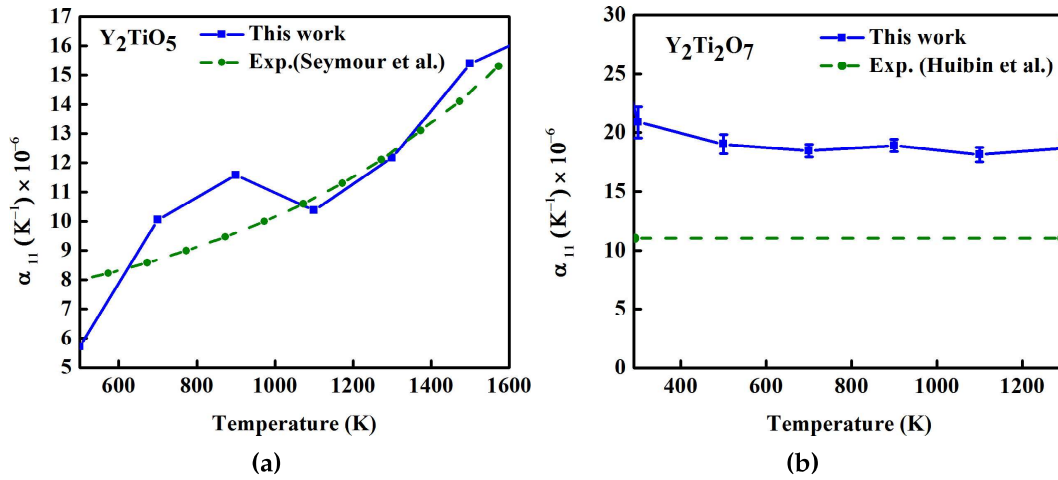
Figure 4.7 – Coefficient of thermal expansion (α_{11}) compared with experimental results for (4.7a) Y_2TiO_5, experiment ref: Seymour *et. al* [148]; (4.7b) $Y_2Ti_2O_7$, experiment ref: Huibin *et. al* [26].

Fig. 4.7 shows the variation of thermal coefficient α_{11} vs temperature. Experimentally observed α_{11} for Y_2TiO_5 [148] and $Y_2Ti_2O_7$ [26] are compared with the calculated values of α_{11} using molecular dynamics. As seen in Fig. 4.7a and Fig. 4.7b, for the temperature range considered, α_{11} increases with temperature for Y_2TiO_5 but remains almost constant for $Y_2Ti_2O_7$. Similar trends are also seen in experiments. In the case of Y_2TiO_5, since it has an orthorhombic structure, ideally one should get a different variation for α_{11}, α_{22} and α_{33} as seen in experiments [148]. However, our potential predicts similar values for all the three coefficients and hence only α_{11} is shown in the plots.

peaks after the second peak disappear after the melting point.
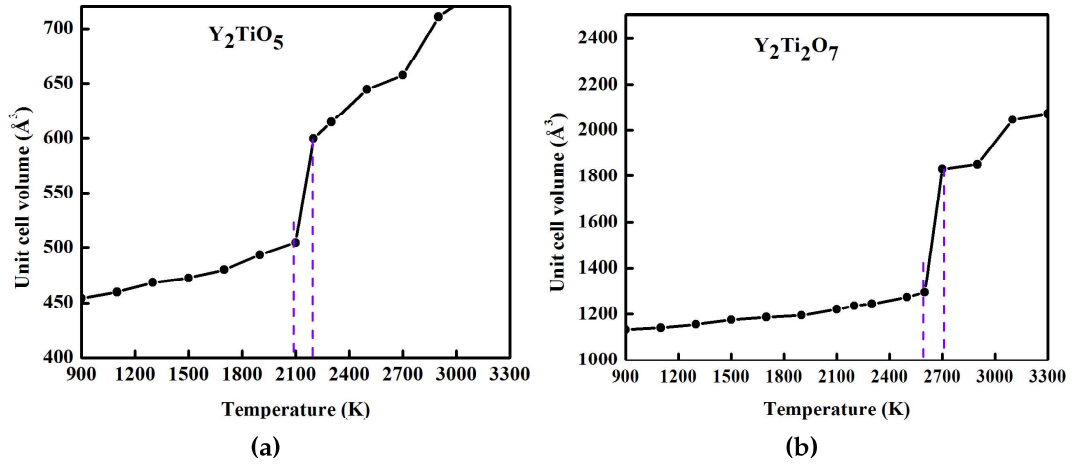
Figure 4.5 – Unit cell volume vs temperature in NPT ensemble: (4.5a) Y_2TiO_5; (4.5b) $Y_2Ti_2O_7$.
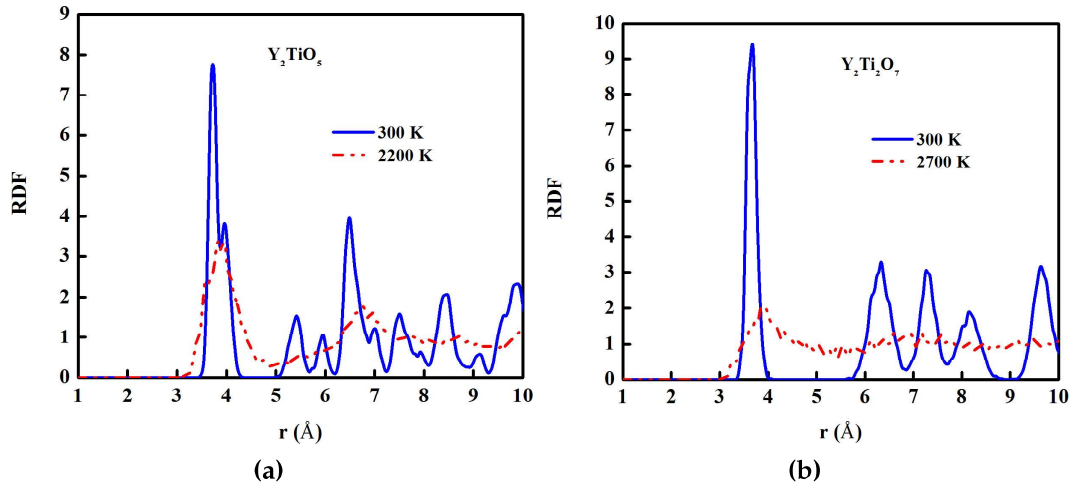
Figure 4.6 – A comparison of RDF of a melted system and a system equilibrated at 300 K (Pressure = 1 bar): (4.6a) Y_2TiO_5; (4.6b) $Y_2Ti_2O_7$.

The coefficient of thermal expansion is a measure of the expansion of lattice parameter of a system upon heating. It is a second rank tensor which relates the strain in the lattice and the temperature. It can be represented as:

$$\frac{\triangle l}{l} = \begin{bmatrix} \alpha_{11} & \alpha_{12} & \alpha_{13} \\ \alpha_{21} & \alpha_{22} & \alpha_{23} \\ \alpha_{31} & \alpha_{32} & \alpha_{33} \end{bmatrix} \triangle T \tag{4.8}$$

However, since thermal expansion possesses a reciprocity in its elements, there

79
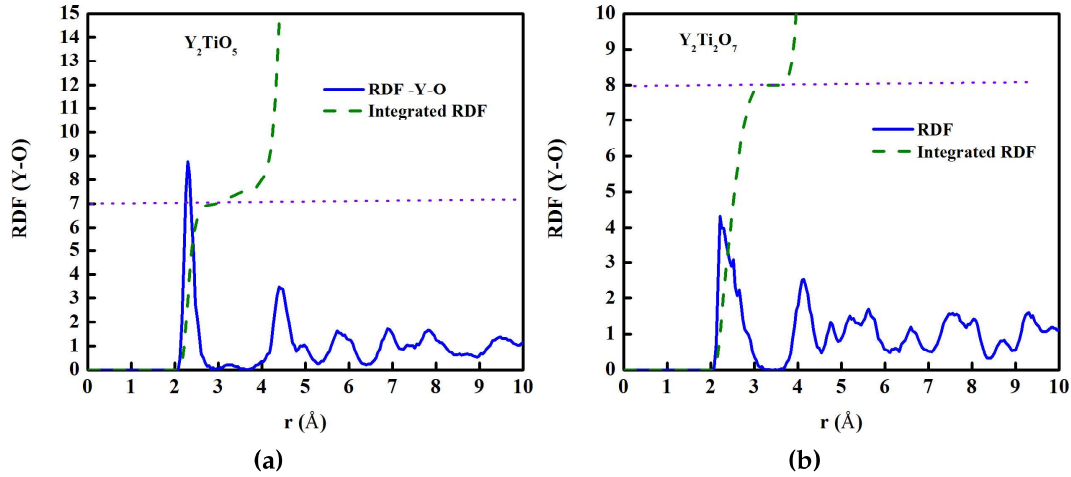
Figure 4.4 − Pair distribution function and the integrated pair distribution function plotted for Y-O, at $T = 300K$, $P = 1$ bar (4.4a) Y_2TiO_5; (4.4b) $Y_2Ti_2O_7$.

ful monitoring of the phonon dispersion curves to ensure better thermal properties. Now we check, whether this effort has paid off or not, by calculating the melting points (MP) of both the systems. Melting of a system is related to a sudden jump in the volume of the unit cell. At the melting point, all the atoms of the crystal start vibrating with an amplitude much higher than that in equilibrium configurations below the melting temperature. This results in the ionic dynamics being controlled by the anharmonic part of the interatomic potential, which leads to a shift in the mean ionic positions, thus leading to an abrupt change in the volume of the crystal. MP can be roughly estimated as 10% less than the temperature of the abrupt transition, as observed in Al_2O_3 and Y_2O_3 [17].

Thus, to calculate MP of both the systems, we vary the temperature of the systems at constant pressure and equilibrate them for a total equilibration time of 1 ns in steps of 0.05 ps. Fig. 4.5 shows the variation of unit cell volume with temperature. As shown in Fig. 4.5a and Fig. 4.5b respectively, the abrupt change in volume comes at $\sim$ 2150 K for Y_2TiO_5 and at $\sim$ 2650 K for $Y_2Ti_2O_7$. Thus, the melting points of Y_2TiO_5 and $Y_2Ti_2O_7$ is estimated as 1935 K and 2385 K respectively. These values of melting point are encouraging as they are quite near to the experimental MP of $\sim$ 2000 K [25] and $>$ 2173 K [26] for Y_2TiO_5 and $Y_2Ti_2O_7$ respectively. Fig. 4.6 shows the RDF after MP for both the systems, along with the RDF corresponding to 300 K temperature. It can be seen from the figure that all the

Formation energies (eV)	Y$_2$TiO$_5$		Y$_2$Ti$_2$O$_7$	
Frenkel pair (FP)	*GULP*	*DFT*	*GULP*	*DFT*
Y	6.058	5.507	6.091	2.727
Ti	5.899	6.650	8.547	4.235
O	2.329	2.883	2.985	4.949
AS Pair				
Y-Ti	1.606	2.612	0.097	3.472
Y-O	11.194	2.563	2.942	4.698
Ti-O	9.765	13.155	7.309	–
AS pair (Y-Ti) + FP				
Y^1	5.583	–	6.491	–
Ti	5.742	–	9.458	–
O*	1.728	–	2.924	–
Schottky defect	13.556	–	18.848	–

Table 4.3 – A comparison of point defect formation energies calculated using GULP and DFT calculations for both Y$_2$TiO$_5$ and Y$_2$Ti$_2$O$_7$. Y = Y^1 in both the systems, while O = O^5 in Y$_2$TiO$_5$, and O = O^2 for Y$_2$Ti$_2$O$_7$. * O^1 atom taken in the case of Y$_2$Ti$_2$O$_7$.

all these calculations consists of equilibrating the simulation cell for 1 ns at a given temperature and a pressure of 1 bar, using Nosé-Hoover thermostat and barostat.

The crystallinity of systems can be analysed using radial distribution function (RDF) as it provides an information about the immediate neighborhood of an atom. The plots of partial RDF, along with the corresponding integrated coordination number for Y-O bond for both Y$_2$TiO$_5$ and Y$_2$Ti$_2$O$_7$ at temperature 300 K and pressure 1 bar are shown in Fig. 4.4a and Fig. 4.4b respectively. It is seen that the systems are crystalline at this temperature, as all the peaks are quite sharp. For Y$_2$TiO$_5$, the Y-O and Ti-O interatomic distances, as obtained from the corresponding partial RDF are 2.31 Å and 1.94 Å respectively (experimental value: Y-O= 2.29-2.40 Å; Ti-O= 1.78-1.94 Å [146]) while the corresponding values in Y$_2$Ti$_2$O$_7$ are 2.21 Å and 1.95 Å respectively. The integrated RDF shows that the coordination number (O surrounding Y atom) is strictly zero before 2 Å for both the systems. At the peak, there are 8 O atoms surrounding the Y atom in Y$_2$Ti$_2$O$_7$, and the number sharply increases at the second peak. In Y$_2$TiO$_5$, the integrated RDF varies from ∼6 to ∼7 at peak.

As mentioned in section 4.3, the development of potentials consisted of a care-

$$\triangle E_f^{(X,Y)} = E^{(X,Y)} - E_{tot} \tag{4.5}$$

Where, $E^{(X,Y)}$ = total energy of the system having X_Y and Y_X antisites, E_{tot} = Energy of the ideal structure.

Further, we also calculate the FP energy of an atom in a system which is already having an antisite pair defect. For this, we create a FP of the particular atom (Z) in an equilibrated system having an antisite pair. The defect formation energy ($\triangle E$) can be calculated by subtracting the energy of the system having the antisite pair from the energy of the system having the antisite pair as well as FP of the Z atom.

$$\triangle E = E_{FP(Z)}^{(X,Y)} - E^{(X,Y)} \tag{4.6}$$

Where, $E_{FP(Z)}^{(X,Y)}$ = Energy of the system having X_Y and Y_X antisites as well as a FP of Z atom. $E^{(X,Y)}$ = total energy of the system having X_Y and Y_X antisites.

A Schottky defect is created by a removal or addition of a complete formula unit of the system. If N_f is the number of formula units in the ideal structure, while $N_f - 1$ is the number of formula units present in the defective structure, then Schottky defect energy can be calculated as:

$$\triangle E^{Schottky} = E^{Sch} - \frac{(N_f - 1)}{N_f} E_{tot} \tag{4.7}$$

Where, E^{Sch} = total energy of the system having a Schottky defect, E_{tot} = total energy of the ideal structure.

Table 4.3 shows the defect formation energies for all the various configurations considered. In general, in both the systems, the cation antisite pair formation energy is quite small. This suggests towards the tendency for formation of cation antisites upon irradiation, seen in all pyrochlores [27].

4.4.3 Study of structural and thermal properties of the systems

Here, we present the study of structural and thermal properties for both the systems using the new interatomic potentials. The MD methodology adopted for
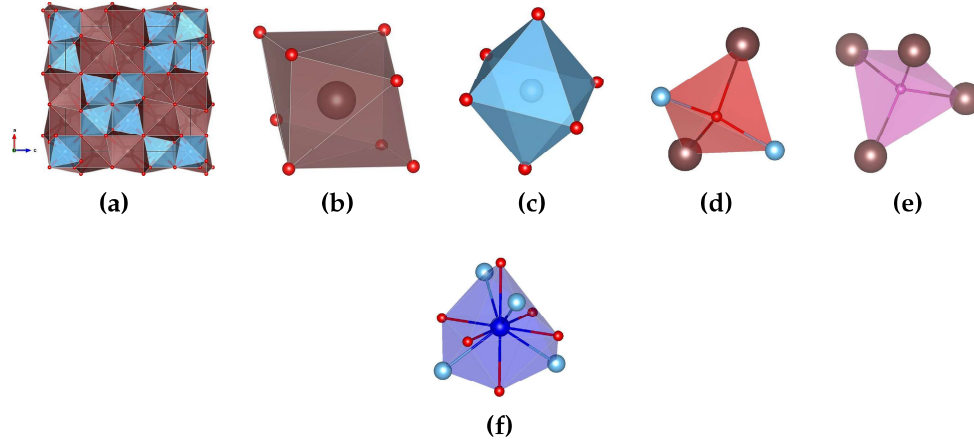
Figure 4.3 – (4.3a) $Y_2Ti_2O_7$ structure; (4.3b) YO8 polyedron; (4.3c) TiO6 polyhedron; (4.3d) O^1 site surrounded by two Y and two Ti atoms; (4.3e) O^2 site surrounded by 4 Y atoms; (4.3f) *8a* interstitial site in $Y_2Ti_2O_7$. *8a* site is surrounded by 6 O^1 atoms and 4 Ti atoms. The Interstitial site is represented by a fictitious atom. Y atoms: Brown, Ti atoms: Blue, O atoms: Red.

well as molecular statics calculations, the cell volume as well as the ion positions were relaxed. For DFT calculations, we took a simulation cell of size $1 \times 3 \times 1$ (96 atoms) for Y_2TiO_5 while for $Y_2Ti_2O_7$, a unit cell (88 atoms) was taken. For GULP calculations, we could go for bigger simulation cells, thus we took a simulation cell of $3 \times 6 \times 2$ supercell for Y_2TiO_5 and $2 \times 2 \times 2$ supercell for $Y_2Ti_2O_7$.

A Frenkel pair (FP) is created when a vacancy defect of X atom is created and a corresponding interstitial of the X atom is placed at some other place in the crystal lattice. In these studies, the site for placing the interstitial atom is *4a* in the case of Y_2TiO_5, and *8a* in $Y_2Ti_2O_7$. The FP energy can be simply calculated as

$$\triangle E_f^{FP(X)} = E^{FP(X)} - E_{tot} \tag{4.4}$$

where, $E^{FP(X)}$ is the energy of the defect structure and E_{tot} is the energy of the ideal structure.

An antisite (AS) defect is formed when an atom of one species occupies the lattice site of atom of another species. Here we calculate the antisite pair (AS pair) formation energy, which means the total energy of a pair of defects X_Y (X atom occupying the lattice site of Y atom) and Y_X. The AS pair energy $\Delta E_{(X,Y)}$ can be calculated as:

One of the O atom sites is shown in Fig. 4.2d, which shows an oxygen atom in a tetrahedron made up of Y atoms. For Frenkel pair calculations, we have chosen the $4a$ $(0,0,0)$ interstitial site which is surrounded by four oxygen atoms and two Ti atoms, as shown in Fig. 4.2e.
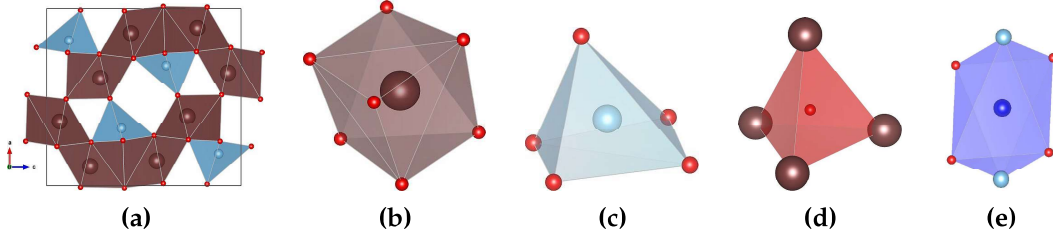
Figure 4.2 – (4.2a) Y_2TiO_5 structure; (4.2b) YO7 polyhedron; (4.2c) TiO5 polyhedron; (4.2d) OY4 tetrahedron; (4.2e) $4a$ interstitial site, having four O atoms and two Ti atoms as vertices, with the interstitial site being represented by a fictitious atom. Y atoms: Brown, Ti atoms: Blue, O atoms: Red.

$Y_2Ti_2O_7$ has a pyrochlore structure which is a cubic system with space group $Fd\bar{3}m$. There are two different lattice sites for oxygen, represented by O^1 and O^2. Y cations occupy $16d$ $(1/2, 1/2, 1/2)$, Ti atoms occupy $16c$ $(0,0,0)$ sites while O^1 and O^2, occupy $48f$ $(x, 1/8, 1/8)$ and $8b$ $(3/8, 3/8, 3/8)$ sites respectively [76]. If all the vacant $8a$ $(1/8, 1/8, 1/8)$ sites are filled with oxygen atoms, the structure will become the fluorite (space group: $Fm\bar{3}m$) structure. The crystal structure of $Y_2Ti_2O_7$ can be visualized as being made up of YO8 and TiO6 polyhedra, as depicted in Fig. 4.3a. The Y cation, as shown in Fig. 4.3b, is coordinated to six O^1 oxygen anions and two O^2 oxygen anions making a distorted polyhedron while the Ti cation is coordinated to six O^1 oxygen anions making a distorted octahedron, as shown in Fig. 4.3c. O^1 is surrounded by a tetrahedron formed by two Y atoms and two Ti atoms, while O^2 is surrounded by a tetrahedron formed by four Y atoms, as shown in Fig. 4.3d and Fig. 4.3e respectively. For the calculations of Frenkel pair formation energies the vacant $8a$ sites are chosen. The $8a$ site, as shown in Fig. 4.3f is surrounded by 6 O^1 atoms and 4 Ti atoms.

The defect formation energies were calculated using DFT as well as by molecular statics as incorporated in GULP [24], using the new interatomic potentials. The supercell approach was used for both the type of calculations. For both the DFT as

curve is less steep in both the cases, however it matches better for Y_2TiO_5. The minimum of MD calculated EOS of $Y_2Ti_2O_7$ shows a slight shift towards a larger value. However, in both the cases, the left side of the curves, as well as their slopes match better with the corresponding DFT calculated curves, which is an indication that these potentials are well suited for situations where the atoms come close to each other as in small volume/high pressure conditions.
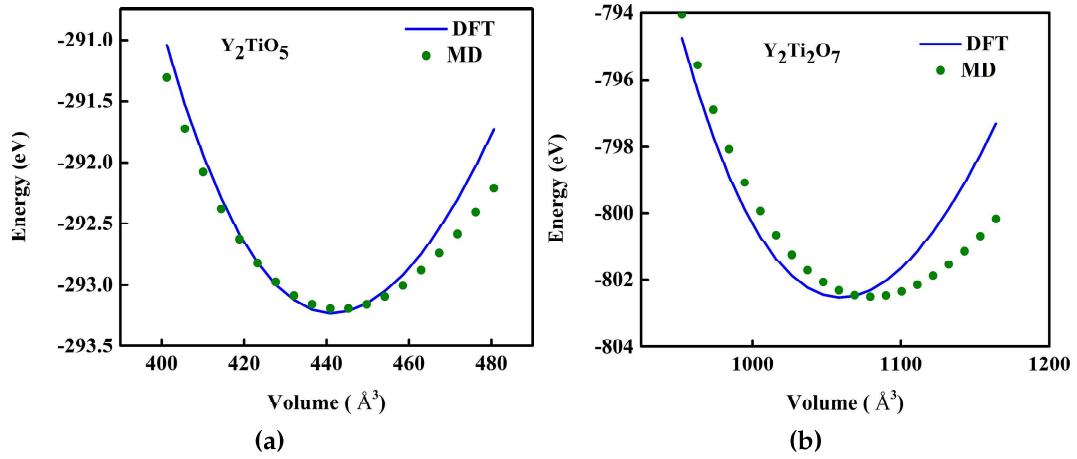
Figure 4.1 – Comparison of the equation of state energies obtained from DFT and MD: (4.1a) Y_2TiO_5; (4.1b) $Y_2Ti_2O_7$.

4.4.2 Defect formation energies

At a non-zero temperature, any crystal has defects due to statistical fluctuations. Moreover, in any energetic process, defects are produced. Thus, it is important to calculate the defect formation energies using the potentials. In this section, we discuss the results obtained from molecular statics calculations (using GULP) employing interatomic potentials and compare them with the defect formation energies calculated using DFT.

$\alpha - Y_2TiO_5$ has an orthorhombic structure, with space group Pnma, as shown in Fig. 4.2a. All atoms are in the Wyckoff positions 4c: (x, 1/4, z) [146]. Fig. 4.2b shows the larger Y cation being sevenfold coordinated to oxygen atoms, while Fig. 4.2c shows Ti cation being fivefold coordinated with oxygen atoms forming an off-center square pyramid. There are two different atomic sites for Y, denoted as Y^1 and Y^2, while there are 5 different atomic sites for O atoms, denoted as O^1 to O^5.

4.4.1 Lattice parameters

Calculation of the lattice parameters at finite temperatures is one of the important validation tests of the potential. As the database used for fitting the potentials is generated from the DFT calculations, which correspond to 0 K, this test acquires importance. Calculations of the lattice parameter at finite temperatures were carried out using molecular dynamics (MD) simulations as incorporated in LAMMPS package [13]. A $3 \times 9 \times 3$ cell (2592 atoms) of Y_2TiO_5 and a $3 \times 3 \times 3$ cell (2376 atoms) of $Y_2Ti_2O_7$ were first relaxed using conjugate gradient algorithm and then equilibrated at a temperature 300 K and pressure 0 bar for 1 ns using Nosé-Hoover thermostat and Nosé-Hoover barostat [89, 90]. Periodic boundary conditions were used in all the directions. The 0 K simulations required static relaxation of the system and hence, conjugate gradient algorithm is sufficient. Table 4.2 shows the lattice parameters at 0 K and at 300 K. Results from the molecular statics runs carried out in LAMMPS are compared with those using GULP, to test whether the two techniques predict similar results.

Y_2TiO_5				
Lattice paramters (Å)	*LAMMPS*	*GULP*	*DFT*	*Experiment*
a (0 K)	10.45	10.45	10.45	-
b(0 K)	3.69	3.69	3.72	-
c(0 K)	11.46	11.46	11.35	-
a(300 K)	10.52	10.54	-	10.35±0.01 [146]
b(300 K)	3.72	3.72	-	3.70±0.01 [146]
c(300 K)	11.53	11.55	-	11.25±0.01 [146]
$Y_2Ti_2O_7$				
a(0 K)	10.26	10.26	10.19	
a(300 K)	10.33	10.34	-	10.125± 0.023[147]

Table 4.2 – Lattice parameters for Y_2TiO_5 and $Y_2Ti_2O_7$.

Equation of state runs, with the lattice parameters varying isotropically from -10% to $+10\%$ of the equilibrium value are performed using MD by relaxing the structure at 0 K and the results are compared with the corresponding DFT results, which are shown in Fig. 4.1. The results shown in MD are shifted by the small difference in the minimum energy value along the energy axis to better represent the differences in the slopes of the $E - V$ curves. The right side of the parabolic

plied in the calculations of the total energy. Energy of the system was obtained by considering interatomic interactions corresponding to all the neighboring atoms within a cut off (r_c) of 11 Å. The parameters A_{ij}, ρ_{ij}, C_{ij} as well as the charges q_i and q_j were fitted until the cohesive energies calculated from *ab initio* and GULP calculations matched as closely as possible. The initial values for fitting of the potential parameters A_{ij}, ρ_{ij}, C_{ij} were taken from the paper by Hammond *et. al* [137], while the initial values of ionic charges q_i , q_j were taken from the paper by Jegan *et. al* [19]. Table 4.1 lists all the parameters obtained after fitting. The interatomic potentials for both the systems are thus generated using all the energies and atomistic configurations discussed as well as the checks that are required to ensure the reliability of the potentials.

	Y_2TiO_5			$Y_2Ti_2O_7$		
	A*(eV)*	**$\rho(Å)$**	**c*(eV Å⁶)***	**A*(eV)***	**$\rho(Å)$**	**c*(eV Å⁶)***
Y-Y	127806.27	0.263726	0.00	31745.091	0.276655	0.00
Y-Ti	10658.686	0.273455	0.00	3413.0489	0.271128	0.00
Y-O	85704.616	0.175203	0.00	45602.406	0.184449	0.00
Ti-Ti	99.979409	0.151575	0.00	56458.129	0.279597	0.00
Ti-O	9999.4023	0.201134	0.00	13539.444	0.190961	0.00
O-O	321084.03	0.176621	0.00	188903.85	0.180310	0.00
Charge	q_Y	q_{Ti}	q_O	q_Y	q_{Ti}	q_O
	1.690	1.840	-1.044	1.500	2.000	-1.000
Cut off, r_c(Å)	11			11		

Table 4.1 – Parameters for the pair potentials for Y_2TiO_5 and $Y_2Ti_2O_7$.

4.4 Results and discussion

After an interatomic potential is developed, the next major step is its validation. This is done by calculating various physical properties using the potentials and comparing them with the experimental or first principle values. Thus in this section, we discuss the calculations of the physical properties and see how well the potentials have performed.

was used for generating the **k** points grid with a mesh of $(4 \times 12 \times 4)$ **k** points for Y_2TiO_5 and $(4 \times 4 \times 4)$ **k** points shifted by $(0.5, 0.5, 0.5)$ for $Y_2Ti_2O_7$. Conjugate gradient algorithm was used for ionic relaxation steps. The ionic relaxations were stopped when the individual interatomic forces were smaller than 10^{-3} eV/Å. The total energy convergence was better than 10^{-9} eV for stopping the SCF cycle during the electronic iterations.

Twenty-one runs consisting of isotropic volume change within $\pm 20\%$ were carried out. Then, calculations for varying cell parameters along the x, y and z directions were performed. Since $Y_2Ti_2O_7$ is a cubic system, 9 such calculations were performed while 16 different runs were performed for Y_2TiO_5 as it has an orthorhombic structure. In order to take into account the angular distortions, calculations corresponding to different distortions with $\pm 5°$ angles between the lattice vectors **a**, **b** and **c** were carried out. These distortions and their total energies comprised the static configurations used in the fitting database. As the high energy processes generate defects in the system, consideration of the defect formation energies and its accuracy are important. Hence calculations were carried out for different defect configurations for vacancies, interstitials and Frenkel pairs of all the cations and anions using a $2 \times 2 \times 2$ supercell for $Y_2Ti_2O_7$ and $2 \times 6 \times 2$ supercell for Y_2TiO_5. For all these configurations, isochoric runs were performed. As the atoms come very close to each other in higher energy processes, it is required that the repulsive term in the Buckingham potential is modeled accurately. Thus, calculations corresponding to different positions of the interstitials with respect to varying distances from the nearest neighbour atoms were also carried out. At every step of the potential development, we always checked the corresponding phonon frequencies at the Brillouin zone center (Γ point) and made sure that none of the frequencies were imaginary. At any stage, if imaginary frequencies were obtained in the phonon dispersion, that step in the fitting was abandoned. This assured a better description of the thermal properties.

A nonlinear least square fitting as incorporated in General Utility Lattice Program (GULP) code [24] was carried out. Periodic boundary conditions were ap-

where, A_{ij}, ρ_{ij} and C_{ij} are the parameters of the Buckingham potential and r_{ij} is the interatomic separation.

4.3 Methodology for developing the interatomic potential

Development of the combined Coulomb-Buckingham potential for these systems requires fitting of the parameters A_{ij}, ρ_{ij} and C_{ij} for all the pairs of interacting ions, as well as their ionic charges q_i and q_j. In order to obtain the parameters for all the pairs of ions in the fitting procedure, we need to use various experimental or first principle calculations data. Our fitting data base consisted of the lattice and structural parameters and elastic constants obtained from the DFT calculations carried out for both the systems by Jiang *et. al* [145]. A reliable fit of all the potential parameters demands the use of an extensive set of data corresponding to different atomistic configurations, cell volume distortions, defect configurations and their total energies. Since this data is not available in the literature, we performed density functional theory (DFT) calculations [96, 97] as implemented in VASP package [20–23], which is a plane waves pseudopotential implementation of DFT. Projector augmented wave (PAW) [103] pseudopotentials and exchange-correlation functional as devised by Perdew-Burke-Ernzerhof (PBE) [100] were used in the calculations. In principle, it would have been better if a common, transferable potential function could model the interactions in both Y_2TiO_5 and $Y_2Ti_2O_7$, but our previous attempts to make it did not give satisfactory results, as unstable equilibrium configurations were obtained using the potential even for low-temperature simulations. The potential thus, was not able to reproduce the melting points of the two crystal systems. Further, the Y-O and Ti-O bond lengths and the bonding angles were also too much off from the DFT calculated values.

For Y_2TiO_5, a unit cell containing 32 atoms was taken, while a unit cell containing 88 atoms was taken for $Y_2Ti_2O_7$ in all the calculations. The cut off for kinetic energy was taken to be 520 eV for both the systems. Monhorst-Pack scheme [105]

potentials can model the Cauchy violation ($C_{12} \neq C_{44}$) exhibited by actinide oxides with fluorite structure.

To model the pairwise interactions between ions in Y_2TiO_5 and $Y_2Ti_2O_7$ crystal systems, we choose the Buckingham type pair potential [92] coupled with the Coulomb potential, as represented in eqn. 4.1. Buckingham potential is the most popular functional form for representing interactions in ionic materials. At short distances, the Buckingham term plays a significant role and is responsible for the minimum in the total potential. Buckingham potential as expressed in eqn. 4.3 comprises of a repulsive term decaying exponentially with increasing radial distance and an attractive term varying as r^{-6}, where r is the interatomic separation. The attractive term comes from the dipole-dipole interactions, while the repulsive term models the Pauli repulsion which dominates once the atoms approach so close to each other, such that their atomic shells start overlapping. Both the attractive and repulsive terms are important for a correct modeling of equilibrium properties. Further, in highly energetic situations, atoms come too close to each other and an accurate modeling of the repulsive term becomes very important. As long as the overlap between ionic shells is weak, one can assume that the magnitude of the repulsive interaction follows the same exponential decay form as followed by the electronic density function and hence the repulsive exponential term in Buckingham potential models the repulsion between electronic shells quite nicely [12]. The total potential function can be written as:

(Total potential)
$$U_{ij} = U_{ij}^{Coulomb} + U_{ij}^{Buckingham} \tag{4.1}$$

(Long-ranged)

$$U_{ij}^{Coulomb} = q_i q_j e^2 / r_{ij} \tag{4.2}$$

(Short-ranged)

$$U_{ij}^{Buckingham} = A_{ij} exp(-\frac{r_{ij}}{\rho_{ij}}) - C_{ij}/r_{ij}^6 \tag{4.3}$$

68

cades, shell models are unstable [144]. Thus, in MD simulations, shell models are not preferred and rigid ion potentials are much favoured as with them one can simulate large system sizes, which is also a prime requirement for displacement cascade studies. Thus, it was clear, that we required developing new interatomic potentials of the rigid ion type for Y_2TiO_5 and $Y_2Ti_2O_7$ crystals, suitable for simulating large system sizes in MD simulations.

In this chapter, we discuss the details of the development of the interatomic potentials for Y_2TiO_5 and $Y_2Ti_2O_7$ crystals. The chapter is organized as follows: The model and its details are discussed in section 4.2. The methodology used for fitting is discussed in section 4.3. The results obtained for different properties of the systems towards the validation of the potential are given in section 4.4 and the summary and conclusions are discussed in section 4.5.

4.2 Theory and the choice of model

The first principle calculations of the electron localization functions, charge densities and density of states of Y_2TiO_5 and $Y_2Ti_2O_7$ showed that these systems are predominantly ionic with only a partial covalent character (Ti-O bonds having higher covalency than Y-O bonds) [19, 145]. The analysis of Mullikan charges shows that the ionic charges are fractional instead of the integral charges of +3 for Y, +4 for Ti and -2 for O ions [19]. In ionic systems, oppositely charged ions are formed due to charge transfer and this leads to a strong Coulombic attraction between cations and anions. The force is strong and remains practically unaffected by the presence of other ions in the vicinity and is direction-independent [91]. The predominant ionic nature of these systems leads us to go for a potential function, which need not be strictly dependent on direction and hence, embedded atom method (EAM) potentials or pair potentials can be taken as model functions. Pair potentials have been traditionally used to describe ionic systems (for example, potentials for pyrochlores are mostly pair potentials [137–141, 144]), however, recently, EAM potentials also have been developed for ionic materials such as actinide oxides [143]. Since EAM potentials incorporate many-body effects, these

unavailable in the literature, or in case if some potential forms exist, those potentials are not suitable for our purpose. Hammond *et al.* [137] derived a Buckingham type pair potential for Fe-Y-Ti-O system. Their aim was to study the clustering behavior of Y-Ti-O solute atoms in Fe matrix using off-lattice Monte Carlo simulations. This potential treats the Y, Ti, O atoms as charge neutral species, which is a valid approximation as they are embedded in Fe matrix, wherein the ionic charge gets neutralized by the free electrons of the metal lattice. Neglecting the charges on ions gives an advantage in the speed of calculations as the long-range Coulombic forces don't need to be calculated. The potential gives good results in the dilute limit of Y, Ti, O solutes in the Fe matrix, but is not very satisfactory when used for crystal systems of Y_2TiO_5 and $Y_2Ti_2O_7$, as imaginary phonon frequencies are obtained for Y_2TiO_5 and the crystalline configurations of both the systems are unstable in MD equilibration runs performed even for room temperature.

Recently Sattony *et. al* [77] used a tight-binding variable-charge model for $Y_2Ti_2O_7$ crystal to study the amorphization characteristics in it. However, details of the potential are not very clearly discussed in the paper. In principle, the pairwise interactions between the different ionic species in Y_2TiO_5 and $Y_2Ti_2O_7$ crystals could have been taken from some of the popular shell model based interatomic potentials available in the literature [138–141]. Shell models are able to account for some many-body effects by making the interactions depend on coordination. The polarizability of ions in this model is incorporated by splitting an ion into a positive core associated with a negatively charged massless shell. The internal energy of this system is taken to be harmonic with respect to the core-shell displacement [142]. However, since shells represent massless entities, they are difficult to handle in the standard MD algorithm. There are some ways to incorporate the shell models in MD studies, for instance, by assigning a nominal mass to the shell, or by updating the shell positions through a static energy minimization stage performed for each MD time step. However, all such methods lead to very long calculation-times, thus limiting the time and the system size that can be simulated [143]. Further, in highly non-equilibrium conditions, such as those generated by displacement cas-

Chapter 4

Development of interatomic potentials for Y_2TiO_5 and $Y_2Ti_2O_7$ crystals

In this chapter, we discuss the development of interatomic potentials for Y_2TiO_5 and $Y_2Ti_2O_7$ crystals. An extensive set of first principle calculations data is generated for a reliable fitting of the potential parameters and the generated potentials are used for studying various physical properties.

4.1   Introduction

Molecular dynamics is a very efficient technique to probe the atomic systems and it can provide the dynamical as well as the statistical picture of the atomic systems simultaneously. One can actually track the individual atoms and observe the mechanism of the processes in detail. However, the results obtained from MD simulations crucially depend upon the robustness of the potential functions used to describe the interatomic interactions in the systems. A carelessly chosen potential function can lead to spurious results [12].

In the contextual envelope of this thesis, we required interatomic potentials that can satisfactorily model Y-Ti-O crystals and can be used for displacement cascade studies. For Y_2O_3, as discussed earlier, we used the interatomic potential by Belonoshko *et. al* [17] which is an appropriate potential for the current studies [136], but the case of Y_2TiO_5 and $Y_2Ti_2O_7$ is different. Either the interatomic potentials are

for any particular application requires an optimization for the desired properties. For example, for their use in ODS steels, not only the precipitates are required to be resistant to amorphization, they should also be able to effectively trap helium produced in the reactors. In this regard, it has been seen from the first principle studies [156], that helium is in fact, more deeply trapped in Y_2TiO_5 as compared to $Y_2Ti_2O_7$. Moreover, it is suggested that at elevated temperatures, Y_2TiO_5 may stand more effective than $Y_2Ti_2O_7$ in pinning the dislocations [145]. Thus, one needs to have a complete overview of the comparative behavior of these systems under different conditions for designing better radiation-resistant materials.

Summary of the results comparing Y-Ti-O systems:

- In Y_2O_3 and $Y_2Ti_2O_7$, the short and medium-range order persists even at the peak of cascade. In Y_2TiO_5, these orders vanish and the system behaves like a melt.

- Constraints analysis and strain energy calculation in the distorted systems show that $Y_2Ti_2O_7$ is more constrained as compared to Y_2O_3 and Y_2TiO_5.

- After the displacement cascade subsides, least number of FPs survive in Y_2O_3, indicating its strong bonding characteristics. The highest number of FPs survive in the case of Y_2TiO_5.

- Ballistic diffusion is highest in Y_2TiO_5, followed by $Y_2Ti_2O_7$ and then Y_2O_3.

- The number of antisites produced, as well as survived, are the least in Y_2O_3.

- The number of cation antisites surviving in $Y_2Ti_2O_7$ is larger than that in Y_2TiO_5, indicating towards higher amorphization resistance of $Y_2Ti_2O_7$ as compared to Y_2TiO_5.

- After displacement cascade subsides, Y_2O_3 and $Y_2Ti_2O_7$ almost recover their initial topologies, while a complete recovery of the initial topology doesn't occur in the case of Y_2TiO_5.

In general, we can say, Y-Ti-O systems are constrained systems, and should be quite stable under irradiation. In all the properties studied, Y_2O_3 and $Y_2Ti_2O_7$ fair better than Y_2TiO_5 in terms of radiation stability and resistance to amorphization. Y_2O_3 seems to be very resilient against radiation damage, as least number of point defects and antisites survive in it. However, $Y_2Ti_2O_7$ also stands quite good, albeit from a different view, as the cation antisites produced in it point towards its high resistance to amorphization. Moreover, the topological order is also quickly regained in both the systems. From these studies, Y_2TiO_5 seems to be comparatively less resistant to amorphization, and one may conclude it to be inferior to Y_2O_3 and $Y_2Ti_2O_7$. However, it should be remembered, that material selection and design

duced by heating them at high temperatures, as well as by inducing displacement cascades. Displacement cascade studies were carried out for different PKA energies and initial equilibration temperatures of the lattice. Now we summarise all the results.

Summary of the general results

- A radiation-damaged system can have a clearly different topology from a corresponding melted system, and this difference can be effectively discerned by ring analysis.

- In Y-Ti-O systems, a prediction of amorphization resistance by two completely different approaches, the constraints analysis which considers only the structure type of the materials, and by a calculation of strain energy in the distorted systems by explicitly incorporating the interatomic potentials, agree well and show that these systems are constrained, and must be resistant to amorphization.

- A delayed production and an apparent saturation of cation antisites is observed in Y_2TiO_5 and $Y_2Ti_2O_7$. Oxygen disordering to alternative lattice sites is not discernible in any of the cases. $Y_2Ti_2O_7$ undergoes an incomplete order-disorder transition for the PKA energies considered in this study.

- The effect of initial temperature (T) on the cascade characteristics is marginal in the case of properties such as MSD, temperature in the cascade region, etc. However, its effect is seen in the case of point defects. The measured quantities (eg., the peak number of FPs and antisites, the surviving number of FPs and antisites, etc.) in general, increase as T increases.

- The effect of PKA energy (E_{PKA}) is to increase any of the measured quantities, except the time ($t_{peak}(HKE)$) to reach the maximum number of HKE atoms, where, as E_{PKA} increases, $t_{peak}(HKE)$ decreases.

study of radiation damage in zirconolite [15], it was observed, that while in the crystalline zirconolite, there is no edge-sharing between the Ti polyhedra, in the damaged system, a new order due to edge-sharing between Ti polyhedra emerges.

To test whether the Ti_2 rings in $Y_2Ti_2O_7$ have actually arisen due to the edge-sharing of TiO6 polyhedra, we carry out the coordination analysis of all the Ti atoms involved in the Ti_2 rings. It can be seen from Fig. 5.24, Ti atoms in the Ti_2 rings have a mixed coordination of oxygen atoms, and most of them are not TiO6 polyhedra. It seems, in $Y_2Ti_2O_7$, the emergence of Ti_2 rings cannot be directly correlated to the edge-sharing, as it may have arisen due to the formation of cation antisites (thus a Ti atom replacing a Y atom of the Y polyhedra, which was already sharing edges with other Ti polyhedra). Further, in the disordered system, the polyhedra can be distorted, as well as some oxygen atoms can come nearby to Ti atoms due to disorder, which may lead to extra connectivities. These effects would be local rather than arising due to a global change in the topology. This shows that contrary to the case in zirconolite, the radiation damaged $Y_2Ti_2O_7$ does not show any edge-sharing between the Ti polyhedra, and hence, does not show emergence of any new topological order.

In section 5.5.3, by analyzing the partial RDF of oxygen atoms, we found that there was no evidence for a complete order-disorder transition in Y-Ti-O systems. To complement that study, we carried out the ring analysis for various defect-fluorite configurations and compared the results with the rings for damaged $Y_2Ti_2O_7$ and Y_2TiO_5 systems. However, we did not find any resemblance in all the cases. This indicates, in the present simulations, neither Y_2TiO_5, nor $Y_2Ti_2O_7$ undergo a complete order-disorder transition to defect fluorite structure.

5.7 Summary and conclusions

In this chapter, we focussed on two main issues, a study of displacement cascades, and a comparative study of Y-Ti-O systems under different conditions. The systems were analyzed with respect to their structures and topologies, their interatomic interactions, and with respect to their response to dynamic disorder in-
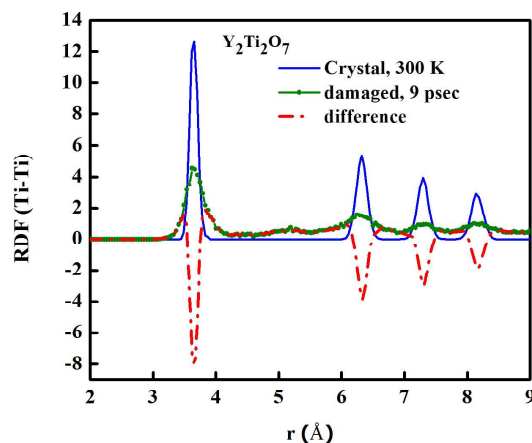
Figure 5.23 – Comparison between the partial RDF of Ti atoms in $Y_2Ti_2O_7$ for the crystalline system (300K) and radiation-damaged system at the end of the simulation time (9 psec). For a better comparison, a difference of Ti partial RDF for the damaged and crystalline systems is also plotted (red curve).

cates edge-sharing between polyhedra is quite less at this stage. 4-rings quickly recover approximately to their initial numbers, which shows the short-range order is maintained quickly.
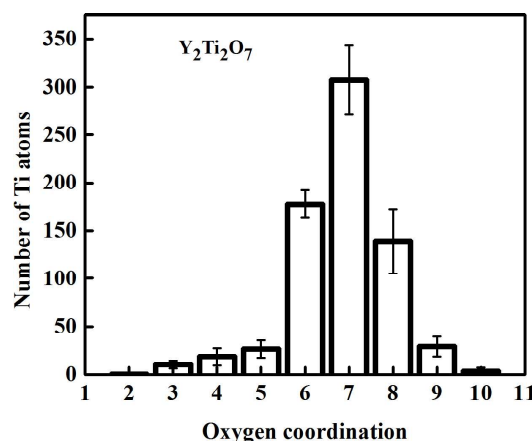
Figure 5.24 – Number of Ti atoms in $Y_2Ti_2O_7$, which are involved in Ti_2 rings, vs their corresponding oxygen coordination number

As can be seen from Fig. 5.22c, in the case of $Y_2Ti_2O_7$, new Ti_2 rings are seen to be formed by the end of the cascade, while there is no such new emergence of another type of rings in Y_2TiO_5. A corresponding study of partial RDF of the Ti atoms, as shown in Fig. 5.23 does not show any such feature emerging for the positions of Ti atoms in the damaged system. The formation of new Ti_2 rings may indicate towards edge-sharing between TiO6 polyhedra, and thus, towards a change in the topology of the radiation damaged $Y_2Ti_2O_7$. For instance, in a similar result in the

the compositional changes occurring in the rings. For instance, if a 4-ring, say Y-O-Ti-O got replaced by a Y-O-Y-O ring, it did not affect the total count of the 4-rings in the system. This was done, as we did not want to discard a ring formed by a different sequence of cation atoms, as cation antisites are a common and favorable feature and are easily formed in pyrochlores [51, 52]. However, now we explore in detail the compositional changes that can occur to rings. These will happen only in the case of Y_2TiO_5 and $Y_2Ti_2O_7$, as Y_2O_3 has only a single type of cation in it. We focus our attention to 4-rings, as they signify edge sharing between the corresponding polyhedra.
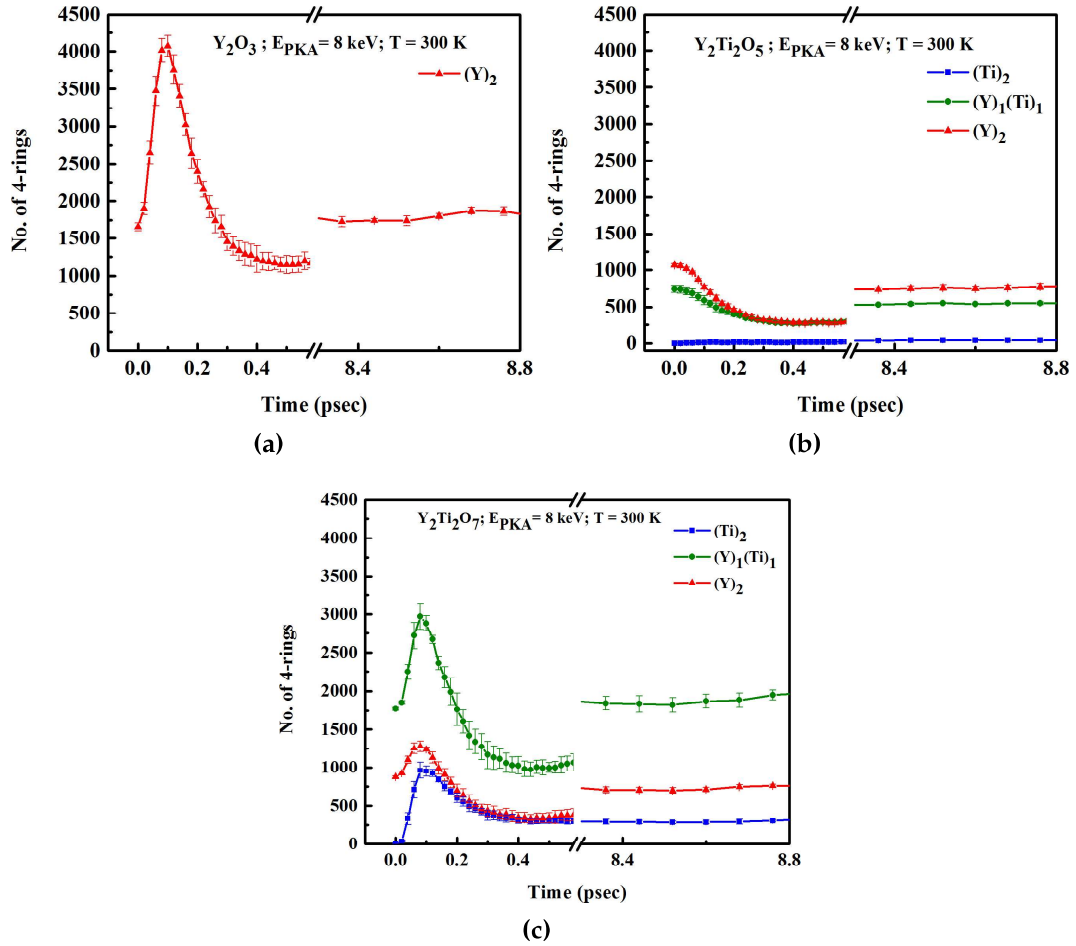
Figure 5.22 – Variation of the number of 4-rings with time in displacement cascade. $E_{PKA}= 8$ keV; $T = 300$ K. Notation: $A_1B_1=$ A-O-B-O ring; $A_2 =$ A-O-A-O ring. (5.22a) Y_2O_3; (5.22b) Y_2TiO_5; (5.22c) $Y_2Ti_2O_7$.

Fig. 5.22 shows the time evolution of the different types of 4-rings under displacement cascade. The reduction in the number of 4-rings at thermal spike indi-

5.6.3 Evolution of rings in displacement cascades

Now we study the evolution of rings with time in a displacement cascade event. Fig. 5.21 shows the variation of the number of rings of order 4, 6 and 8 with time in displacement cascade. As can be seen, rings get annihilated at the time (t_{peak}) when the cascade is at its peak and as the cascade subsides, the rings start recuperating. However, while rings of all the orders almost recover in Y_2O_3 and $Y_2Ti_2O_7$, a complete recovery of all the rings does not occur in the case of Y_2TiO_5. This indicates that Y_2O_3 and $Y_2Ti_2O_7$ lattices are better than Y_2TiO_5 in regaining the topological order after the cascade gets subsided.
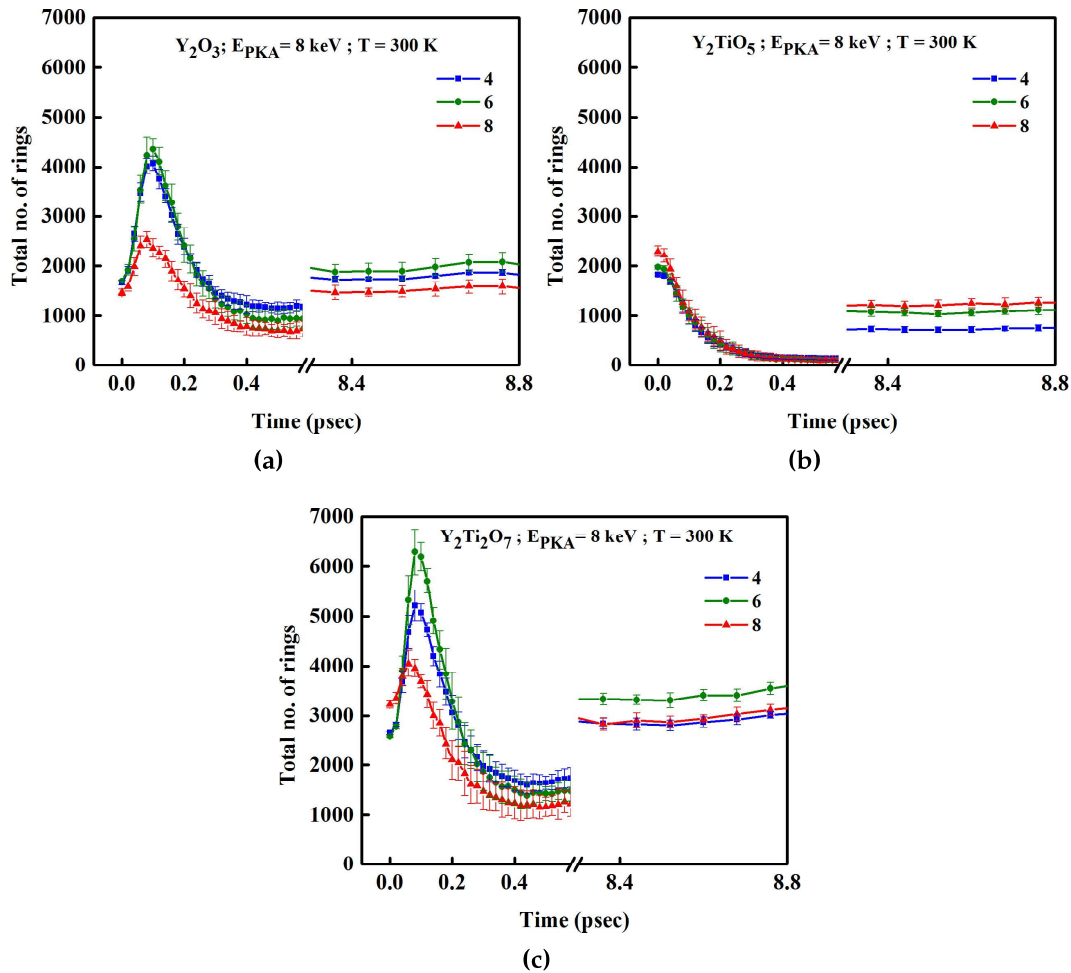
Figure 5.21 – Variation of the total number of rings with time in displacement cascade. E_{PKA} = 8 keV; T = 300 K. (5.21a) Y_2O_3; (5.21b) Y_2TiO_5; (5.21c) $Y_2Ti_2O_7$.

Up to now, in our all discussions on ring analysis, we focussed only upon the global topological changes signified by the rings of particular orders and ignored
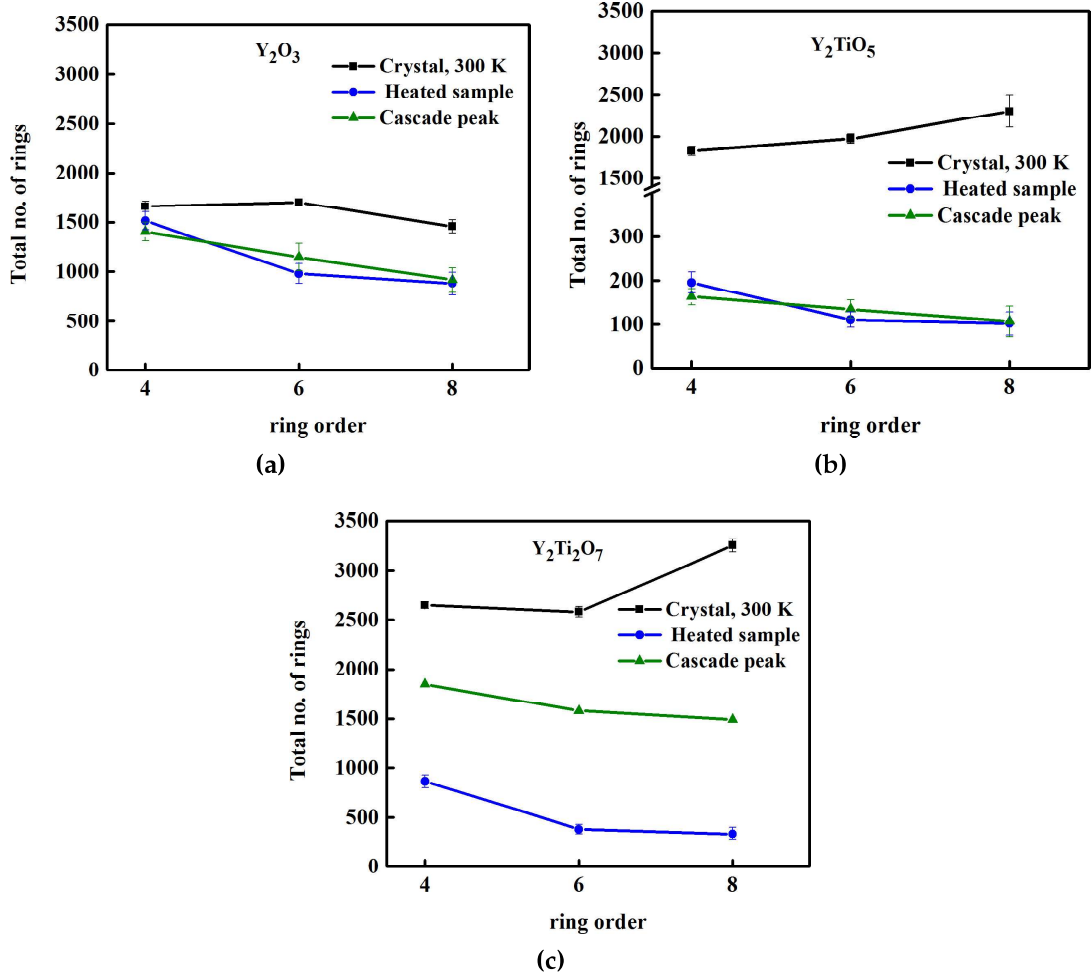
Figure 5.20 – Comparison of ring analysis for crystal equilibrated at 300 K, system equilibrated at temperature $Temp_{(peak)}$ (heated sample), and the radiation damaged system at the time when cascade is at its peak in it (cascade-peak sample). (5.20a) Y_2O_3; (5.20b) Y_2TiO_5; (5.20c) $Y_2Ti_2O_7$. $Temp_{(peak)}$ for Y_2O_3: 4780 K; Y_2TiO_5: 4630 K; $Y_2Ti_2O_7$: 4770 K.

tem is disordered, it still retains its short and medium-ranged order to a certain degree, and thus, its topology does not deviate much from that of the crystalline configuration.

In the case of Y_2O_3, as seen from Fig. 5.20a, the radiation-damaged system appears to be closer to the heated system. However, a closer look at the figure suggests, that the heated system, which was equilibrated at a very high temperature, itself does not deviate too far from its crystalline counterpart. This suggests that Y_2O_3 has got a very resilient bonding, and the short and the medium-ranged orders do not completely vanish in it even when the system is equilibrated for a long time at a high temperature.
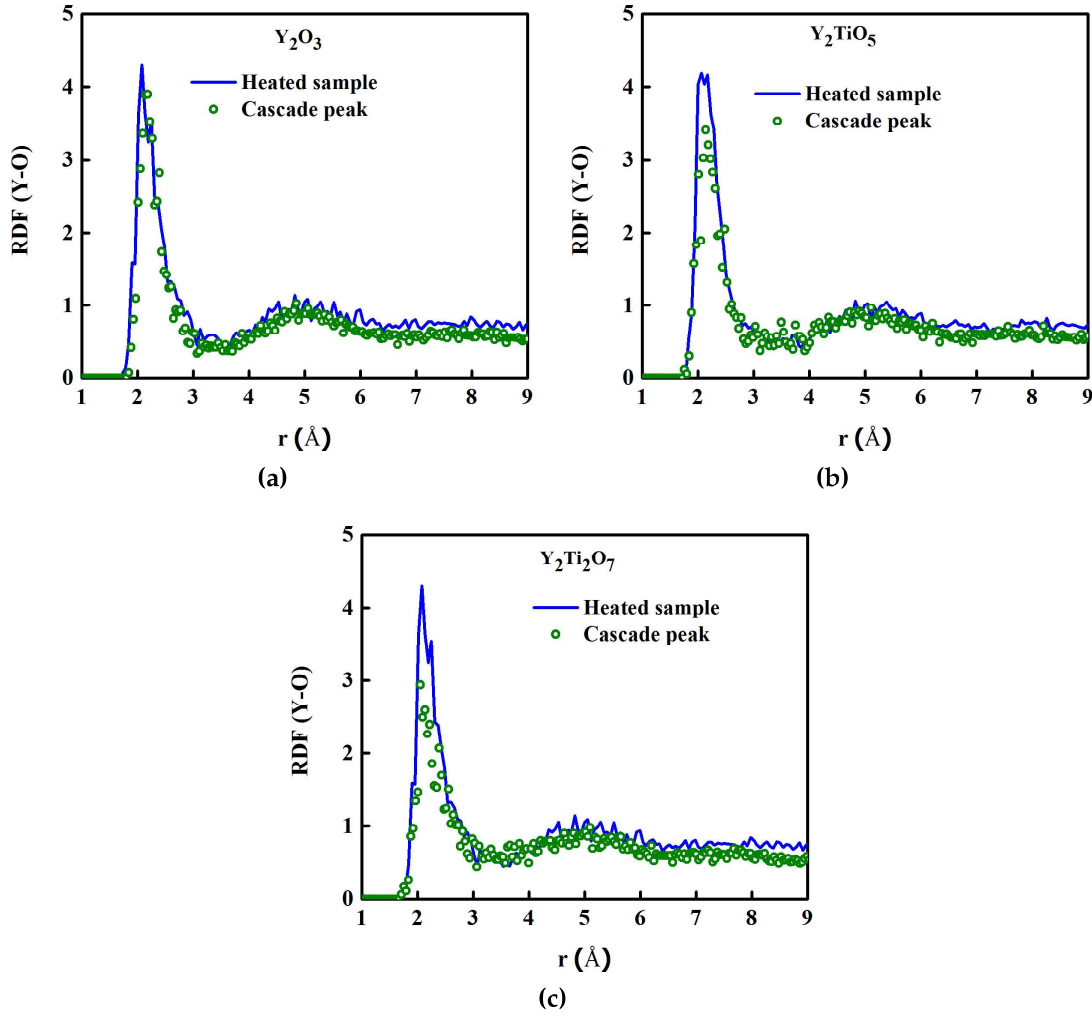
Figure 5.19 – Comparison of partial RDF (Y-O) between system equilibrated at temperature $Temp_{(peak)}$ (heated sample) and the radiation damaged system at the time when cascade is at its peak in it (cascade-peak sample). (5.19a) Y_2O_3; (5.19b) Y_2TiO_5 (5.19c) $Y_2Ti_2O_7$. $Temp_{(peak)}$ for Y_2O_3: 4780 K; Y_2TiO_5: 4630 K; $Y_2Ti_2O_7$: 4770 K.

In Y_2TiO_5, as seen from Fig. 5.20b, the topology of the radiation damaged system is far deviated from its crystalline counterpart and is completely similar to the heated sample. That shows, in the case of Y_2TiO_5, even the short and medium-range order is disrupted considerably at the peak of the cascade, and the radiation damaged system indeed behaves like a melt.

However, Fig. 5.20c shows that in the case of $Y_2Ti_2O_7$, there is a clear difference between the radiation damaged system and the corresponding system equilibrated at $Temp_{(peak)}$. The rings pattern is quite different from that of the heated sample and has not deviated much from the crystalline system as compared to the heated sample. This shows, in the case of $Y_2Ti_2O_7$, although the radiation damaged sys-

118

In the next section, we study radiation damaged system and a system equilibrated at a high temperature, using RDF and ring analysis. Since in Y-Ti-O systems, whether the disorder occurs due to melting or due to displacement cascades, a long-range order is not seen to emerge at any stage, thus now onwards we show only 4, 6 and 8 order rings in all the subsequent plots.

5.6.2 Difference between radiation damaged and heated system

Displacement cascades impart a substantial amount of energy in a localized region which leads to a production of lattice defects, as well as a sudden rise in the temperature of the affected region. The cascade region, at the thermal spike, is highly disordered and by an analysis of RDF, it is said that the cascade-core gets melted and becomes like a liquid [61, 64, 65, 153]. However, Hobbs *et. al* [31] argue, that the radiation damaged system can be quite different from a liquid or an amorphized system, as the resulting disorder exhibits considerable short and medium-range order. To cast some light on this issue, now we study the topologies of the radiation-damaged system and a corresponding system equilibrated at a high temperature. We want to see, if the two systems, both having the same temperature, but one being equilibrated at that given temperature, while the other having that temperature due to cascade, have similar topologies or not.

Fig. 5.19 and 5.20 show a detailed comparison of the systems under disorder, and their analysis by RDF and ring analysis respectively. The common strategy is, for a given material, we consider two samples. (1) Cascade peak: The system at time (t_{peak}) when the cascade is at its peak. We note the temperature of the cascade region at this time, as $Temp_{(peak)}$; (2) Heated sample: the system equilibrated at $Temp_{(peak)}$ by heating.

In all the three figures (5.19a, 5.19b and 5.19c), we can see that RDF plots for a radiation damaged system, and a system equilibrated at an equivalent high temperature ($Temp_{(peak)}$) are almost exactly similar and one may conclude from this that the radiation damaged system behaves like a melt in all of these systems. However, ring analysis shows a more detailed picture, and we find, it can actually discern the difference between a radiation damaged and a melted system.

117
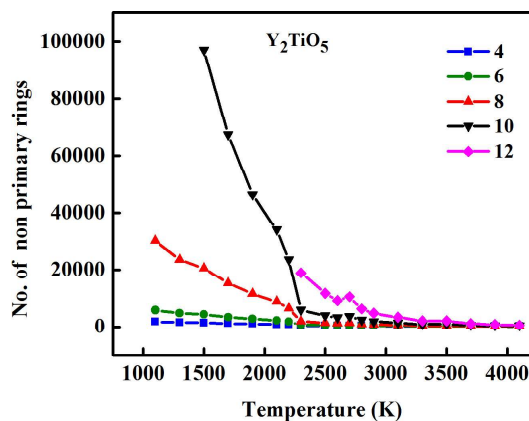
Figure 5.18 – Variation of the number of non-primary rings with temperature in Y_2TiO_5.

paths in the system, with respect to temperature, as shown in Fig. 5.18. These closed paths are the rings which don't have any constraint to be the shortest path [14], and in this discussion, we simply call them 'non-primary' (NP) rings. As can be seen from Fig. 5.18, as the temperature increases, all the NP rings (lower as well as higher order rings) present in the system gradually decrease and eventually vanish after the MP. This shows, that in reality, all the topological order in these systems gets diminished as the temperature is increased and no new long-range order emerges. The effect of increasing higher order rings in the case of primary rings in the current systems is an artifact which comes from the criteria of certifying a ring as a primary ring. As temperature increases, the originally present lower order rings break up, and some higher order rings get qualified as primary rings (as the previous short-cuts don't exist now), and hence, it gives a false inference, as if these rings have suddenly "appeared" as the temperature has increased. Similarly, it was seen that in the radiation damaged system also, no new long-range order emerges. The reason we have not taken NP rings for our analysis is, for crystalline systems, the program is unable to count the higher order rings properly, as the number of these rings becomes quite large. In Fig. 5.18, we have plotted the rings for temperatures 1000 K onwards, as at the temperatures lower than this, higher order NP rings could not be counted properly due to the system still maintaining some crystalline order. Thus, we conclude, unlike zirconolite, these systems do not show the emergence of any new long-range order upon heating.

116
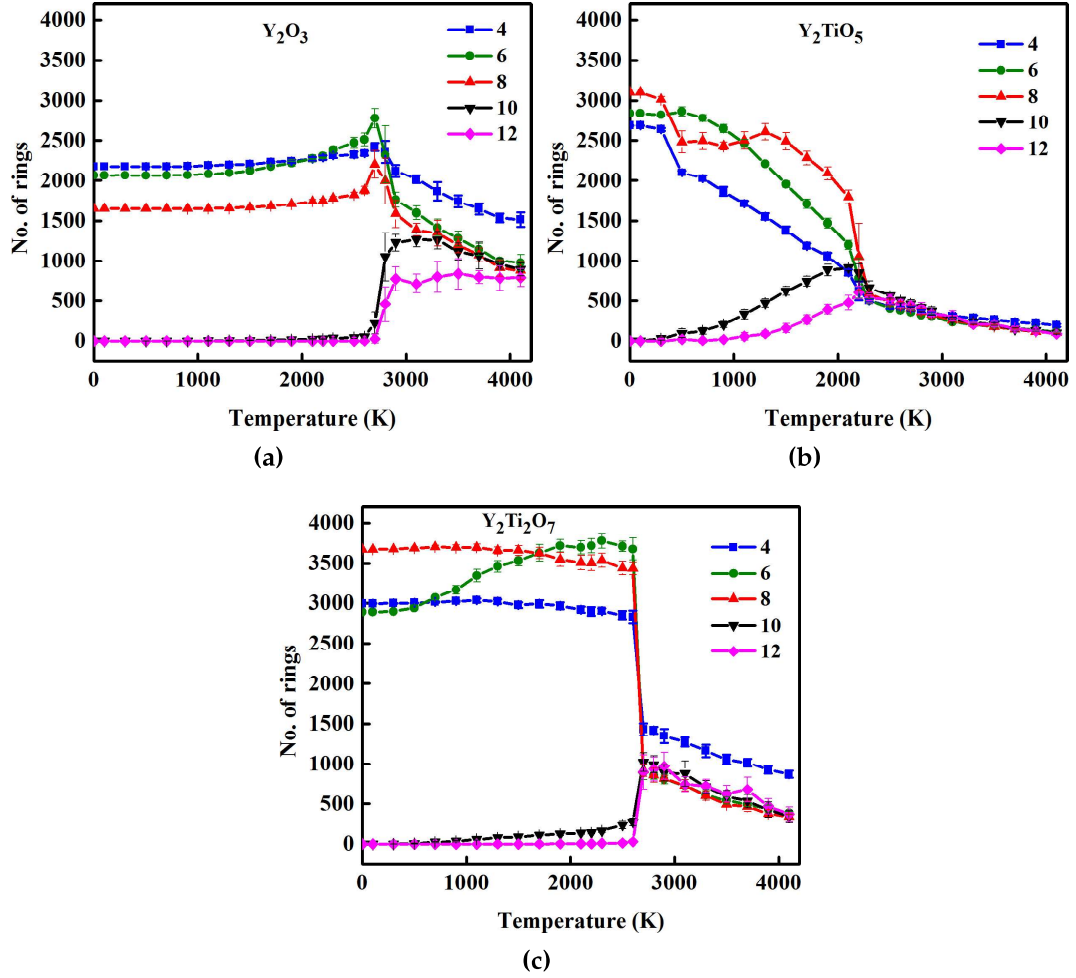
Figure 5.17 – Variation of the number of rings of all orders, with temperature: (5.17a) Y_2O_3; (5.17b) Y_2TiO_5; (5.17c) $Y_2Ti_2O_7$. Notice higher order rings are seen to increase as temperature is increased. In Fig. 5.18, we show this does not indicate any new long-range order emerging in the Y-Ti-O systems equilibrtaed at very high temperatures.

creases, the numbers of originally present rings (4, 6 and 8 order) start decreasing, while higher order rings, originally absent in the system, start rising in number. Does that mean a new topological order has emerged in the Y-Ti-O systems when they are heated? In fact, in a similar study on zirconolite, Foxhall *et. al* found that an increase in the temperature resulted in a reduction in the number of lower-order rings that were initially present in the crystalline zirconolite, but new higher order rings were formed, indicating emergence of a new order in the system [15].

Now we check, whether Y-Ti-O systems actually show a behavior similar to that shown by zirconolite, i.e, the emergence of a new long-range order when heated to a high temperature. For this, we analyze the variation of the number of all closed

Fig. 5.16a shows a comparison of RDF, while Fig. 5.16b shows a comparison of the number of rings versus ring-order for two different temperatures. While RDF shows almost the same behavior at the two temperatures, ring analysis shows a clear difference. Rings of all orders decrease in number at the higher temperature. This result shows, that at temperature 3100 K, although the number of all the rings gets diminished, still some rings survive and hence the topological order sustains to a certain degree. However, when the temperature is further increased to 4100 K, the remaining order in the system also vanishes, resulting in most of the rings getting destroyed.

The reason for ring-analysis being better able to differentiate between the disorder at two different temperatures, as compared to RDF, can be understood from the following argument. Suppose, at a certain temperature, the cation polyhedra remain intact, but there arises a random disorder in their relative orientations. This disorder will lead to the diminishing of the peaks in the RDF plot, but in rings analysis, since one analyzes only the connectivities, regardless of the relative orientations, it may be found that the connectivities are not completely lost. Now, if the system is equilibrated at a higher temperature, RDF will still show the diminished peaks, while ring-analysis will show the loss of the remaining connectivites too, thereby indicating, the new system is even more disordered than the system equilibrated at a lower temperature.

Now we discuss, how the topology of the systems varies as the temperature is increased. Fig. 5.17 shows the effect of temperature on the number of rings of various orders in the systems. It should be noticed that the rings of all orders suffer a sharp transition at around MP of the respective crystal systems, after which the topological order almost diminishes. In the case of Y_2TiO_5, it can be seen that before MP is reached, some rings start getting broken. This is due to the higher diffusion coefficient of oxygen in the case of Y_2TiO_5, as can be seen from Fig. 4.8a. Since the oxygen atoms make the connections between cation polyhedra, their diffusion will lead to the breaking of rings.

One peculiar thing to notice is, in all the three systems, as the temperature in-

figuration although defects may not have formed in reality. In this scenario, the study of the topology of the cascade affected region may provide some useful insights. Thus, now we use ring analysis, which is a topology based tool to analyze the disorder in the systems. The details of the methodology and the definitions we have used to characterize the rings can be seen in section 2.3.2. The cascade runs in the subsequent analyses correspond to 8 keV PKA, with the initial equilibration temperature of the lattice as 300 K.

5.6.1 Ring analysis in systems equilibrated at high temperatures

First we study the effect of temperature on the topology of the systems. We start with applying ring analysis and RDF analysis on a system equilibrated at different temperatures and see if ring analysis can provide some information which can not be obtained from the usual tools like RDF to analyze the order in systems. For this, a system (Y_2TiO_5) is equilibrated at two different high temperatures, 3100 K and 4100 K, which are both beyond the MP of Y_2TiO_5. The idea is, although both the systems would be highly disordered, the one having higher temperature may show higher disorder than the other, and this must get reflected in the topology of the system. The following discussion is similar for all the three Y-Ti-O systems, hence, for a representation, we only discuss the case of Y_2TiO_5 in this part.
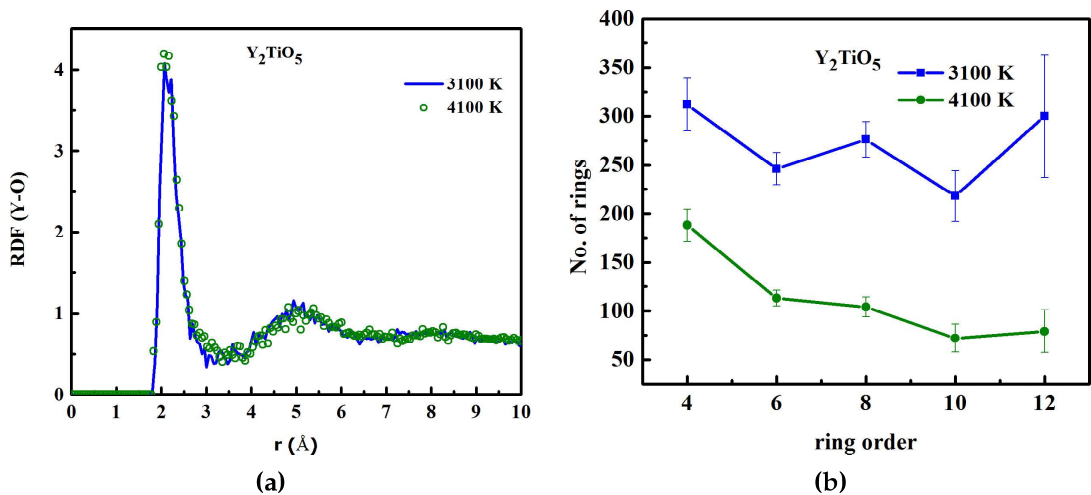
Figure 5.16 – Y_2TiO_5 crystal system, equilibrated at temperature 3100 K and 4100 K, compared by (5.16a) Partial RDF of Y-O bond and (5.16b) total number of rings vs order of ring.
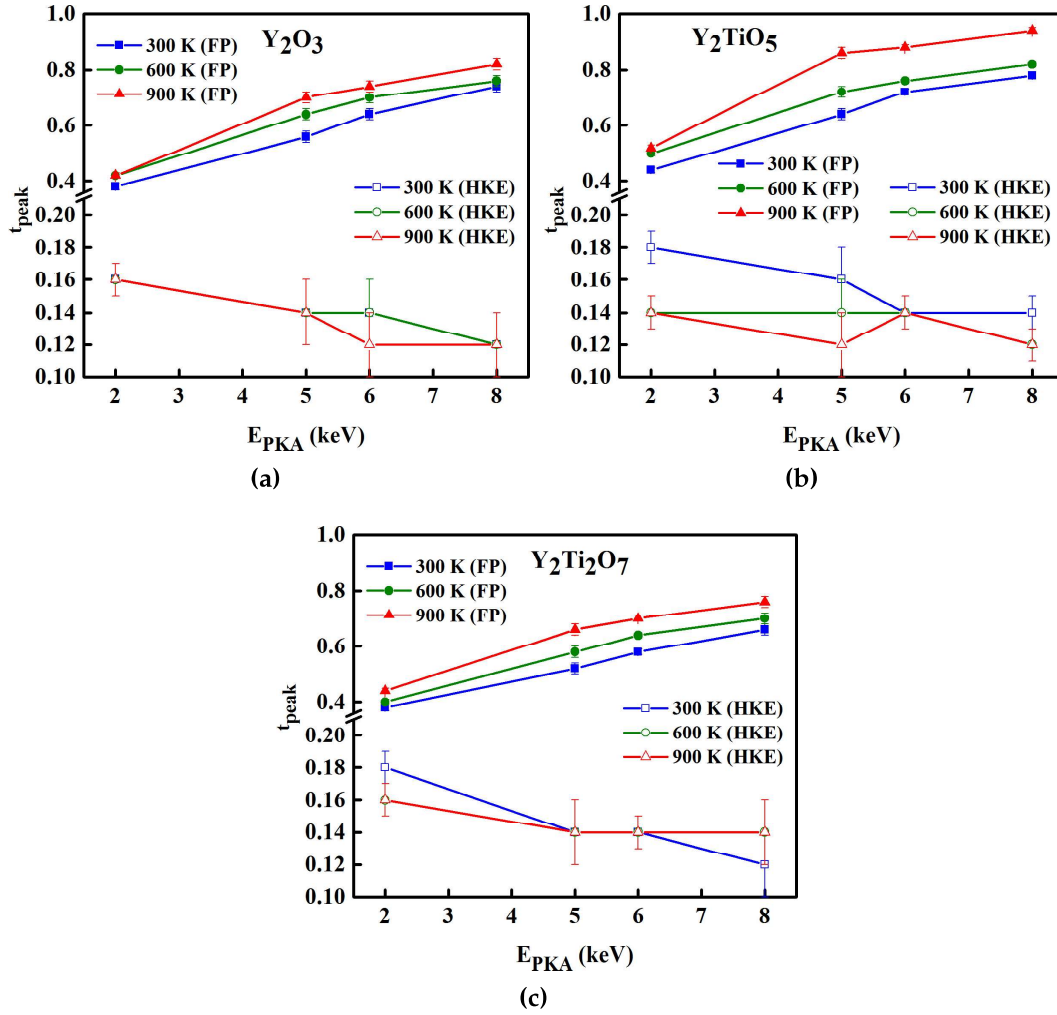
Figure 5.15 – Time to reach maximum number of Frenkel pairs (t_{peak}) and maximum number of HKE atoms $t_{peak}(HKE)$ vs E_{PKA} for different initial equilibrium temperatures of the crystals: (5.15a) Y_2O_3; (5.15b) Y_2TiO_5; (5.15c) $Y_2Ti_2O_7$.

5.6 Topological analysis of disordered systems

Network structures are characterized by a measure of directed bonding and connectivities. Crystalline networks, in addition, exhibit long-range translational periodicity. Irradiation causes the loss of all these network properties. The usual tools to analyze disorder, which rely on comparing the damaged system with reference structures may not give a complete picture when analyzing structures undergoing highly energetic situations such as radiation damage [53]. The penetration of ion and collapse of cascade region causes the elastic waves [155] which can lead to a a shift of atomic planes and, accordingly, shift of atoms from the reference con-
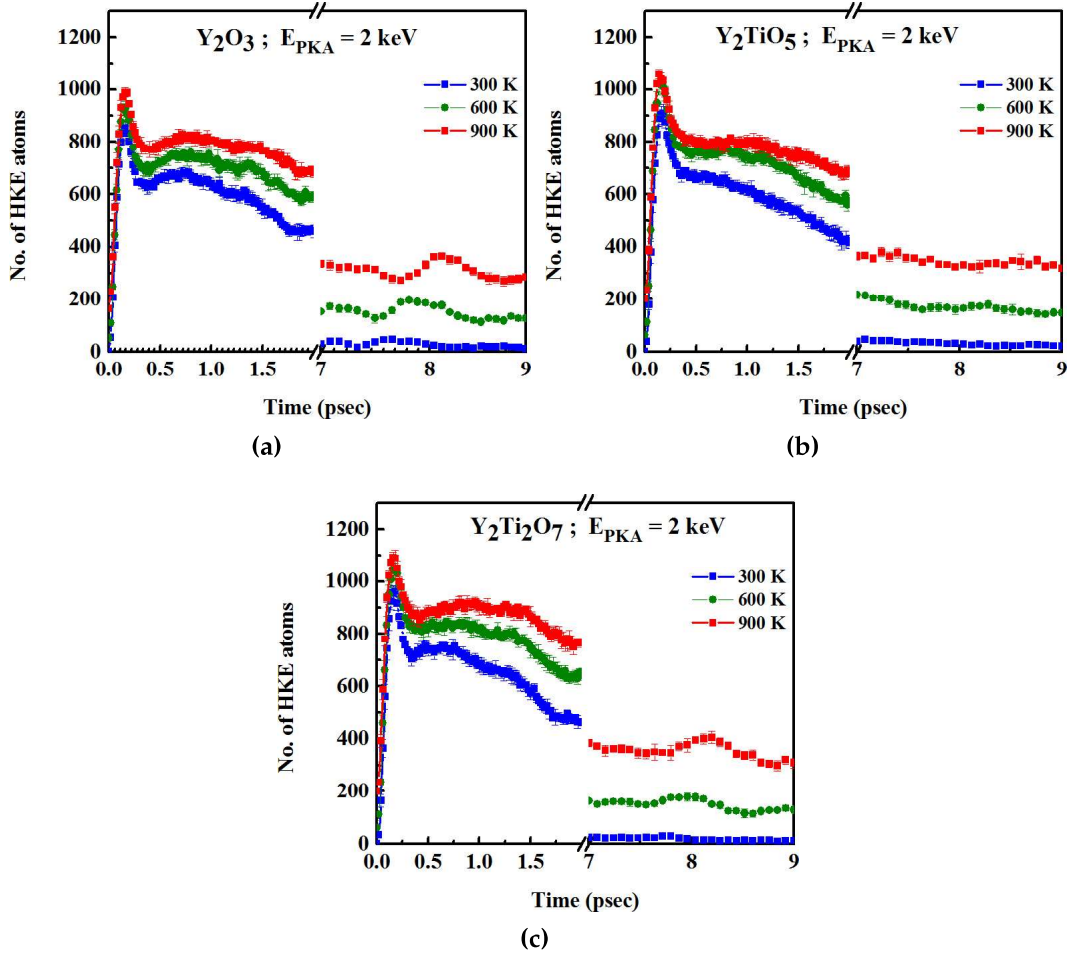
Figure 5.14 – Variation of HKE atoms with time for different initial temperatures (T) of the crystals. E_{PKA}= 2 keV. (5.14a) Y_2O_3; (5.14b) Y_2TiO_5; (5.14c) $Y_2Ti_2O_7$.

spective peak values in all the three systems. As can be seen, the peak number of HKE atoms always reaches before the peak number for defects (at t_{peak}) arrives. Moreover, as E_{PKA} increases, while t_{peak} increases at a substantial rate, $t_{peak}(HKE)$ actually decreases with a smaller rate. One thing this behaviour may indicate towards is, that the predominant mechanism for defect production is via ballistic collisions, rather than due to very high temperature arising because of the cascade, as the peak number of HKE atoms signifies that the maximum number of atoms have acquired a high kinetic energy (higher than the corresponding reference temperature), but still they have not left their lattice sites, and have not become point defects.

111
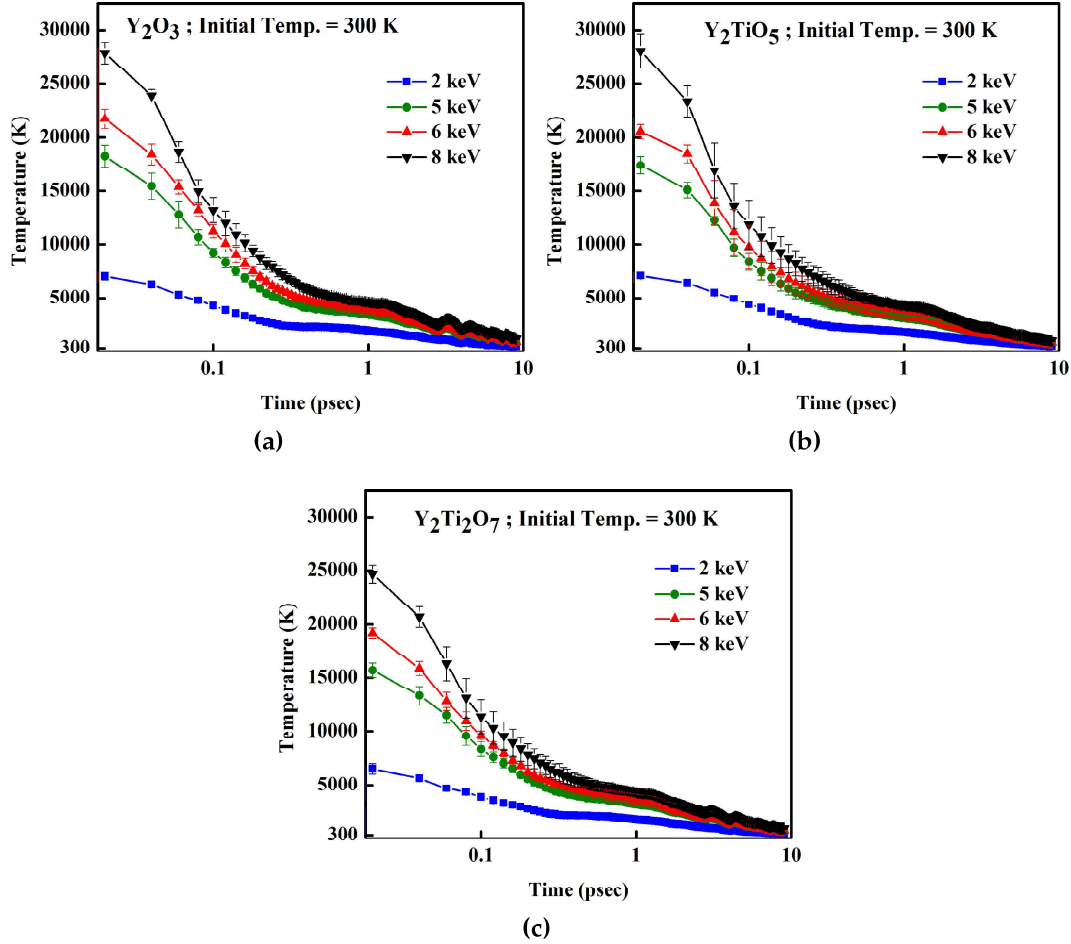
Figure 5.13 – Variation of temperature with respect to time for different E_{PKA}. (5.13a) Y_2O_3; (5.13b) Y_2TiO_5; (5.13c) $Y_2Ti_2O_7$.

($\sim$2000 K [25]). MP of Y_2TiO_5 is used just for a reference as it is the lowest among the three systems, and we want to compare all the three structures using the same reference. Fig. 5.14 shows the variation of HKE atoms with time for different initial temperatures of the lattice for all the three systems. The variation of HKE has the similar behavior as that for FPs, with a typical rising curve, which starts decaying after reaching its peak. Further, it can be seen that the variation of HKE atoms with time is almost similar in all the three materials and the number of HKE atoms do not change much with the increase in the initial temperature of the lattice. The interesting difference between the FPs and HKE atoms comes from the study of the variation of the time $t_{peak}(HKE)$ (the time when the peak number of HKE atoms is reached) with the PKA energy.

Fig. 5.15 compares the time it takes for HKE atoms and FP to reach their re-

along with a "difference" curve depicting the difference of O partial RDF for the damaged and the crystalline systems. If a new order has emerged in the system, the peaks in the RDF will get shifted leading to sharp positive peaks in the difference curve. But, as can be seen from Fig. 5.12, in all the cases the difference plot does not have any prominent new positive peaks, thereby indicating the absence of any newly emerged crystalline ordered configuration of O atoms. Thus, we can say that in all the three cases, anion disordering to alternate crystalline positions is not seen. Since a substantial number of c-c antisites are produced in $Y_2Ti_2O_7$ without a considerable anion disordering, we can say that $Y_2Ti_2O_7$ has undergone an incomplete order-disorder transition.

However, relaxed calculations on coupled cation-antisite and Frenkel-pair defects show that cation-antisite reactions likely drive the oxygen Frenkel pair defect formation process [154]. Since cation antisite disorder precedes oxygen disorder [154], thus survival of a considerable number of cation antisites in $Y_2Ti_2O_7$ may indicate towards their proclivity for an order-disorder transition, leading to defect fluorite structure. It seems, higher PKA energies may lead to a complete order-disorder transition.

5.5.4 Temperature distribution in cascade

Now we study the way temperature is distributed in the cascade region. Fig. 5.13 shows the variation of temperature with time in the cascade region, for different PKA energies in all the three systems. Initially, there is a very high temperature due to cascade, but it gradually decays to the initial equilibration temperature of the lattice by the end of the simulation time. Any difference in the temperature pattern for the three systems is not clearly discernible and it seems the flow of heat from all the three systems should be quite similar for the simulation conditions taken in this study. Further, the initial temperature of the crystal also does not have any visible effect on the temperature distribution.

To explore more deeply into the way the heat energy is distributed in the cascades, we define "HKE" (High kinetic energy) atoms as atoms having kinetic energy in excess to the energy corresponding to the melting point (MP) of Y_2TiO_5
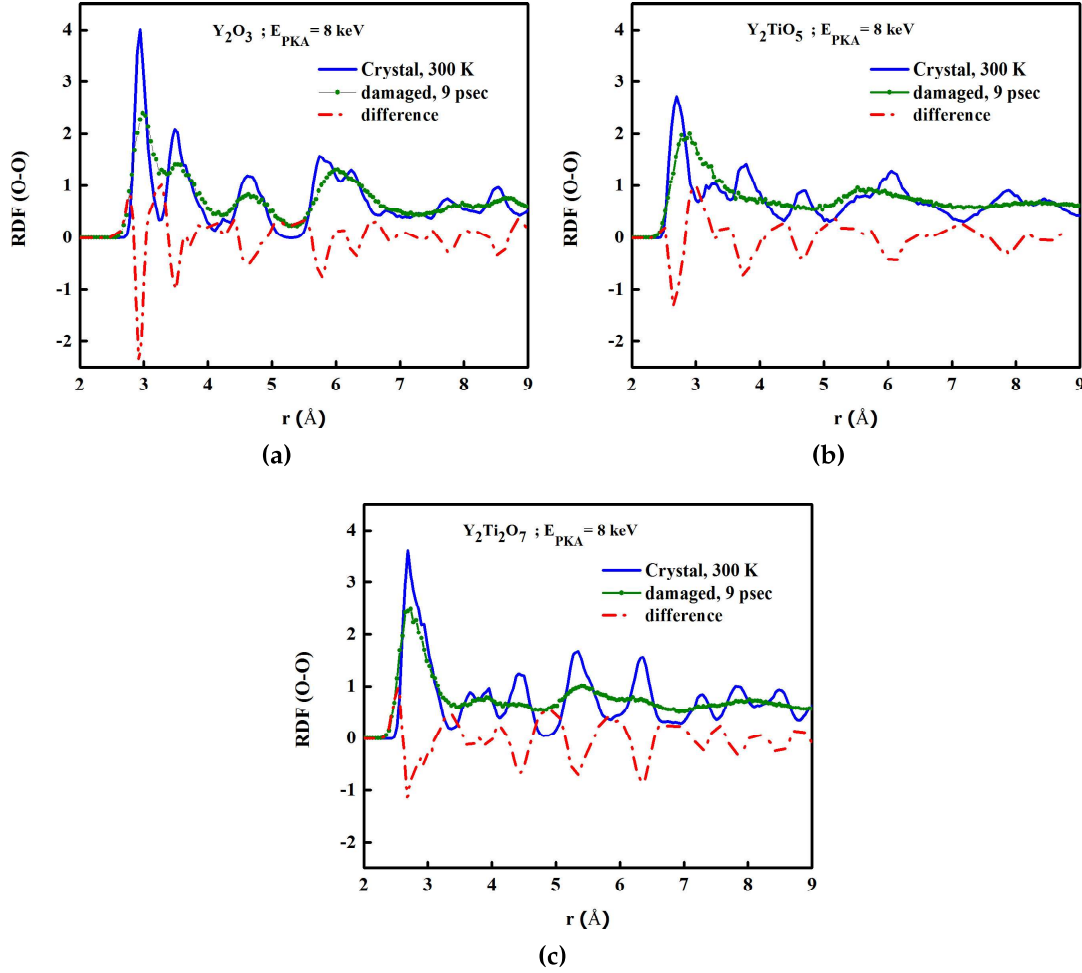
Figure 5.12 – Comparison between the partial RDF of O atoms for the crystalline system (300K) and radiation damaged system at the end of simulation time. For a better comparison, a "difference" curve (Red curve), depicting the difference of O partial RDF for the damaged and the crystalline systems is also plotted. (5.12a) Y_2O_3; (5.12b) Y_2TiO_5; (5.12c) $Y_2Ti_2O_7$.

tion of c-c antisites, particularly in $Y_2Ti_2O_7$ may hint towards an order-disorder transition to defect fluorite structure but to confirm it, we need to see the anion disordering. Since the anion disordering in order-disorder transition places oxygen in well defined crystalline positions, the partial RDF of the oxygen atoms in the corresponding disordered system may reflect this in the form of the emergence of a new crystalline order. Thus, now we study the partial RDF of oxygen atoms for all the three systems to see if this kind of behavior can be seen in any of these materials.

Fig. 5.12c shows a comparison between the partial RDF of O atoms for the crystalline system (300K) and radiation damaged system at the end of simulation time,
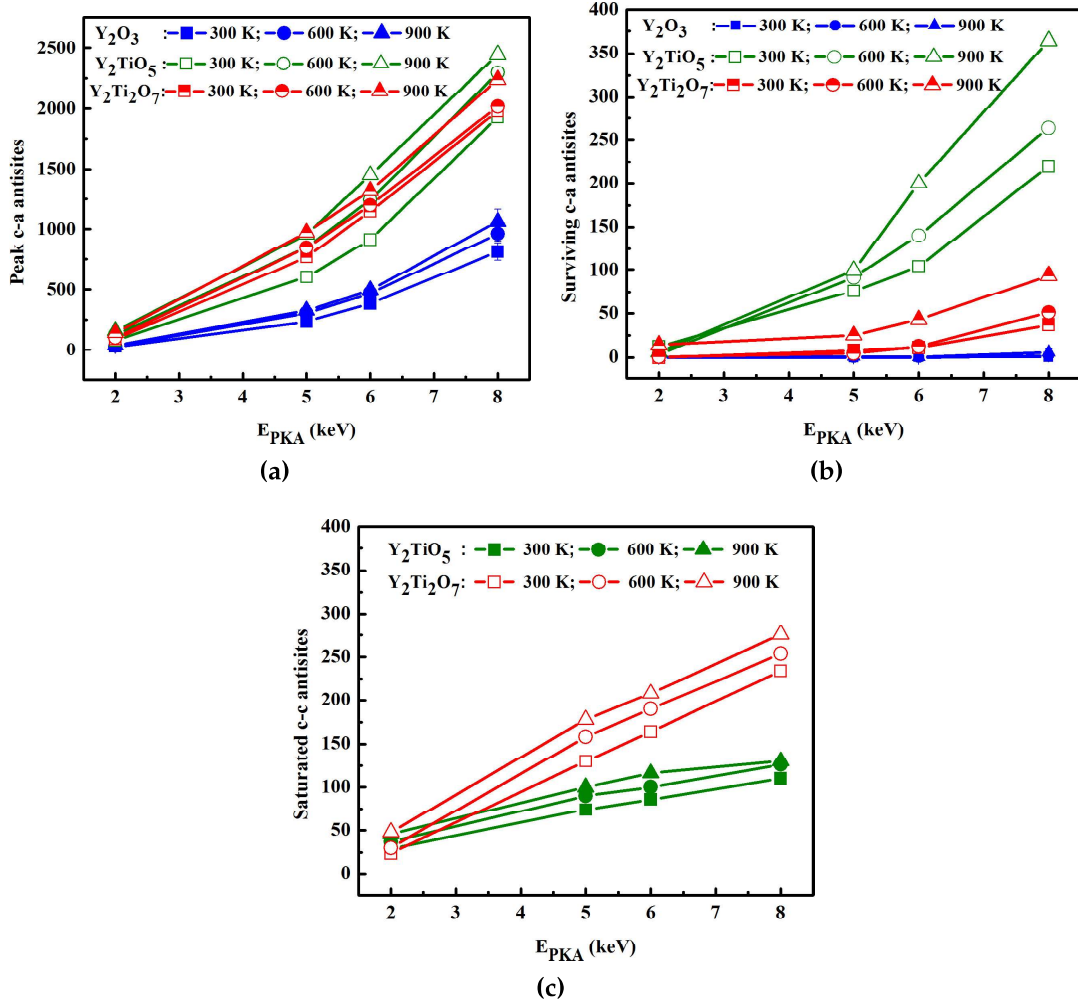
Figure 5.11 – No. of antisites vs E_{PKA} for different initial crystal temperature (T); (5.11a) Peak number of anion-cation (a-c) antisites; (5.11b) Survived number of anion-cation (a-c) antisites; (5.11c) Number of cation-cation antisites (c-c). Notice the different scale for Y axis in the case of Fig. 5.11a

the study of FPs too, it is seen that in Y_2O_3, the least number of FPs survive by the end of the cascade. Thus, from these point defect analyses, it seems Y_2O_3 is having a very resilient structure which resists damage.

Fig. 5.11c shows that a large number of c-c antisites survive in the case of $Y_2Ti_2O_7$ as compared to that in Y_2TiO_5. This points towards the ease of cation disorder in the case of $Y_2Ti_2O_7$ and may indicate towards its higher resistance to amorphization [27] as compared to Y_2TiO_5 .

As mentioned earlier, in pyrochlores, irradiation causes an order-disorder transition, involving cation antisites and anion disordering by oxygen migration from $48f$, $8b$ sites to vacant $8a$ sites leading to defect fluorite structure [27]. The forma-

before getting quickly annihilated and surviving in a considerably small number by the end. This is easily understandable, as cations and anions are neighboring atoms and immediately replace each other at the time of cascade, while fail to survive in a considerable number due to the predominantly ionic nature of these systems [145]. It should be noticed that a negligible number of a-c antisites survive in Y_2O_3 and $Y_2Ti_2O_7$ at the end of the simulation time. Further, in Y_2O_3, substantially lesser number of antisites are produced as compared to Y_2TiO_5 and $Y_2Ti_2O_7$.

An interesting aspect seen from Fig. 5.10b and 5.10c is the delayed production and the subsequent saturation of the cation-cation (c-c) antisites (simply called as cation antisites) in Y_2TiO_5 and $Y_2Ti_2O_7$. In the case of $Y_2Ti_2O_7$, cation antisites eventually surpass the number of surviving a-c antisites, while in Y_2TiO_5 too, c-c antisites increase but by the end of the cascade, both c-c and a-c antisites are almost similar in number. The ease of survival of c-c antisites as compared to a-c antisites can be explained as the cation antisite formation energy is much smaller than a-c antisite formation energy [27, 72] in $Y_2Ti_2O_7$, and the antisite pair formation energies calculated for both the systems in our calculations also showed that c-c antisite pair formation energy is smaller than a-c antisite pair formation energy (see Table. 4.3). However, the delayed production and the apparent saturation of cation antisites is a unique feature. The apparent survival of a-c antisites in Y_2TiO_5 may be due to the small time of simulation, and they may get annihilated in longer time simulations.

Fig. 5.11 shows the variation of the peak number of a-c antisites (Fig. 5.11a), the survived number of a-c antisites (Fig. 5.11b) and the survived (in this case, saturated) number of c-c antisites (Fig. 5.11c) with respect to the PKA energy (E_{PKA}) and at different initial temperatures (T) for all the three systems. It can be seen that effect of the initial equilibration temperature is not very prominent for these systems, except for Y_2TiO_5, which shows some increase in the survived number of a-c antisites as the initial temperature of the lattice increases. Further, for all the cases, as E_{PKA} increases, the measured quantity increases, except for Y_2O_3, where the survived number of antisites are almost negligible even for the 8 keV case. In

oxygen migration from $48f$, $8b$ sites to vacant $8a$ sites leading to a defect fluorite structure (For instance, see the study by Lian *et. al* [27] of ion irradiation by 1 MeV Kr^+ on Ti pyrochlores at room temperature). The transition to defect fluorite structure has been used to explain their resistance to amorphization due to radiation damage [27]. To study similar effects, now we analyze antisites production and local structure using RDF of the systems when they undergo displacement cascades.
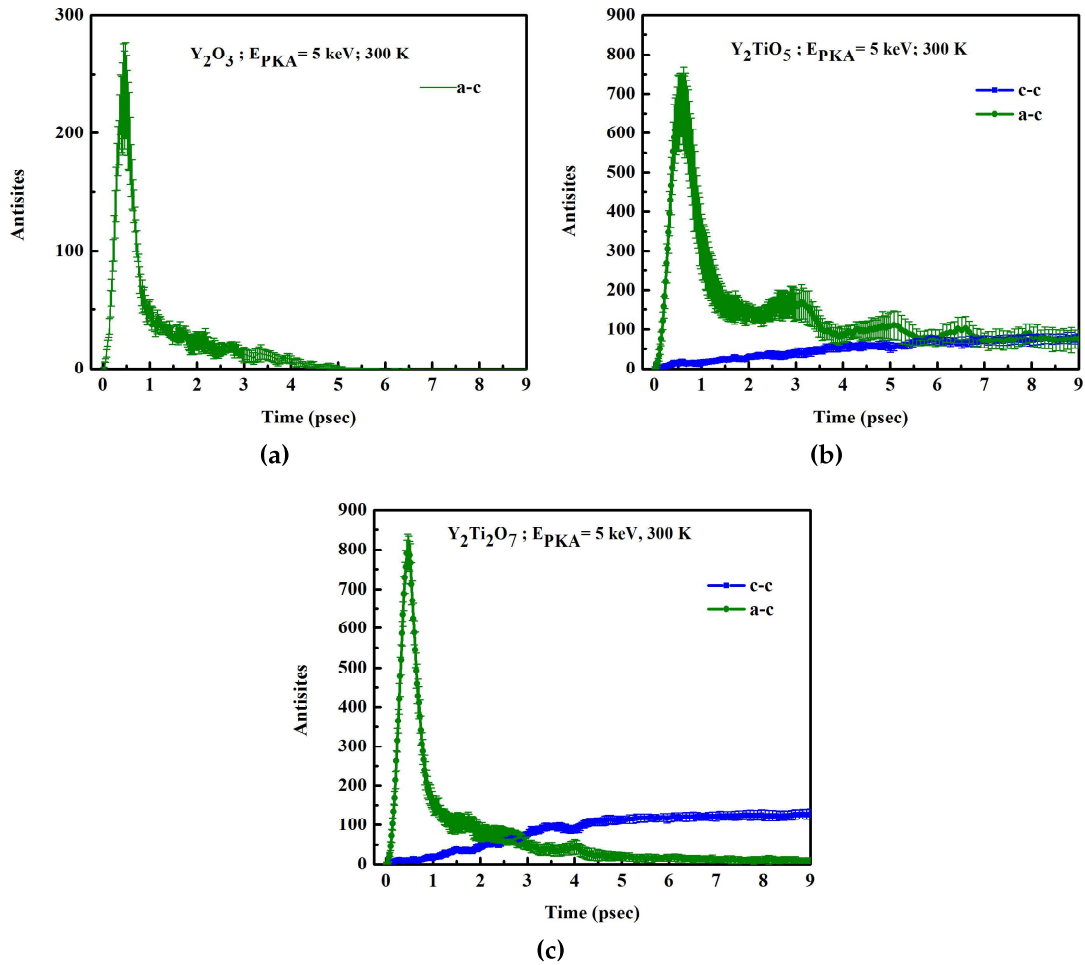
Figure 5.10 – No. of antisites vs time. Notation: a-c antisites: anion-cation antisite, describing interchange of an anion with a cation and vice versa; c-c antisites: cation-cation antisites (or simply, cation antisites) describing interchange of cations of different atomic species. (5.10a) Y_2O_3; (5.10b) Y_2TiO_5; (5.10c) $Y_2Ti_2O_7$. Initial crystal temperature, $T = 300$ K, $E_{PKA} = 5$ keV. Notice the different scale for Y axis in the case of Y_2O_3.

Fig. 5.10 and 5.11 show the results obtained from the study of antisite defects in all the three materials. As seen from Fig. 5.10, for all the three systems, the anion-cation (a-c) antisites increase substantially during the initial stages of the cascade

increases. The increase in MSD with PKA energy does not differ largely among the three systems, but for Y_2TiO_5, at $E_{PKA} = 8$ keV, the MSD is comparatively higher than that for Y_2O_3 and $Y_2Ti_2O_7$. A similar trend is seen at all the temperatures ($T = 600$ K, 900 K). The reason for MSD not varying much with the initial temperature of the lattice should be because of the fact, that the contribution of temperature in the ballistic diffusion would be negligible as compared to that of the ballistic motion.
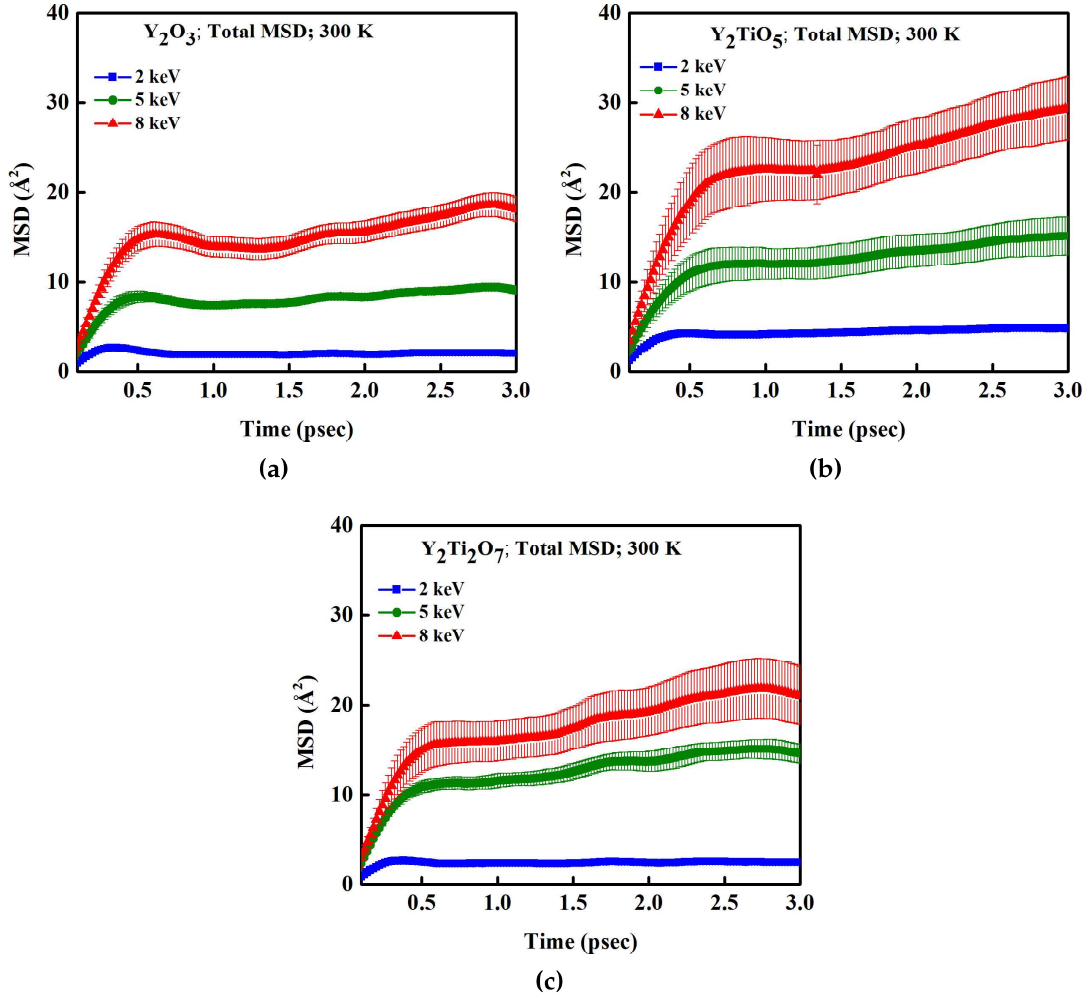
Figure 5.9 – Comparison of the variation of total MSD with time for different E_{PKA} and for $T = 300$ K. (5.9a) Y aoms; (5.9b) O atoms; (5.9c) Ti atoms.

5.5.3 Study of antisites and oxygen disorder

The ease for cation disorder and closeness to fluorite structure are some of the factors which have been used to explain the high amorphization resistance of ternary and binary oxides [51, 52]. It is seen, that in pyrochlores, irradiation causes an order-disorder transition, involving cation antisites and anion disordering by

5.5.2 Ballistic diffusion of atoms in the cascade region

A study of mean square displacement of the ballistically moving atoms in the cascade region sheds light on the cascade characteristics from a different point of view. The MSD of individual atomic species in different systems is shown in Fig. 5.8. It is seen that Y atoms have a comparable MSD in all the three systems, but O atoms have a much higher ballistic diffusion in the case of Y_2TiO_5 as compared to Y_2O_3 and $Y_2Ti_2O_7$. Further, Ti atoms also have a higher ballistic diffusion in the case of Y_2TiO_5 as compared to $Y_2Ti_2O_7$.
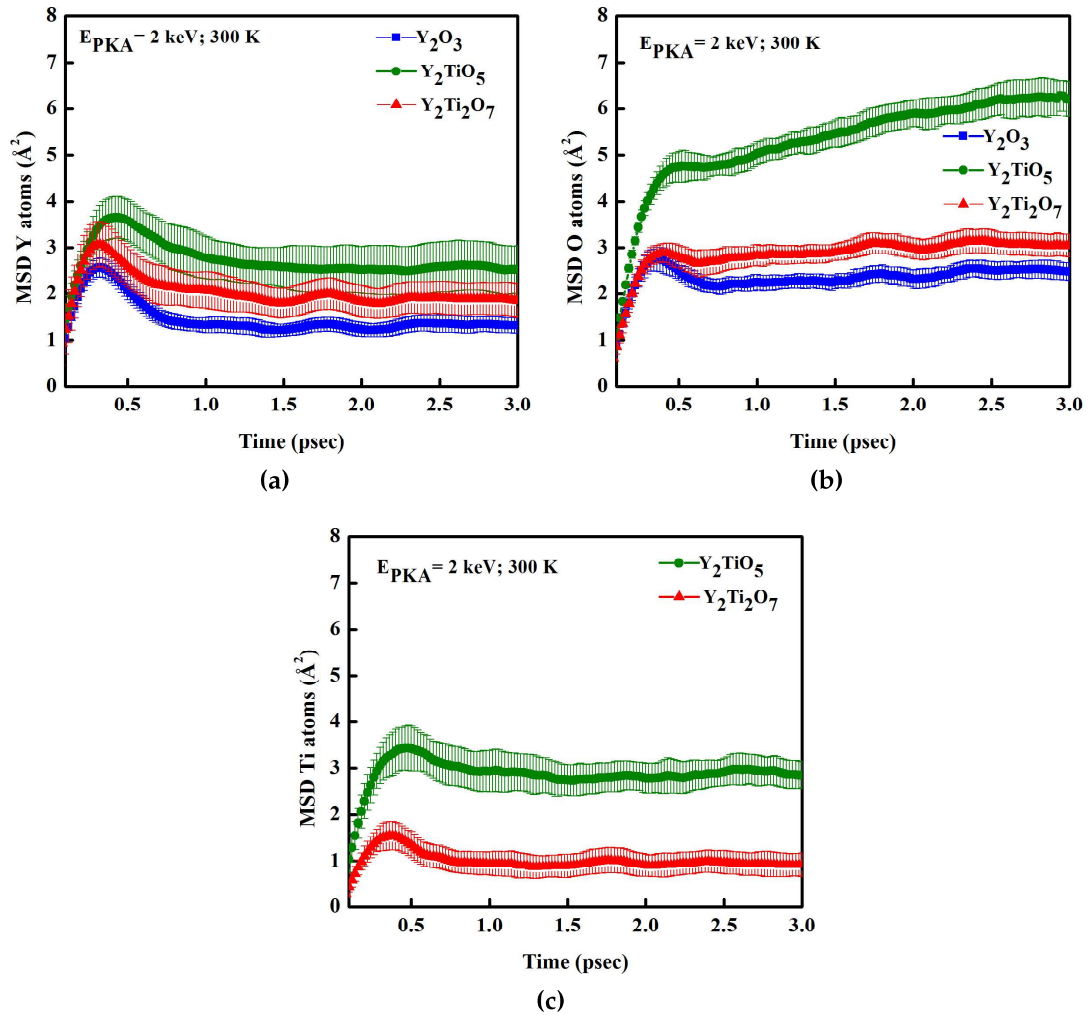
Figure 5.8 – Comparison of the MSD of individual atomic species in different compounds. E_{PKA} = 2 keV and T = 300 K. (5.8a) Y aoms; (5.8b) O atoms; (5.8c) Ti atoms.

Fig. 5.9 shows the variation of the total MSD with time in a system for different E_{PKA}. Evidently, as PKA energy increases, the ballistic diffusion of all the atoms

103

derstood, as with an increase in the temperature, threshold energy to displace an atom from its lattice site will decrease and thus, more number of defects would be produced.

Fig. 5.7 shows that the number of defects that ultimately survive is far less in Y_2O_3 as compared to Y_2TiO_5 and $Y_2Ti_2O_7$. Y_2TiO_5 has the maximum number of survived defects by the end of the simulation time. The variation of the number of surviving FPs is linear for $Y_2Ti_2O_7$, but it is not strictly linear in Y_2O_3 (the linearity is only up to 5 keV energy, as also was seen in section-3.4.2) and Y_2TiO_5, with a considerably larger number of FPs surviving at a higher energy, than that expected from a linear relationship. Also, it is observed that for all the three systems, the surviving number of defects does not decrease as the initial temperature of the system increases, which is in contrast to metals [61, 153]. This points towards comparatively lower diffusion in oxide materials which makes the recombination process in them sluggish as compared to metals. A longer simulation time is expected to show a lower number of FPs surviving as the initial temperature of the lattice is raised.
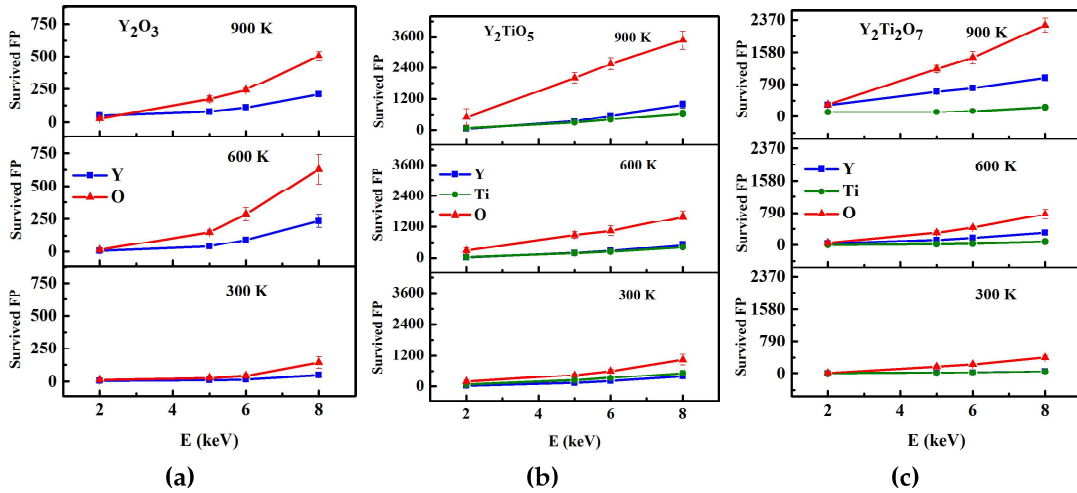
Figure 5.7 – Surviving number of Frenkel pairs of individual atomic species vs E_{PKA} for different initial crystal temperatures: (5.7a) Y_2O_3; (5.7b) Y_2TiO_5; (5.7c) $Y_2Ti_2O_7$. Notice the comparatively smaller scale for the Y axis in the case of Y_2O_3.
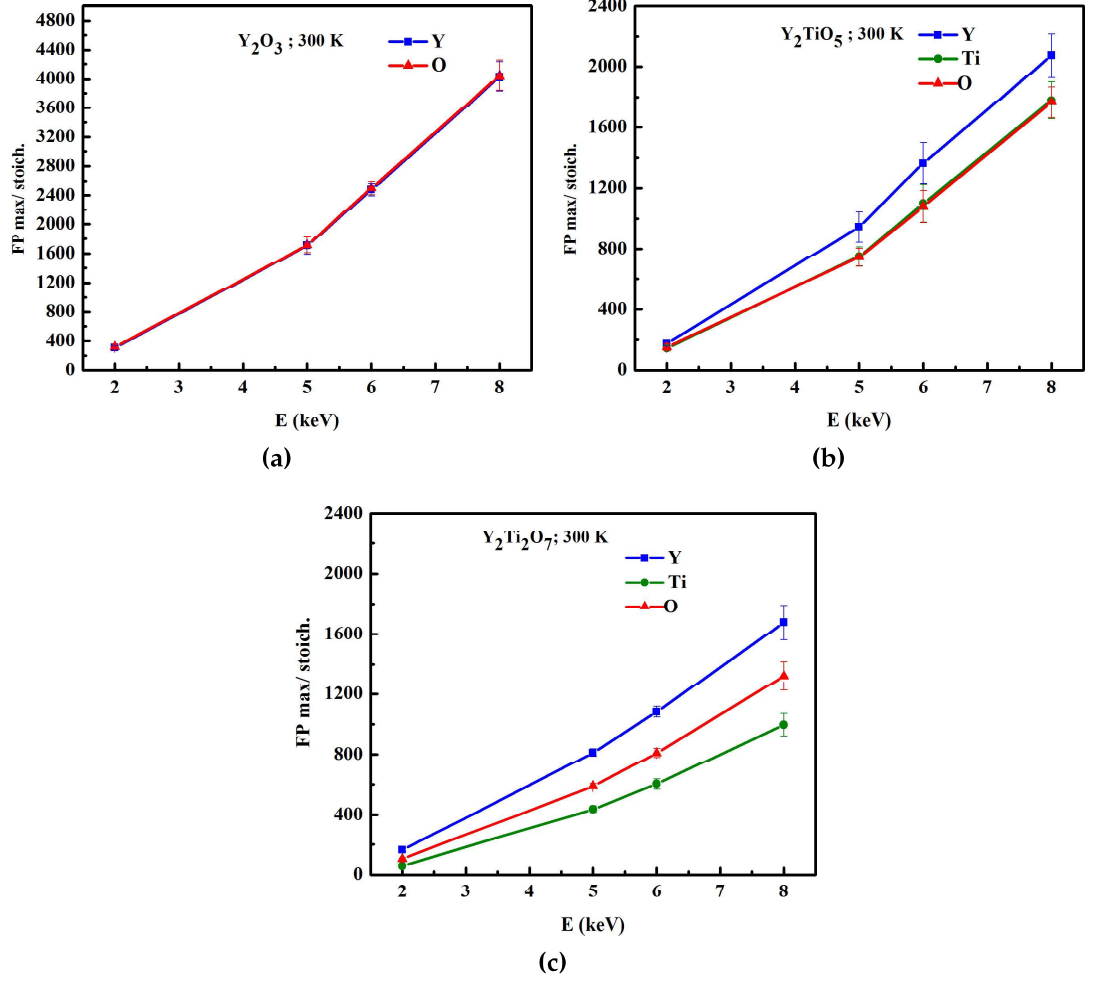
Figure 5.6 – Peak number of Frenkel pairs normalized by the relative stoichiometry vs E_{PKA}: (5.6a) Y_2O_3; (5.6b) Y_2TiO_5; (5.6c) $Y_2Ti_2O_7$.

tions (<100>, <110> and <111>), for cations and anions in $Y_2Ti_2O_7$ are ~35 eV and ~17 eV, respectively [76]. At lower energies, the number of normalized defects is almost similar for Y, Ti, and O, however, the difference increases as E_{PKA} increases, with normalized Y FPs produced in a larger number than normalized O FPs, followed by normalized Ti FPs.

The peak number of defects for all the three systems at all the initial temperatures and E_{PKA} are almost comparable. For all the three systems, the peak number of FPs varies linearly with E_{PKA}. This should be, since up to the time (t_{peak}) peak number of defects are generated, the cascade is basically governed by ballistic collisions, where the number of defects is proportional to the PKA energy. With increasing temperature, the peak number of defects also increases. This can be un-
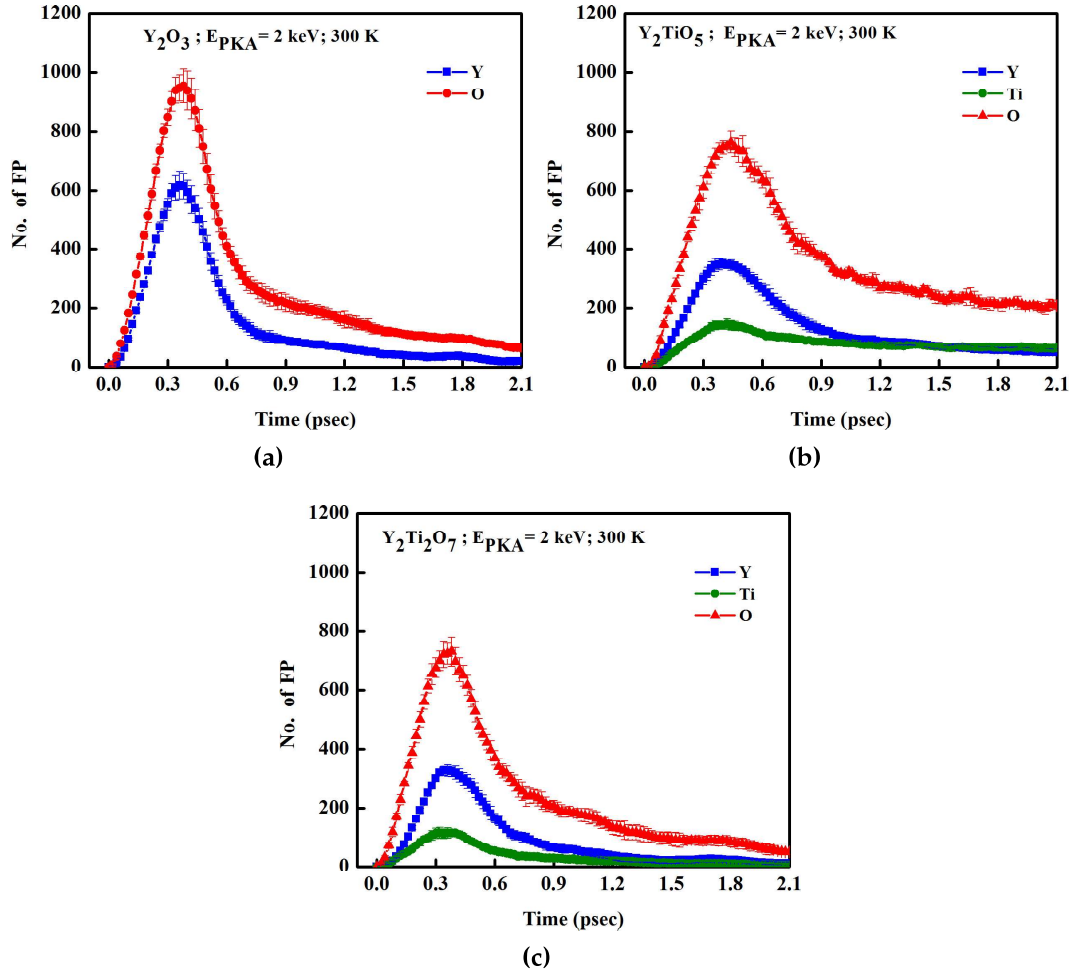
Figure 5.5 – Variation of the number of Frenkel pairs with time for (5.5a) Y_2O_3; (5.5b) Y_2TiO_5; (5.5c) $Y_2Ti_2O_7$; T = 300 K, E_{PKA}= 2 keV.

Fig. 5.6a, the normalized number of Y and O defects remain exactly equal at all the energies. The threshold displacement energy of Y and O atoms is equal in Y_2O_3, both being 57 eV [124]. Thus, in the case of Y_2O_3, we can say the production of the number of Y and O defects exactly follows the stoichiometry of the lattice.

In the case of Y_2TiO_5, as seen from Fig. 5.6b, the number of Ti and O normalized FPs are almost equal at all the energies, while Y FPs are produced in a larger number than that expected from the stoichiometry. The data for threshold displacement energy is not available for Y_2TiO_5, but this may indicate that the threshold displacement energy of Ti and O atoms must be almost similar in the case of Y_2TiO_5.

The corresponding plot in the case of $Y_2Ti_2O_7$ is shown in Fig. 5.6c. The threshold displacement energies measured along the three main crystallographic direc-

atoms are essentially two-body and can be approximated by the binary collision approximation. But, by the time of thermal spike, atoms lose their energy and it is at this stage, when interatomic potentials become very important and dictate the eventual rearrangement of atoms in the cascade-region. As an example, in the MD simulations of radiation damage in complex silicates and titanates, a formation of Si-O-Si and Ti-O-Ti bridges was observed and it was seen that their stability in the damaged state prevents atoms from regaining coherence with the crystalline lattice [11]. Thus in this section, we study the disorder in Y-Ti-O systems by displacement cascades as well as by equilibrating them at high temperatures. MD simulations are carried out for different PKA energies and initial temperatures of the lattice. To obtain good insight from different approaches, we employ point defect analysis using equivalent sphere method [30], radial distribution function (RDF) as well as ring analysis [14] to analyze the damage in the systems.

5.5.1 Study of Frenkel pairs

Displacement cascades commence with the initiation of a highly energetic primary knock-on atom (PKA) which collides with other atoms of the lattice and a subsequent chain of collisions between atoms produces point defects in the target material. Initially, a large number of point defects are produced, but due to recombination, only a fraction of them eventually survive. This can be seen from Fig. 5.5, which shows the variation of the number of Frenkel pair defects with time in displacement cascades in Y-Ti-O systems for a 2 keV PKA, at an initial temperature 300 K of the crystal. This figure represents the general trend for all the different cases considered in this study. Cascade gets subsided by $\sim$2 psec in all the cases.

The general trend for all the systems is, the number of oxygen FPs is always higher than the number of cation FPs. To study if the difference arises due to the inherent stoichiometry of the lattices, in Fig. 5.6, we plot the peak number of FPs of all the different atomic species, divided by the stoichiometry of the corresponding lattice. For example, the numbers of Y, Ti and O FPs in $Y_2Ti_2O_7$ are divided by 2, 2 and 7 respectively. The trend seen at 300 K does not differ from the trends seen at other temperatures, thus here we show only the case of 300 K. In Y_2O_3, as seen in

in energy as compared to Y_2O_3 and Y_2TiO_5, indicating a better amorphization resistance for $Y_2Ti_2O_7$ as compared to Y_2O_3 and Y_2TiO_5, which seem to have almost a similar resistance to amorphization. Thus, this analysis, based on a completely different approach, compares well and validates the prediction obtained from the constraints analysis. Based on this analysis, we can say that in the case of Y-Ti-O systems, a prediction of amorphization resistance just by considering the structural aspects can also provide significant insights.

5.5 Simulation of dynamic disorder: by displacement cascades and by high temperatures

In both of the previous studies, the cation polyhedra are assumed to remain intact. But, in processes like displacement cascades, the polyhedra might completely get destroyed, or atoms may take completely different positions due to disorder. For example, SiC, having the structural degree of freedom, $f = -3$ [31] is a constrained system and thus, is predicted to be resistant to amorphization, but gets amorphized easily at 0.2 dpa irradiation dose [55]. It was proposed [135], that the possible antisite disorder generated within the displacement cascade, causes the Si and C sites to become indistinguishable. Due to this, the topology and the structural freedom of the disordered SiC corresponds to that of the Si structure ($f = 0$) and hence, it is amorphizable. However, this is an effect which involves dynamics of the system and cannot be envisaged by any of the aforementioned criteria for predicting amorphizabilities of materials. Thus, it seems, if a general mechanism for resistance to amorphization is to be identified, it should be microscopic and should be able to describe the atomic interactions and rearrangements.

If we employ MD simulations to analyze the dynamics of the disorder, we get two advantages: first, is the usage of interatomic potentials that can automatically model the contributions of short and long-range forces in the system, and second, since the dynamics can be investigated, one can track the reorganization of the lattice. In the ballistic phase of the displacement cascades, the interactions between
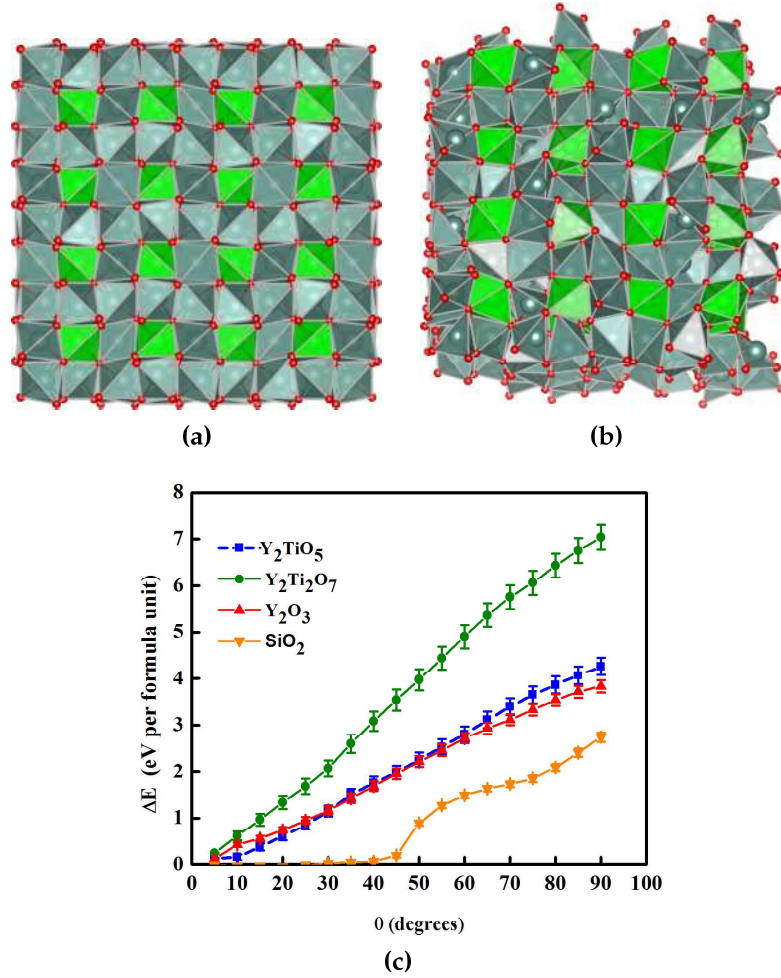
Figure 5.4 – (5.4a) Ideal crystal structure of Y_2O_3; (5.4b) Disordered system of Y_2O_3 corresponding to $\theta = 20°$; (5.4c) Strain energy per formula unit vs degree of distortion for $Y_2Ti_2O_7$, Y_2TiO_5, Y_2O_3 and SiO_2.

energies of the disordered system and the crystalline system by the number of formula units present in the system. To ensure statistically robust results, for each angle of rotation (θ), 1000 different random configurations of the same unit cell are generated and then molecular statics runs are performed on all the configurations.

Fig. 5.4c shows the change in energy per formula unit (ΔE) vs distortion angle (θ) for all the three systems along with SiO_2 (crystoballite). It can be seen that whilst SiO_2 shows a marginal change in its energy even when the lattice is quite distorted, Y-Ti-O systems show a substantial change in energy as disorder increases. This confirms the prediction obtained from the constraints analysis, that all the three Y-Ti-O crystals have a much higher resistance to amorphization than an amorphizable material like crystoballite. Further, $Y_2Ti_2O_7$ shows a larger change

97

Vertex	Connectivity (C)	Edge connected polyhedra	Corner shared
O_1	4	3 (All Y)	0
O_2	4	3 (1 Y , 2 Ti)	0
O_3	4	3 (1 Y, 2 Ti)	0
O_4	4	3 (1 Y, 2 Ti)	0
O_5	4	3 (1 Y, 2 Ti)	0
O_6	4	3 (1 Y, 2 Ti)	0
O_7	4	3 (1 Y, 2 Ti)	0
O_8	4	3 (All Y)	0

Table 5.5 – Connectivities of a YO8 polyhedron in the $Y_2Ti_2O_7$ lattice.

Vertex	Connectivity (C)	Edge connected polyhedra	Corner shared
O_1	4	2 (2 Y)	1 (Ti)
O_2	4	2 (2 Y)	1 (Ti)
O_3	4	2 (2 Y)	1 (Ti)
O_4	4	2 (2 Y)	1 (Ti)
O_5	4	2 (2 Y)	1 (Ti)
O_6	4	2 (2 Y)	1 (Ti)

Table 5.6 – Connectivities of a TiO6 polyhedron in the $Y_2Ti_2O_7$ lattice.

higher the resistance to amorphization. We compare Y_2O_3, Y_2TiO_5 and $Y_2Ti_2O_7$ crystals along with cristobalite SiO_2, which is a known amorphizable material having the structural degree of freedom, $f = 0$ [31].

We take a $2 \times 2 \times 2$ cell for Y_2O_3, $2 \times 6 \times 2$ cell for Y_2TiO_5, $2 \times 2 \times 2$ cell for $Y_2Ti_2O_7$ and a $3 \times 3 \times 3$ cell for SiO_2 for the energy minimization calculations using the conjugate gradient algorithm, as implemented in LAMMPS [13]. Interatomic potential for Y_2O_3 is from Belonoshko *et. al* [17], Tersoff potential is used for SiO_2[152], while for Y_2TiO_5 and $Y_2Ti_2O_7$, the in-house generated potentials are used. A given distortion to the lattice is described by a rotation angle θ along which all the individual polyhedra of the lattice are rotated along a randomly assigned axis passing through their respective centers. For a representation, Fig. 5.4a and 5.4b show the ideal structure of Y_2O_3 unit cell and it's disordered structure obtained after random rotations of the cation polyhedra. The disordered system, generated by randomly orienting the cation polyhedra is then relaxed using molecular statics until the energy convergence is obtained and then strain energy per formula unit deposited into the system is calculated by dividing the difference between the
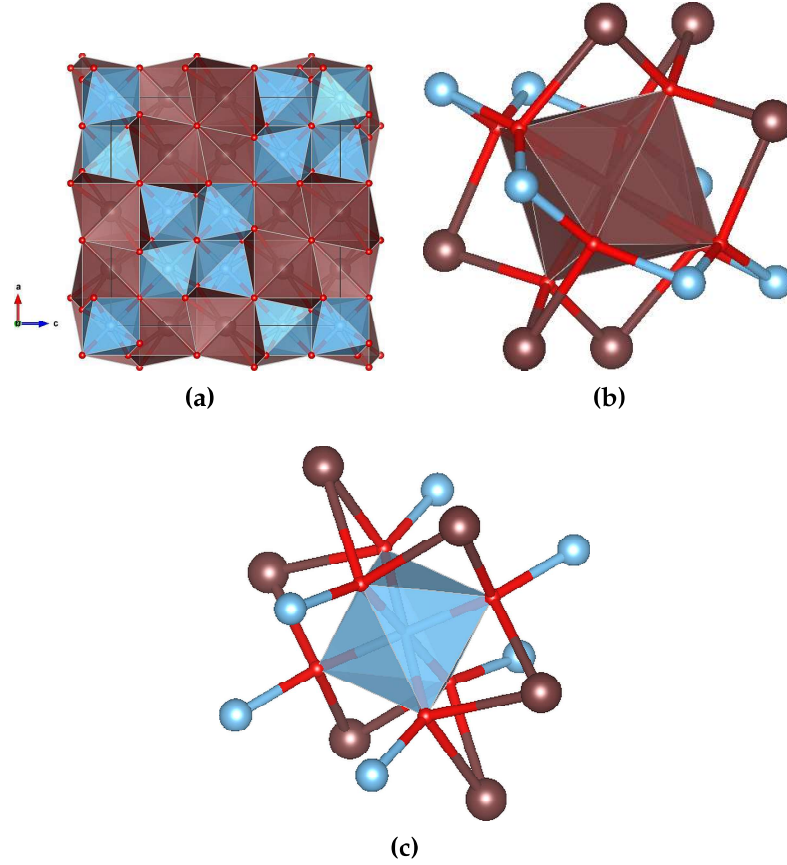
Figure 5.3 – (5.3a) $Y_2Ti_2O_7$; (5.3b) YO8 polyhedron in $Y_2Ti_2O_7$; (5.3c) TiO6 polyhedron in $Y_2Ti_2O_7$. Brown: Yatoms; Blue: Ti atoms; Red: O atoms.

of a material to amorphization is basically defined by the competition between the long-range and short-range forces, originating from the ionic and covalent contributions to bonding. The empirical potentials used in MD studies have electrostatic charges to emulate the ionicity of the bonding and in addition, they also contain the short-range bonding interactions in order to stabilize the structure. Thus, the complete Hamiltonian of the system will indeed have contributions from both the long and short-range order forces. In this section, we improve upon the insight obtained from the constraints analysis by explicitly calculating the total energies of the distorted systems by using interatomic potentials for these materials. This is done by applying various distortions to the individual cation polyhedra and calculating the change in energy of the systems by performing molecular statics runs using LAMMPS [13]. The idea is, given a distortion, higher the change in energy of the network, more will be its aversion to that alternative arrangement, and hence,

Vertex	Connectivity (C)	Edge connected polyhedra	Corner shared
O_1	3	1 (1 Y)	1 (1 Ti)
O_2	4	1 (1 Y)	2 (2 Y)
O_3	4	3 (2 Y, 1 Ti)	0
O_4	4	2 (2 Y)	1 (1 Ti)
O_5	4	3 (2 Y, 1 Ti)	0
O_6	4	3 (2 Ti, 1 Y)	0
O_7	3	1 (1 Y)	1 (1 Ti)

Table 5.3 – Connectivities of a YO7 polyhedron in the Y_2TiO_5 lattice.

Vertex	Connectivity (C)	Edge connected polyhedra	Corner shared
O_1	3	0	2 (Y)
O_2	4	2 (2 Y)	1 (Ti)
O_3	4	2 (2 Y)	1 (Y)
O_4	4	2 (2 Y)	1 (Y)
O_5	4	2 (2 Y)	1 (Y)

Table 5.4 – Connectivities of a TiO5 polyhedron in the Y_2TiO_5 lattice.

while a strongly ionic system, such as NaCl ($f = -10$) is having a substantially higher amorphization resistance than all of them. On the other hand, these systems have more amorphization resistance than TiO_2 ($f = -4$), SiC ($f = -3$). The materials such as Si ($f = +1$), B_2O_3 ($f = +1$) are highly amorphizable as they are under constrained [31].

5.4 Analysis of structural freedom by calculating strain energy in disordered systems

The topological analysis based on constraints analysis is quite successful in predicting amorphization characteristics of many materials. However, predictions using it can sometimes mislead too. For instance, both $Gd_2Zr_2O_7$ and $Gd_2Ti_2O_7$ have similar structures, and hence, according to this criteria, they must have a comparable resistance to amorphization. However, it is found that their amorphization resistance differ drastically, with $Gd_2Zr_2O_7$ being far more resistant to amorphization than $Gd_2Ti_2O_7$ [11, 56]. It seems, apart from considering only the connectivities and the structure, one should also look into the interatomic forces that operate in the systems to get the complete picture. Kostya *et. al* [57] suggest that the resistance
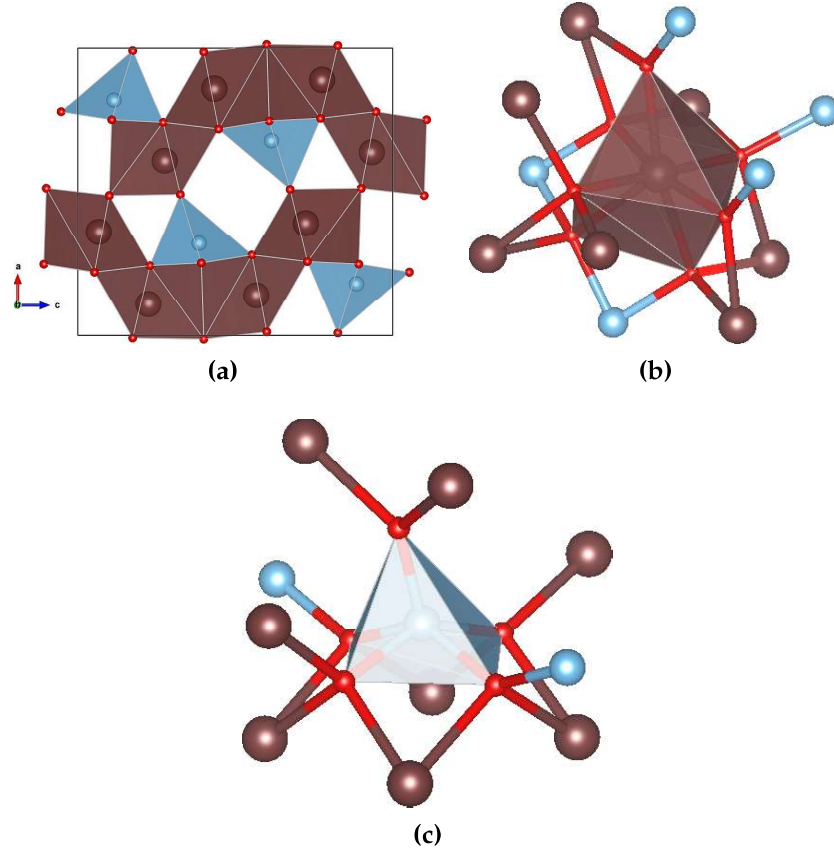
Figure 5.2 – (5.2a) Y_2TiO_5; (5.2b) YO7 polyhedron in Y_2TiO_5; (5.2c) TiO5 polyhedron in Y_2TiO_5. Brown: Yatoms; Blue: Ti atoms; Red: O atoms.

In $Y_2Ti_2O_7$, for YO8 polyhedron, $V = 8$; $C_{avg} = 4$; $Y = 8/8 = 1$. Thus, from eqn. 5.1, $f_{YO8} = -7$

While for TiO6 polyhedron, $V = 6$; $C_{avg} = 4$; $Y = 6/6 = 1$. Thus, from eqn. 5.1, $f_{TiO6} = -6$

The structural freedom of the $Y_2Ti_2O_7$ lattice is calculated as, $f_{Y_2Ti_2O_7} = (2f_{YO8} + 2f_{TiO6})/4 = -6.5$

Thus, structural degrees of freedom for Y_2O_3, Y_2TiO_5 and $Y_2Ti_2O_7$ crystals are $-6, -5.786$ and -6.5 respectively. The negative structural degree of freedom indicates these systems are highly constrained and hence, they all must be resistant to amorphization. Further, all the three systems should have a comparable amorphization resistance, with $Y_2Ti_2O_7$ having slightly higher amorphization resistance, followed by Y_2O_3, and then Y_2TiO_5. This analysis predicts the amorphization resistance of Y-Ti-O systems as comparable to that of α-Al_2O_3 ($f = -6.25$),

Vertex	Connectivity (C)	Edge connected polyhedra	Corner shared
O_1	4	3 (2 Y_a, 1 Y_b)	0
O_2	4	2 (1 Y_a, 1 Y_b)	1 (1 Y_a)
O_3	4	1 (1 Y_a)	2 (1 Y_a, 1 Y_b)
O_4	4	2 (1 Y_a, 1 Y_b)	1 (1 Y_a)
O_5	4	3 (2 Y_a, 1 Y_b)	0
O_6	4	1 (1 Y_a)	2 (1 Y_a, 1 Y_b)

Table 5.1 – Connectivities of a Y_aO6 polyhedron in the Y_2O_3 lattice. The type of cation polyhedra to which the representative polyhedron is linked are written in brackets. For example, in the first row, third column, 3 (2 Y_a, 1 Y_b) represents edge connectivity to 3 different cation polyhedra, out of which 2 are Y_a polyhedra, whilst 1 is Y_b polyhedron. In this and the upcoming tables, O_1, O_2 etc., represent the vertices of the cation polyhedra, which are always the oxygen atoms.

Vertex	Connectivity (C)	Edge connected polyhedra	Corner shared
O_1	4	2	1
O_2	4	2	1
O_3	4	2	1
O_4	4	2	1
O_5	4	2	1
O_6	4	2	1

Table 5.2 – Connectivities of a Y_bO6 polyhedron in the Y_2O_3 lattice. All connections, whether edge or corner sharing, are only with Y_a polyhedra.

5.1c, Table. 5.2) respectively. For both the type of octahedra, $V = 6$; $C_{avg} = 4$; $Y = 6/6 = 1$. Thus, from eqn. 5.1, we get, $f_{Y_aO6} = f_{Y_bO6} = -6$. Total structural degree of freedom for Y_2O_3 lattice can be calculated by taking a weighted average, $f_{Y_2O_3} = (f_{Y_aO6} + f_{Y_bO6})/2 = -6$

Y_2TiO_5 lattice is made up of YO7 and TiO5 polyhedra units. Their connectivities are shown in (Fig. 5.2b, Table. 5.3) and (5.2c, Table. 5.4) respectively. For YO7 polyhedron in Y_2TiO_5, $V = 7$; $C_{avg} = 26/7$; $Y = 7/7 = 1$. Thus, from eqn. 5.1, $f_{YO7} = -5.959$

For TiO5 polyhedron, $V = 5$; $C_{avg} = 19/5$; $Y = 4/5$. Thus, from eqn. 5.1, $f_{TiO5} = -4.64$

The structural freedom of the Y_2TiO_5 lattice is calculated as, $f_{Y_2TiO_5} = (2f_{YO7} + f_{TiO7})/3 = -5.5193$.

$Y_2Ti_2O_7$ lattice is made up of YO8 and TiO6 polyhedra units. Their connectivities are shown in (Fig. 5.3b, Table. 5.5) and (Fig. 5.3c, Table. 5.6) respectively.
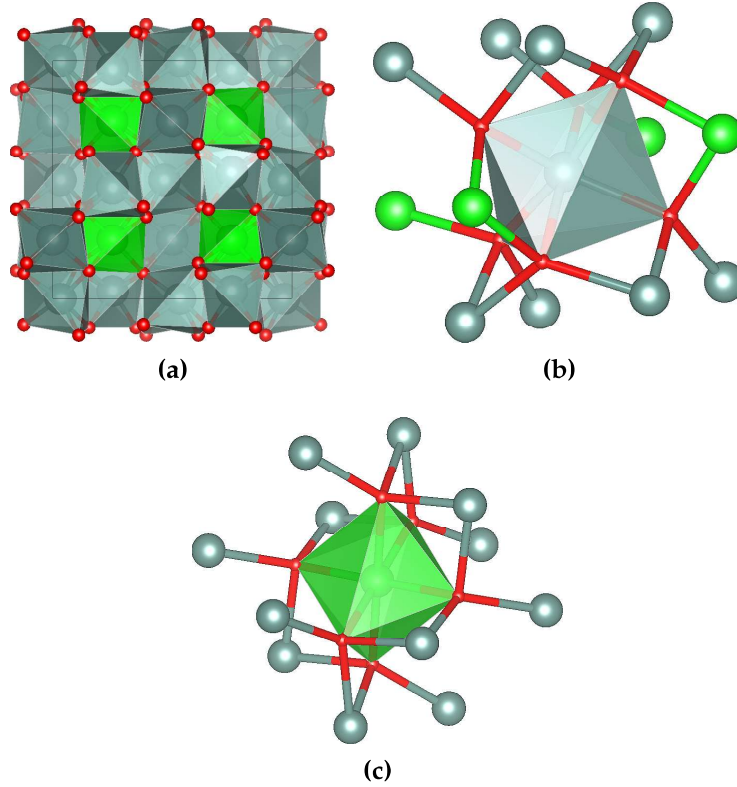
Figure 5.1 – (5.1a) Y_2O_3 structure; (5.1b) Y_aO6 octahedron in Y_2O_3; (5.1c) Y_bO6 octahedron in Y_2O_3. Silver green: Y_a atoms; Light green: Y_b atoms; Red: O atoms. In the figures depicting a single cation polyhedron, for example, in Fig. 5.1b, we show the edge or corner sharing (there is no face sharing of cation polyhedra in all the three systems) of the representative polyhedron by the respective bonds made by the vertices of the polyhedron (O atoms) with the center (cation) of the other cation polyhedra. Connectivity of two adjacent vertices of the representative polyhedron to the same neighboring cation indicates an edge-connection with the corresponding cation polyhedron, while a single connection of the neighboring cation with a given vertex of the representative polyhedron indicates corner-sharing through that vertex.

$Z = 0$ for all of them. Further, the spatial dimension (d) of the lattices as well as the dimension (δ) of the polytopes forming them is 3. The other details of the connectivities as well as of the calculations of the structural degree of freedom are as follows:

As discussed in section-3.2, bixbyite Y_2O_3 has two symmetrically inequivalent cation sites, Y_a (silver green balls) at Wyckoff positions $24d$ ($x, 0, 1/4$) and Y_b (light green balls) at Wyckoff positions $8a$ ($1/4, 1/4, 1/4$). Both Y_a and Y_b atoms sit in octahedra whose corners are oxygen atoms. Thus, the Y_2O_3 lattice can be visualized as made up of Y_aO6 and Y_bO6 cation octahedra. The connectivities of Y_aO6 and Y_bO6 octahedra are shown in (Fig. 5.1b, Table. 5.1) and (Fig.

perature (for comparison with cascade runs), we take a simulation cell of size $30 \times 30 \times 30$ Å^3 to have a direct comparison with the cascade simulation runs. The systems are equilibrated for 1 ns at the given temperature and 10 different random seeds are used for each configuration.

5.3   Analysis of Y-Ti-O systems using constraints analysis

Zachariasen [29] in 1932, proposed that materials that get a substantial energy change when disordered, must be averse to the disordered state and hence, must be resistant to amorphization. In other words, an unconstrained material will have more structural freedom for alternative arrangements than an overconstrained material, and thus, will be more prone to damage upon irradiation. This is because, one of these alternative arrangements can be the damaged state, which can be as stable as any other alternative crystalline arrangement. This proposal is quantified by the constraints analysis, where the structural degree of freedom (f) of a matrix is calculated based on the connectivities of the structuring polytopes. A material having a negative structural degree of freedom is over-constrained, and hence, resistant to radiation damage, while the one with a positive value will be readily amorphizable. Gupta *et. al* [28] came up with a formulation for calculating the structural degree of freedom (f), of a network with a dimensionality d, comprising of corner-sharing V-edged polytopes of dimensionality δ, sharing on an average C_{avg} connections per vertex, as:

$$f = d - C_{avg}[\delta - \delta(\delta+1)/2V_{avg}] - (d-1)(Y/2) - [(p-1)d - (2p-3)](Z/p)$$

(5.1)

Where, Y = fraction of edge-sharing vertices, Z = fraction of face-sharing vertices and p = number of shared polygonal faces.

As seen in figures 5.1, 5.2 and 5.3, for all the three systems, there is no face sharing between any of the polyhedra in their respective lattices, which implies

test the results obtained from constraints analysis by explicitly incorporating interatomic potentials for the systems (section 5.4). Then we proceed to simulate dynamic disorder in the systems by inducing displacement cascades and by equilibrating them at high temperatures. In section 5.5, we analyze the disorder mainly by studying the point defects, and in section 5.6, we analyze the disorder using topological tools to gain insights from a different perspective.

5.2 Computational methodology

For the displacement cascades studies, cell size for all the three systems is taken to be $\sim 100 \times 100 \times 100$ Å^3 which corresponds to 80,000 atoms for Y_2O_3, 96,000 atoms for Y_2TiO_5 and 88,000 atoms for $Y_2Ti_2O_7$ crystal. Y atom is taken as the primary knock-on atom (PKA) and its initial direction is taken to be $\hat{i} + 3\hat{j} + 5\hat{k}$, which also happens to be the crystallographic direction <135> in Y_2O_3 and $Y_2Ti_2O_7$, as they both have a cubic structure. Three different initial equilibration temperatures, 300 K, 600 K and 900 K are taken for the lattice, while 4 different PKA energies (2, 5, 6 and 8 keV) are taken for the cascade generation. To procure good statistics 10 different random seeds are used for each cascade simulation. The system is first equilibrated for 1 ns at the desired temperature and then the PKA with a given energy is initiated. To effectively model the dynamics of the displacement cascades, variable time step approach is applied, with time steps being 0.02, 0.1 and 1 femtoseconds for the ballistic, thermal spike and the annealing phase respectively. The total time of simulation is 9 psec. Other details of the MD implementation are the same as discussed in section-3.3. All the physical properties and analyses such as RDF, MSD, temperature, ring analysis etc., have been carried out in a region of size $30 \times 30 \times 30$ Å^3 which contains the cascade at its peak (at t_{peak}), such that the centre of the box coincides with the position of the centre of mass of the Frenkel pairs at the peak of cascade. This region corresponds to maximum cascade volume corresponding to the 8 keV cascade. The calculation of point defects is done by using equivalent sphere method [30].

For all the studies involving equilibrating the systems at a given high tem-

tion which starts from the interface between the host matrix and the oxide nan-ocluster [42, 43]. It is evident, that an understanding of the damage mechanism and amorphization in these systems is highly required, as it will enable us to predict long-term material degradation, and will pave the way for designing better materials.

The experiments on understanding the radiation stability and amorphization of Y-Ti-O oxides under irradiation damage vary drastically and the general consensus on this topic remains difficult to form [6]. On the other side, literature has many analytical and phenomenological criteria for predicting amorphization resistance. However, while many of these criteria are successful for one class of materials, they fail for others [11]. In this regard, MD has emerged as a useful tool to gain insights into the basic mechanism of damage processes. Realistic interatomic potentials used in MD can mimic the role played by the short and the long-range forces in materials, which are the decisive factors for the relative amorphizabilities of materials [11]. Further, MD can actually track the dynamics in the thermal spike regime, where most of the atomic rearrangements take place. This is an important feature, as by using MD, it is shown, that the number of point defects that actually survive after displacement cascades is in general, smaller than that predicted by NRT model [58].

However, when analyzing the damage in materials, one should consider various factors and it has been shown that a description based on point defects may not be sufficient for materials that can support permanent radiation cascades with high structural disorder and also, in the case of highly energetic processes such as displacement cascades. In these scenarios, one must look for different ways to analyse the disorder in materials [53].

Thus, in this chapter, we make a comparative study of Y-Ti-O systems by using different tools and use molecular dynamics to investigate the dynamics of displacement cascades. Different PKA energies, as well as simulation temperatures, are taken to understand the behavior of these oxides under various conditions. We start with analyzing the systems using constraints analysis (section 5.3) and then

Chapter 5

A comparative study of displacement cascades in Y-Ti-O systems using structural and connectivity topology analyses

In this chapter we make a comparative study of Y-Ti-O crystals to understand their irradiation behavior. MD simulations of displacement cascades are carried out and the damage is characterized using various tools to gain insights into the amorphization characteristics of these systems from different perspectives.

5.1 Introduction

Y_2O_3, Y_2TiO_5 and $Y_2Ti_2O_7$ precipitates are the basic ingredients of the ODS steels. They provide mechanical strength [8], reduce the void growth by trapping helium [7], and are believed to provide radiation stability [2]. These oxide nanoclusters are observed to be having a good coherence with the host matrix, which is an important property for their role as effective sinks for the defects [39].

However, It is seen, that under irradiation, the coherence of the precipitates with the host matrix gets degraded [39, 44]. The size and the volume fraction of these oxide nanoclusters are very crucial parameters for their role in pinning the dislocations [10], and it is observed that upon irradiation, nanoparticles can get eroded, resulting in the size reduction too. These effects occur due to amorphiza-

might not have got ruptured. In all these scenarios, one must also look into the topology of the disordered system. A complete picture of the damage can be obtained by using all the different tools together to analyze the damage so that the perspective obtained from one method can be complemented by some other tool based on a completely different approach.

6.2 Future outlook

The work presented in this thesis can be further advanced by carrying out further simulations along the following directions:

- MD studies of radiation damage, as well as topological analysis of the different pyrochlore and fluorite systems can be carried out to gain an understanding of the relative stability under radiation damage of these crystal classes.

- Ab initio calculations can be performed and electronic density maps of pyrochlore and fluorite systems can be analyzed to understand the detailed bonding characteristics of these materials. This will help in gaining an understanding of their amorphization characteristics.

	Property	Comparison	Section
1	Topogical Degree of freedom (f)	$Y_2Ti_2O_7 \gtrsim Y_2O_3 \gtrsim Y_2TiO_5$	5.3
2	Strain energy upon distortion	$Y_2Ti_2O_7 \gtrsim Y_2O_3 \sim Y_2TiO_5$	5.4
3	No. of FP surviving	$Y_2TiO_5 > Y_2Ti_2O_7 > Y_2O_3$	5.5.1
4	Ballistic diffusion (MSD)		5.5.2
5	Surviving cation antisites	$Y_2Ti_2O_7 > Y_2TiO_5 .(Y_2O_3 \text{ N.A})$	5.5.3
6	Surviving a-c antisites	$Y_2TiO_5 > Y_2Ti_2O_7 > Y_2O_3$	5.5.3
7	Topological order at t_{peak}	$Y_2O_3 \sim Y_2Ti_2O_7 > Y_2TiO_5$	5.6.2
8	Topological order regained		5.6.3

Table 6.1 – A summary of results comparing the Y-Ti-O systems.

Based on this work, it is understood that to characterize damage suffered by materials due to radiation damage, one must analyze various factors. In a displacement cascade event, point defects are generated and a study of the number of point defects generated and survived can provide a measure of disorder in many materials. The subsequent damage evolution of the material crucially depends upon two factors. First is, the degree to which the stability of the lattice gets affected by the accumulation of defects. This factor influences in a major way a material's proclivity for amorphization under irradiation. The second factor is, the ultimate fate of the point defects produced in a displacement cascade event. The interstitials and vacancies produced can migrate and annihilate harmlessly by interstitial-vacancy recombination or, they can start clustering to form dislocation loops and voids. A material in which clustering occurs with ease will be prone to void swelling.

However, a description based only on point defects may not render a complete picture of the damage in materials that can support permanent radiation cascades with a high structural disorder. Further, such an analysis will also fail in highly energetic situations, as the material is free to distort and move, giving a false inference that point defects have generated, while the basic connectivities of the system

ous distortions, validated and matched the results of the constraints analysis quite nicely.

- A delayed production and a subsequent saturation of the cation antisites is seen in both Y_2TiO_5 and $Y_2Ti_2O_7$. Cation antisites survive in a far more number in $Y_2Ti_2O_7$ as compared to Y_2TiO_5, indicating the ease for cation disorder in $Y_2Ti_2O_7$, and hence the possibility of stability under irradiation. Although the cation antisite formation occurs, anion disordering is not discernible, indicating $Y_2Ti_2O_7$ has undergone an incomplete order-disorder transition. Since in pyrochlores, cation antisite formation is known to felicitate anion disordering, it is expected that higher PKA energies may lead to a complete order-disorder transition to defect fluorite structure.

- Y_2O_3, due to its strong Y-O bonding, recovers its crystallinity quickest and thus is a highly resilient, amorphization resistant structure, while $Y_2Ti_2O_7$, owing to its ease for cation disordering, also seems to be quite resistant to amorphization. In all the properties studied, Y_2O_3 and $Y_2Ti_2O_7$ fair better than Y_2TiO_5 in terms of radiation stability and resistance to amorphization. Table 6.1 lists the main properties studied to investigate the resistance to amorphization, and the comparative behaviour of Y-Ti-O systems.

the highlights of the work carried out, and the results obtained in this thesis.

- New interatomic potentials for Y_2TiO_5 and $Y_2Ti_2O_7$ crystals have been developed. The functional form for the potentials is combined Coulomb and Buckingham. Since the potentials are of the rigid-ion type and lack shell components, they are appropriate for large-scale MD simulations. Further, repulsive part of the potentials has been modeled with extra care, thus making them suitable for radiation damage simulations, where atoms can come quite close to each other such that their electronic shells start overlapping.

- The potentials reproduce the melting points of both Y_2TiO_5 and $Y_2Ti_2O_7$ quite closely to the experimental values, indicating they are suitable for studying thermal properties. Defect formation energy calculations showed that in both Y_2TiO_5 and $Y_2Ti_2O_7$, the formation energy for the cation antisite pairs is quite small. The physical properties such as lattice constants, elastic constants, coordination number, the coefficient of thermal expansion etc., were calculated and found to be in a fairly good agreement with the experimental/ first principle values.

- In general, a radiation damaged system can have a very different topology from a melted system. Topological analysis using rings statistics shows that it can be used as a tool to bring out the differences between a melted system and a radiation damaged system. The short and medium-range order can persist in a radiation damaged system even at the peak of the cascade as opposed to the loss of order seen in melted systems. While in Y_2O_3 and $Y_2Ti_2O_7$, the topology of the radiation damaged systems does not deviate too far from the corresponding crystalline counterpart, in Y_2TiO_5, it is similar to the topology of the corresponding melted system.

- Constraints analysis showed that all the three Y-Ti-O systems are constrained and must be in general, resistant to amorphization. $Y_2Ti_2O_7$ has a more constrained structure than Y_2O_3 and Y_2TiO_5. Calculation of the lattice strain energy by incorporating interatomic potentials in Y-Ti-O systems for vari-

Chapter 6

Conclusions and future outlook

In this chapter, we outline the highlights of all the main results obtained in this thesis and discuss the ways the present work can be extended.

6.1   Conclusions

In this thesis, we have used classical MD to study displacement cascades in Y-Ti-O systems. For MD, reliable interatomic potentials are the prime requirement and the need for realistic potentials becomes even more important when studying the amorphization characteristics of materials. Since appropriate interatomic potentials were not available for Y_2TiO_5 and $Y_2Ti_2O_7$, we have developed new pairwise interatomic potentials for these systems.

In Chapter-1, we presented the general motivation and an overview of the problem addressed in the thesis. In Chapter-2, we discussed the theoretical and computational techniques used in the work and also elucidated about the various types of rings present in the Y-Ti-O crystal systems. In Chapter-3, mainly the results obtained for the low-energy displacement cascades in Y_2O_3, with Y and O PKAs initiated in various crystallographic directions, were discussed. Then in Chapter-4, we presented the details of the methodology and validation of the interatomic potentials developed for Y_2TiO_5 and $Y_2Ti_2O_7$ crystals. In Chapter-5, we discussed the comparative behavior of the cascade characteristics in Y-Ti-O systems for different simulation conditions and analyzed them using different tools. Now we outline

[154] W. R. Panero, L. Stixrude, and R. C. Ewing, Physical Review B **70**, 054110 (2004). 109

[155] M. W. Ullah, A. Kuronen, K. Nordlund, F. Djurabekova, P. Karaseov, and A. Titov, Journal of Applied Physics **112**, 043517 (2012). 112

[156] Y. Jin, Y. Jiang, L. Yang, G. Lan, G. Robert Odette, T. Yamamoto, J. Shang, and Y. Dang, Journal of Applied Physics **116**, 143501 (2014). 126

[135] L. Hobbs, A. Sreeram, C. Jesurum, and B. Berger, Nuclear Instruments and Methods in Physics Research Section B: Beam Interactions with Materials and Atoms **116**, 18 (1996). 62, 98

[136] M. Dholakia, S. Chandra, M. Valsakumar, and S. M. Jaya, Journal of Nuclear Materials **454**, 96 (2014). 65

[137] K. D. Hammond, H. J. L. Voigt, L. A. Marus, N. Juslin, and B. D. Wirth, Journal of Physics: Condensed Matter **25**, 055402 (2013). 66, 67, 71

[138] R. Williford, W. Weber, R. Devanathan, and J. Gale, Journal of Electroceramics **3**, 409 (1999). 66

[139] P. Wilde and C. Catlow, Solid State Ionics **112**, 173 (1998).

[140] T. S. Bush, J. D. Gale, C. R. A. Catlow, and P. D. Battle, Journal of Materials Chemistry **4**, 831 (1994).

[141] L. Minervini, R. W. Grimes, and K. E. Sickafus, Journal of the American Ceramic Society **83**, 1873 (2000). 66, 67

[142] B. Dick Jr and A. Overhauser, Physical Review **112**, 90 (1958). 66

[143] M. Cooper, M. Rushton, and R. Grimes, Journal of Physics: Condensed Matter **26**, 105401 (2014). 66, 67, 81

[144] D. S. Gunn, N. L. Allan, H. Foxhall, J. H. Harding, J. A. Purton, W. Smith, M. J. Stein, I. T. Todorov, and K. P. Travis, Journal of Materials Chemistry **22**, 4675 (2012). 67

[145] Y. Jiang, J. R. Smith, and G. R. Odette, Acta Materialia **58**, 1536 (2010). 67, 69, 82, 106, 126

[146] W. G. Mumme and A. D. Wadsley, Acta Crystallographica Section B **24**, 1327 (1968). 72, 73, 77

[147] A. F. Fuentes, K. Boulahya, M. Maczka, J. Hanuza, and U. Amador, Solid State Sciences **7**, 343 (2005). 72

[148] K. C. Seymour, Ph.D. thesis, University of Illinois at Urbana-Champaign (2015). xxvii, 80

[149] M. J. P. Musgrave, *Crystal Acoustics* (Holden-Day, San Francisco, 1970). 81

[150] Y. Luan, Ph.D. thesis, University of Tennessee (2011). xxx, 82

[151] H. B. Huntington, Solid State Physics **7**, 213 (1958). 81

[152] S. Munetoh, T. Motooka, K. Moriguchi, and A. Shintani, Computational Materials Science **39**, 334 (2007). 96

[153] H. Hsieh, T. D. De La Rubia, R. Averback, and R. Benedek, Physical Review B **40**, 9986 (1989). 102, 117

[115] J. Robertson, The European Physical Journal-Applied Physics **28**, 265 (2004). 45

[116] X. Qin, T. Yokomori, and Y. Ju, Applied Physics Letters **90**, 073104 (2007). 45

[117] G. Baldinozzi, J. Berar, and G. Calvarin-Amiri, in *Materials Science Forum* (Trans Tech Publ, 1998), vol. 278, pp. 680–685. 46

[118] Y. N. Xu, Z. Q. Gu, and W. Ching, Physical Review B **56**, 14993 (1997). 46

[119] F. Hanic, M. Hartmanová, G. Knab, A. Urusovskaya, and K. S. Bagdasarov, Acta Crystallographica Section B: Structural Science **40**, 76 (1984). 47

[120] C. Janowitz, V. Scherer, M. Mohamed, A. Krapf, H. Dwelk, R. Manzke, Z. Galazka, R. Uecker, K. Irmscher, R. Fornari, et al., New Journal of Physics **13**, 085014 (2011). 47

[121] S. Krishnan and D. L. Price, Journal of Physics: Condensed Matter **12**, 145 (2000). 48

[122] S. Krishnan, S. Ansell, and D. L. Price, Journal of the American Ceramic Society **81**, 1967 (1998). 48

[123] A. Calder and D. Bacon, Journal of Nuclear Materials **207**, 25 (1993). 50, 54

[124] I. Monnet, T. V. D. Berghe, and P. Dubuisson, Journal of Nuclear Materials **424**, 204 (2012). 50, 53, 100

[125] A. Stukowski, Modelling and Simulation in Materials Science and Engineering **18**, 015012 (2009). xxv, 51

[126] M. Norgett, M. Robinson, and I. Torrens, Nuclear Engineering and Design **33**, 50 (1975). 54

[127] J. Zheng, G. Ceder, T. Maxisch, W. K. Chim, and W. K. Choi, Physical Review B **73**, 104101 (2006). 55

[128] H. Wendt and F. F. Abraham, Physical Review Letters **41**, 1244 (1978). 58

[129] W. Baur, Acta Crystallographica Section B: Structural Crystallography and Crystal Chemistry **30**, 1195 (1974). 59

[130] P. K. Gupta and A. Cooper, Journal of Non-Crystalline Solids **123**, 14 (1990). 60

[131] S. Alavi, N. Joffin, M. Vérelst, and B. Caussat, Chemical Engineering Journal **125**, 25 (2006). 61

[132] M. Ishii, A. Nakao, and K. Sakurai, in *Journal of Physics: Conference Series* (IOP Publishing, 2007), vol. 83, p. 012014. 61

[133] L. Pauling, Journal of the American Chemical Society **54**, 3570 (1932). 61

[134] L. Wang, W. Yang, Y. Ding, Y. Ren, S. Xiao, B. Liu, S. V. Sinogeikin, Y. Meng, D. J. Gosztola, G. Shen, et al., Physical Review Letters **105**, 095701 (2010). 61

[93] J. E. Jones, in *Proceedings of the Royal Society of London A: Mathematical, Physical and Engineering Sciences* (The Royal Society, 1924), vol. 106, pp. 463–477. 25

[94] M. Baskes and R. Johnson, Modelling and Simulation in Materials Science and Engineering **2**, 147 (1994). 27

[95] E. Wigner and F. Seitz, Physical Review **43**, 804 (1933). 30

[96] P. Hohenberg and W. Kohn, Physical Review **136**, B864 (1964). 31, 32, 69

[97] W. Kohn and L. J. Sham, Physical Review **140**, A1133 (1965). 32, 69

[98] J. P. Perdew and Y. Wang, Physical Review B **45**, 13244 (1992). 34

[99] S. H. Vosko, L. Wilk, and M. Nusair, Canadian Journal of Physics **58**, 1200 (1980). 34

[100] J. P. Perdew, K. Burke, and M. Ernzerhof, Physical Review Letters **77**, 3865 (1996). 35, 69

[101] J. P. Perdew and Y. Wang, Physical Review B **45**, 13244 (1992). 35

[102] J. P. Perdew, J. A. Chevary, S. H. Vosko, K. A. Jackson, M. R. Pederson, D. J. Singh, and C. Fiolhais, Physical Review B **46**, 6671 (1992). 35

[103] P. E. Blöchl, Physical Review B **50**, 17953 (1994). 35, 69

[104] G. Kresse and D. Joubert, Physical Review B **59**, 1758 (1999). 35

[105] H. J. Monkhorst and J. D. Pack, Physical Review B **13**, 5188 (1976). 36, 69

[106] L. Guttman, Journal of Non-Crystalline Solids **116**, 145 (1990). 38

[107] K. Goetzke and H. J. Klein, Journal of Non-Crystalline Solids **127**, 215 (1991). 38

[108] C. S. Marians and L. W. Hobbs, Journal of Non-Crystalline Solids **119**, 269 (1990). 38

[109] H. R. Foxhall, Ph.D. thesis, The University of Sheffield (2008). xxv, 38

[110] R. Gaboriaud, F. Paumier, M. Jublot, and B. Lacroix, Nuclear Instruments and Methods in Physics Research Section B: Beam Interactions with Materials and Atoms **311**, 86 (2013). 45, 61

[111] G. Y. Adachi and N. Imanaka, Chemical Reviews **98**, 1479 (1998). 45

[112] M. Zinkevich, Progress in Materials Science **52**, 597 (2007). 45

[113] B. Hyde, Acta Crystallographica Section A: Crystal Physics, Diffraction, Theoretical and General Crystallography **27**, 617 (1971). 45

[114] B. Lacroix, F. Paumier, and R. J. Gaboriaud, Physical Review B **84**, 014104 (2011).

[73] M. Pirzada, R. W. Grimes, L. Minervini, J. F. Maguire, and K. E. Sickafus, Solid State Ionics **140**, 201 (2001).

[74] M. Rushton, R. W. Grimes, C. Stanek, and S. Owens, Journal of Materials Research **19**, 1603 (2004).

[75] C. R. Stanek, L. Minervini, and R. W. Grimes, Journal of the American Ceramic Society **85**, 2792 (2002). 12

[76] H. Y. Xiao, F. Gao, and W. J. Weber, Journal of Physics: Condensed Matter **22**, 415801 (2010). 12, 74, 83, 101

[77] G. Sattonnay, S. Cammelli, D. Menut, N. Sellami, C. Grygiel, I. Monnet, J. Béchade, J. Crocombette, A. Chartier, A. Soulié, et al., Physical Review B **94**, 224109 (2016). 12, 66

[78] M. P. Allen and D. J. Tildesley, *Computer Simulation of Liquids* (Oxford University Press, 2017). 15

[79] E. Kaxiras, *Atomic and Electronic Structure of Solids* (Cambridge University Press, 2003). 15

[80] I. Fermi, P. Pasta, S. Ulam, and M. Tsingou, Tech. Rep., Los Alamos Scientific Lab., N. Mex. (1955). 16

[81] A. Rahman, Physical Review **136**, A405 (1964). 16

[82] M. Tuckerman, *Statistical Mechanics: Theory and Molecular Simulation* (Oxford University Press, 2010). 17, 18

[83] M. Aroyo, J. Perez-Mato, D. Orobengoa, E. Tasci, G. De La Flor, and A. Kirov, Bulg. Chem. Commun **43**, 183 (2011). 18

[84] K. Momma and F. Izumi, Journal of Applied Crystallography **41**, 653 (2008). 18

[85] L. Verlet, Physical Review **159**, 98 (1967). 20

[86] D. Frenkel and B. Smit, *Understanding Molecular Simulation: from Algorithms to Applications*, vol. 1 (Academic press, 2001). 20, 48, 50

[87] H. C. Andersen, The Journal of Chemical Physics **72**, 2384 (1980). 22

[88] H. J. Berendsen, J. V. Postma, W. F. Van Gunsteren, A. DiNola, and J. Haak, The Journal of Chemical Physics **81**, 3684 (1984). 22

[89] S. Nosé, The Journal of Chemical Physics **81**, 511 (1984). 22, 23, 49, 72

[90] W. G. Hoover, Physical Review A **31**, 1695 (1985). 22, 23, 49, 72

[91] C. Kittel, *Introduction to Solid State Physics* (Wiley, 2005). 25, 67

[92] R. A. Buckingham, Proceedings of the Royal Society of London A: Mathematical, Physical and Engineering Sciences **168**, 264 (1938). 25, 68

137

[55] W. Bolse, Nuclear Instruments and Methods in Physics Research Section B: Beam Interactions with Materials and Atoms **141**, 133 (1998). 9, 61, 62, 98

[56] K. Trachenko, J. Pruneda, E. Artacho, and M. T. Dove, Physical Review B **71**, 184104 (2005). 10, 94

[57] K. Trachenko, M. Pruneda, E. Artacho, and M. T. Dove, Physical Review B **70**, 134112 (2004). 10, 94

[58] M. Norgett, M. Robinson, and I. Torrens, Nuclear Engineering and Design **33**, 50 (1975). 10, 88

[59] C. Erginsoy, G. H. Vineyard, and A. Englert, Physical Review **133**, A595 (1964). 11

[60] J. Gibson, A. N. Goland, M. Milgram, and G. Vineyard, Physical Review **120**, 1229 (1960). 11

[61] T. D. De La Rubia, R. Averback, R. Benedek, and W. King, Physical Review Letters **59**, 1930 (1987). 11, 102, 117

[62] R. Webb and D. Harrison, Nuclear Instruments and Methods in Physics Research **218**, 697 (1983). 11

[63] R. Webb and D. E. Harrison Jr, Physical Review Letters **50**, 1478 (1983). 11

[64] D. J. Bacon and T. D. De La Rubia, Journal of Nuclear Materials **216**, 275 (1994). 11, 117

[65] T. D. De La Rubia and G. Gilmer, Physical Review Letters **74**, 2507 (1995). 11, 117

[66] K. Nordlund, Nuclear Instruments and Methods in Physics Research Section B: Beam Interactions with Materials and Atoms **188**, 41 (2002). 11

[67] M. Ghaly and R. Averback, Physical Review Letters **72**, 364 (1994).

[68] M. Ghaly, K. Nordlund, and R. Averback, Philosophical Magazine A **79**, 795 (1999). 11

[69] M. J. Caturla, T. D. de La Rubia, L. Marques, and G. Gilmer, Physical Review B **54**, 16683 (1996). 11

[70] T. Lazauskas, S. D. Kenny, R. Smith, G. Nagra, M. Dholakia, and M. Valsakumar, Journal of Nuclear Materials **437**, 317 (2013). 12, 46

[71] L. Kittiratanawasin, R. Smith, B. Uberuaga, K. Sickafus, A. Cleave, and R. Grimes, Nuclear Instruments and Methods in Physics Research Section B: Beam Interactions with Materials and Atoms **266**, 2691 (2008). 12, 46, 50

[72] L. Minervini, R. W. Grimes, and K. E. Sickafus, Journal of the American Ceramic Society **83**, 1873 (2000). 12, 106

[37] D. Menut, J. L. Béchade, S. Cammelli, S. Schlutig, B. Sitaud, and P. L. Solari, Journal of Materials Research **30**, 1392 (2015). 6

[38] J. Ribis, Journal of Nuclear Materials **434**, 178 (2013). 6

[39] T. Chen, J. G. Gigax, L. Price, D. Chen, S. Ukai, E. Aydogan, S. Maloy, F. Garner, and L. Shao, Acta Materialia **116**, 29 (2016). 6, 7, 87

[40] M. Miller, E. Kenik, K. Russell, L. Heatherly, D. Hoelzer, and P. Maziasz, Materials Science and Engineering: A **353**, 140 (2003), 47th International Field Emission Symposium. 7

[41] J. Xu, C. Liu, M. Miller, and H. Chen, Physical Review B **79**, 020204 (2009). 7

[42] V. Skuratov, A. Sohatsky, J. O' Connell, K. Kornieieva, A. Nikitina, V. Uglov, J. Neethling, and V. Ageev, Nuclear Instruments and Methods in Physics Research Section B: Beam Interactions with Materials and Atoms **374**, 102 (2016). 7, 88

[43] A. Aleev, N. Iskandarov, M. Klimenkov, R. Lindau, A. Möslang, A. Nikitin, S. Rogozhkin, P. Vladimirov, and A. Zaluzhnyi, Journal of Nuclear Materials **409**, 65 (2011). 7, 88

[44] M. Lescoat, J. Ribis, A. Gentils, O. Kaïtasov, Y. De Carlan, and A. Legris, Journal of Nuclear Materials **428**, 176 (2012). 7, 87

[45] H. Matzke and J. Whitton, Canadian Journal of Physics **44**, 995 (1966). 8

[46] H. Naguib and R. Kelly, Radiation Effects **25**, 1 (1975). 8, 61

[47] L. Wang, R. Eby, J. Janeczek, and R. Ewing, Nuclear Instruments and Methods in Physics Research Section B: Beam Interactions with Materials and Atoms **59**, 395 (1991). 8

[48] K. E. Sickafus, L. Minervini, R. W. Grimes, J. A. Valdez, M. Ishimaru, F. Li, K. J. McClellan, and T. Hartmann, Science **289**, 748 (2000). 9

[49] K. Sickafus, L. Minervini, R. Grimes, J. Valdez, and T. Hartmann, Radiation Effects and Defects in Solids **155**, 133 (2001). 9, 12

[50] L. Kittiratanawasin, R. Smith, B. Uberuaga, and K. Sickafus, Journal of Physics: Condensed Matter **21**, 115403 (2009). 9, 12, 46, 50

[51] K. E. Sickafus, J. A. Valdez, J. R. Williams, R. W. Grimes, and H. T. Hawkins, Nuclear Instruments and Methods in Physics Research Section B: Beam Interactions with Materials and Atoms **191**, 549 (2002). 9, 104, 121

[52] L. Minervini, R. W. Grimes, Y. Tabira, R. L. Withers, and K. E. Sickafus, Philosophical Magazine A **82**, 123 (2002). 9, 12, 104, 121

[53] L. W. Hobbs, Journal of Non-Crystalline Solids **182**, 27 (1995). 9, 88, 112

[54] L. W. Hobbs, F. W. Clinard, S. J. Zinkle, and R. C. Ewing, Journal of Nuclear Materials **216**, 291 (1994). 9

[16] L. W. Hobbs, Journal of Non-Crystalline Solids **192**, 79 (1995). xvii

[17] A. B. Belonoshko, G. Gutierrez, R. Ahuja, and B. Johansson, Physical Review B **64**, 184103 (2001). xviii, xix, 48, 65, 78, 96

[18] V. Gaydaenko and V. Nikulin, Chemical Physics Letters **7**, 360 (1970). xviii, 25, 48

[19] P. Jegadeesan, S. Amirthapandian, G. Kaur, S. Chandra, and B. K. Panigrahi, Physica Status Solidi (B) **252**, 206 (2015). xviii, 67, 71

[20] G. Kresse, J. Furthmüller, and J. Hafner, Europhysics Letters **32**, 729 (1995). xviii, 69

[21] G. Kresse and J. Hafner, Physical Review B **49**, 14251 (1994).

[22] G. Kresse and J. Furthmüller, Computational Materials Science **6**, 15 (1996).

[23] G. Kresse and J. Furthmüller, Physical Review B **54**, 11169 (1996). xviii, 69

[24] J. D. Gale, Journal of the Chemical Society, Faraday Transactions **93**, 629 (1997). xix, 70, 74

[25] C. Holcombe, M. Morrow, D. Smith, and D. Carpenter, Tech. Rep., Oak Ridge Y-12 Plant, Tenn.(USA) (1974). xix, 78, 110

[26] H. Xu and H. Guo, *Thermal Barrier Coatings* (Elsevier, 2011). xix, xxvii, 78, 80

[27] J. Lian, J. Chen, L. M. Wang, R. C. Ewing, J. M. Farmer, L. A. Boatner, and K. B. Helean, Physical Review B **68**, 134107 (2003). xix, 40, 76, 105, 106, 107

[28] P. K. Gupta, Journal of the American Ceramic Society **76**, 1088 (1993). xix, 8, 60, 90

[29] W. H. Zachariasen, Journal of the American Chemical Society **54**, 3841 (1932). xix, 90

[30] D. Terentyev, C. Lagerstedt, P. Olsson, K. Nordlund, J. Wallenius, C. S. Becquart, and L. Malerba, Journal of Nuclear Materials **351**, 65 (2006). xx, 30, 50, 89, 99

[31] L. W. Hobbs, Nuclear Instruments and Methods in Physics Research Section B: Beam Interactions with Materials and Atoms **91**, 30 (1994). xx, 9, 62, 94, 96, 98, 117

[32] R. Averback and T. D. De La Rubia, Solid State Physics **51**, 281 (1997). xxv, 3, 11, 12, 46

[33] E. Little, Materials Science and Technology **22**, 491 (2006). xxv, 3, 4

[34] J. A. Brinkman, Journal of Applied Physics **25**, 961 (1954). xxv, 4

[35] A. Brailsford and R. Bullough, Journal of Nuclear Materials **44**, 121 (1972). 4

[36] S. Ukai and M. Fujiwara, Journal of Nuclear Materials **307**, 749 (2002). 6

References

[1] R. W. Grimes, R. J. Konings, and L. Edwards, Nature Materials **7**, 683 (2008). xv, 1

[2] G. Odette, M. Alinger, and B. Wirth, Annual Review of Materials Research **38**, 471 (2008). xv, 1, 6, 87

[3] G. Taubes, Science **263**, 629 (1994). xv, 1, 8

[4] S. J. Zinkle and L. L. Snead, Annual Review of Materials Research **44**, 241 (2014). xv, 2, 6

[5] G. S. Was, *Fundamentals of Radiation Materials Science: Metals and Alloys* (Springer, 2016). xv, xvi, 2, 52

[6] J. P. Wharry, M. J. Swenson, and K. H. Yano, Journal of Nuclear Materials **486**, 11 (2017), ISSN 0022-3115. xv, xvi, 6, 7, 88

[7] M. J. Alinger, G. R. Odette, and D. T. Hoelzer, Journal of Nuclear Materials **329**, 382 (2004). xv, 6, 87

[8] J. Benjamin and T. Volin, Metallurgical Transactions **5**, 1929 (1974). xv, 1, 6, 87

[9] G. Odette, P. Miao, T. Yamamoto, D. Edwards, H. Tanagawa, and R. Kurtz, Transactions-American Nuclear Society **98**, 1148 (2008). xv, 1, 6

[10] J. Zhang, J. Lian, A. F. Fuentes, F. Zhang, M. Lang, F. Lu, and R. C. Ewing, Applied Physics Letters **94**, 243110 (2009). xvi, 6, 87

[11] K. Trachenko, Journal of Physics: Condensed Matter **16**, R1491 (2004). xvi, xix, 8, 9, 10, 88, 94, 99

[12] S. Yip, *Handbook of Materials Modeling* (Springer Science & Business Media, 2007). xvi, xviii, 25, 65, 68

[13] S. Plimpton, P. Crozier, and A. Thompson, Sandia National Laboratories (2007). xvi, xx, 49, 72, 95, 96

[14] S. Le Roux and P. Jund, Computational Materials Science **49**, 70 (2010). xvii, xix, xx, 15, 38, 99, 116

[15] H. Foxhall, K. Travis, L. Hobbs, S. Rich, and S. Owens, Philosophical Magazine **93**, 328 (2013). xvii, xx, 115, 123